

Preparation and characterization
of two-dimensional surface alloys of rare earth
metals on Pt (111)



POZNAN UNIVERSITY OF TECHNOLOGY

Preparation and characterization
of two-dimensional surface alloys of rare earth
metals on Pt (111)

Marta Izabela Przychodnia
Institute of Physics
Poznan University of Technology

Supervisor D.Sc. Eng. Wojciech Koczorowski, PUT Professor
Auxiliary supervisor Ph.D. Eng. Maciej Bazarnk

Poznań, 2023

Abstract

Surface alloys are of great importance in the development of modern technologies such as modern electronics (spintronics and molecular electronics) or the energy industry. In this dissertation, I have investigated two surface alloys systems of rare earth metal with platinum to address their structural, electronic, and magnetic properties. The mentioned systems form two types of surface alloys with the stoichiometry rare earth metal-Pt₂ and rare earth metal-Pt₅. They differ not only in structure but also in electronic and magnetic properties. In addition, they form multilayers that also possess varying properties. In the case of the Gd-Pt system, the coexistence of these two types of alloys was observed, while the Dy-Pt system forms only DyPt₂ in the stoichiometry. All surface alloys exhibit long-range and short-range orders which makes them ideal candidates as templated substrates for the growth of molecular devices or dense-packed nanodot networks as a magnetic storage in spintronics. Depending on the stoichiometry and termination layer, they also differ in reactivity and electronic and magnetic properties. Moreover, the properties of these surface alloys rely not only on the chosen rare earth metal but also on the number of surface alloy layers.

The first chapter of the dissertation contains an introduction to the research topic. Further, the theoretical concepts of magnetic interactions and thin film growth are introduced. Another chapter focuses on the analysis of the current state of the art on surface alloys of rare earth metals with noble metals, with particular emphasis on the surface alloys with platinum. Two other chapters are devoted to the characterization of experimental and theoretical methods as well as experimental setups used in the research. Finally, a detailed analysis of the structure, electronic properties, and magnetism of the surface alloys is presented and discussed.

Streszczenie

Stopy powierzchniowe mają istotne znaczenie dla rozwoju nowoczesnych technologii, takich jak elektronika (spintronika i elektronika molekularna) czy energetyka. W przedstawionej rozprawie zbadalam dwa układy stopów powierzchniowych metali ziem rzadkich z platyną, aby określić ich właściwości strukturalne, elektronowe i magnetyczne. Wspomniane systemy tworzą dwa typy stopów powierzchniowych o stechiometrii metal ziem rzadkich – Pt₂ i metal ziem rzadkich – Pt₅. Różnią się one nie tylko strukturą, ale także właściwościami elektronowymi i magnetycznymi. Ponadto tworzą multiwarstwy, które także mają różne właściwości. W przypadku układu Gd-Pt zaobserwowano współistnienie tych dwóch typów stopów, natomiast układ Dy-Pt tworzy jedynie typ DyPt₂. Wszystkie stopy powierzchniowe wykazują uporządkowanie dalekiego i krótkiego zasięgu, co czyni je idealnymi kandydatami jako podłoża do wzrostu urządzeń molekularnych lub gęsto upakowanych sieci nanokropek kwantowych jako pamięci magnetycznych w spintronice. W zależności od stechiometrii i warstwy terminującej różnią się one także reaktywnością, właściwościami elektronowymi i magnetycznymi. Co więcej, na właściwości tych stopów powierzchniowych ma wpływ nie tylko wybrany metal ziem rzadkich, ale także liczba warstw stopu.

Pierwszy rozdział rozprawy zawiera wprowadzenie w tematykę badawczą. Następnie przedstawione zostały teoretyczne koncepcje oddziaływań magnetycznych i wzrostu cienkich warstw. Kolejny rozdział skupia się na analizie aktualnego stanu wiedzy na temat stopów powierzchniowych metali ziem rzadkich z metalami szlachetnymi, ze szczególnym uwzględnieniem stopów powierzchniowych z platyną. Dwa kolejne rozdziały poświęcono charakterystyce metod eksperymentalnych i teoretycznych oraz układów eksperymentalnych stosowanych w badaniach. Na koniec przedstawiona została szczegółowa analiza struktury, właściwości elektronowych oraz magnetycznych stopów powierzchniowych.

Abbreviations

1 L DyPt₂ single layer DyPt₂

1 L GdPt₂ single layer GdPt₂

1 L GdPt₅ single layer GdPt₅

2 L double layer

2D two-dimensional

2 L GdPt₅ double layer GdPt₅

3D three-dimensional

3 L DyPt₂ triple layer DyPt₂

AES Auger electron spectroscopy

CCM constant current mode

CHM constant height mode

CITS current imaging tunneling spectroscopy

DFT density functional theory

DM Dzialoshinsky-Moriya

DOS density of states

FER field emission resonance

IPS image-potential state

JT Joule-Thomson

LDA local density approximation

LDOS local density of states

LEED low-energy electron diffraction

LHe liquid helium

- LN₂** liquid nitrogen
- LSDA** local spin density approximation
- LT** low temperature
- LTS** line tunneling spectroscopy
- ML** monolayer
- NEXAFS** near edge x-ray absorption fine structure
- NM** noble metals
- NND** nearest-neighbor distance
- PDOS** partial density of states
- PTS** point tunneling spectroscopy
- REM** rare earth metal
- RKKY** Ruderman-Kittel-Kasuya-Yosida
- RT** room temperature
- SLS** Swiss Light Source
- STM** scanning tunneling microscopy/microscope
- TEY** total electron yield
- u.c.** unit cell
- UHV** ultra-high vacuum
- UV** ultraviolet
- VT** variable temperature
- XAS** x-ray absorption spectroscopy
- XMCD** x-ray magnetic circular dichroism

Contents

Abstract	V
Streszczenie	VII
List of abbreviations	X
1 Introduction	1
2 Theoretical concepts	3
2.1 Magnetic interactions	3
2.2 Thin films growth	9
3 State of the art	13
3.1 Rare earth metals – noble metals surface alloys	13
3.2 Rare earth metals – Pt compounds	17
4 Methods	23
4.1 Scanning tunneling microscopy	23
4.1.1 Theoretical concept of tunneling effect	26
4.1.2 Surface imaging	29
4.1.3 Differential conductance measurements	31
4.2 Low-energy electron diffraction	36
4.3 Auger electron spectroscopy	39
4.4 X-ray spectroscopy techniques	41
4.4.1 X-ray absorption spectroscopy	41
4.4.2 X-ray magnetic circular dichroism	46

4.5	Density functional theory	49
5	Experimental setup	53
5.1	UHV system with VT STM in Hamburg	53
5.2	UHV system with VT STM in Poznan	56
5.2.1	Multipurpose STM head	59
5.2.2	Cryostats	63
5.3	X07MA X-Treme beamline	68
5.4	BL-29 BOREAS beamline	70
6	Results and discussion	73
6.1	Platinum (111) single crystal	74
6.2	Surface alloys formation	76
6.3	Gd-Pt system	78
6.3.1	Structural properties of Gd-Pt surface alloys	78
6.3.2	Electronic properties of Gd-Pt surface alloys	82
6.3.3	Gd-Pt surface alloys phase diagram	85
6.3.4	Magnetic properties of Gd-Pt surface alloys	87
6.4	Dy-Pt system	92
6.4.1	Chemical composition and structural properties of Dy-Pt surface alloys	93
6.4.2	Electronic properties of Dy-Pt surface alloys	97
6.4.3	Dy-Pt surface alloys phase diagram	99
6.4.4	Magnetic properties of Dy-Pt surface alloys	100
7	Summary and conclusions	105
	Bibliography	109
	List of Tables	123
	List of Figures	125
	Acknowledgements	129
	Financial support	131

Chapter 1

Introduction

Currently, at room temperature (RT), only a few two-dimensional (2D) materials display magnetic properties. Fe, Co, and Ni are the most common pure elements that exhibit ferromagnetism at RT, but developing 2D monolayers of these elements is challenging due to their low resistance to contamination. They immediately cover with contamination and permanently lose their magnetic properties [1]. The rare earth metals (REMs) are an important group of elements that exhibit unique magnetic properties, such as high atomic magnetic moments and huge magnetocrystalline anisotropy [2]. Their peculiar magnetic properties arise from a unique shell arrangement where the 4f electrons carrying the magnetic moment are strongly localized and shielded by the 5d and 6s valence states [3]. Nowadays, REMs are commonly used as additives to enhance or modify the magnetic properties of other metals or alloys [4, 5]. Alloying is a common technique used to obtain new materials that may possess enhanced, modified, or even completely new properties compared to their components. What is more, surface alloying is a method that allows obtaining 2D structures that do not have bulk counterparts or that have entirely different properties from their bulk counterparts [6–8]. 2D magnetic surface alloys are important for developing new technologies like modern electronics, including spintronics and molecular electronics. The lattice constant of the substrate is often different from that of the surface alloy formed on top of it, resulting in an interference pattern that arises from the mismatch of lattices and/or their relative rotation. Such substrates with long-range order may support the growth of densely packed arrays of magnetic nanodots for magnetic storage in spintronics [6, 9, 10]. Besides, the surface alloy atomic structure reveals a periodic spin texture that may serve as a base for the growth of molecular devices [11]. Modifying the structural and magnetic properties of surface alloys is possible by choosing different substrates and deposited metals. These alloys may differ in stoichiometry, structural composition, and termination layer. Varying layer arrangements may result in different interactions between and within layers. Atomic radii of REMs decrease with increasing atomic number [12]. Imple-

menting atoms with different atomic radii affects the stress in the surface alloy layers, which affects the lattice constant, moiré pattern, and structure corrugation. All of these factors affect the magnetic interactions, their strength, and order, which may lead to the observation of exotic magnetic structures. Beyond basic research, REM-Pt alloys are widely used in the electrocatalytic industry. Pure Pt is a commonly used material in membrane fuel cells, but it is relatively expensive, thus seeking new materials or possible modifications to increase the efficiency is of high importance. In this context, polycrystalline alloys of REM with Pt are the most well-known materials that enhance the efficiency of the oxygen reduction reaction.

The dissertation provides a comprehensive study of the structural, electronic, and magnetic properties of two systems involving Pt and REMs. Chapter 2 gives a theoretical background of magnetic interactions, their origin, and thin film growth. Chapter 3 contains a detailed overview of surface alloys with REMs. The first part focuses on REM surface alloys with noble metals (NMs), specifically Au, Ag, and Cu, while the second part focuses on REM-Pt compounds and alloys. The next Chapter outlines the experimental and theoretical methods used in the dissertation. The primary method for identifying structures and analyzing properties is scanning tunneling microscopy (STM). The Subsection provides a description of the physical phenomenon of the tunneling effect, as well as imaging and spectroscopic modes of scanning tunneling microscopes operation. Additionally, the use of low-energy electron diffraction (LEED) and Auger electron spectroscopy (AES) for structural and chemical composition analysis on a global scale is discussed. X-ray absorption spectroscopy (XAS) and the interaction of light with matter are provided as an introduction to x-ray magnetic circular dichroism (XMCD) technique used for investigating magnetic properties. The dissertation also employs density functional theory (DFT) as a supporting technique. Chapter 5 details the experimental setups used to collect data, including two ultra-high vacuum (UHV) systems with variable temperature (VT) STMs and two endstations of synchrotron facilities. The chapter provides a detailed description of the upgraded UHV system, which includes constructional modifications and a new STM head with the thermal characterization of the new STM setup. The flow-cryostat construction and operation principle together with the adaptation of the STM head to the closed cycle low-temperature cooling cryostat are also discussed. Chapter 6 presents the research findings, including the characteristics of the pure substrate, the formation of Gd- and Dy-Pt surface alloys, and the thermal evolution of the REM-Pt surface structures. The Chapter also contains the results of the structural, electronic, and magnetic properties characterization of these systems and their discussion. Finally, Chapter 7 provides a comprehensive summary of the results and concludes the dissertation.

Chapter 2

Theoretical concepts

In this Chapter, theoretical aspects of magnetism and thin film growth are introduced. The first Subsection explores magnetic interactions in solids, including the characterization and origin of exchange interactions. In the second part, the atomic-scale details of thin film growth on metal substrates are discussed, specifically in the context of 2D surface alloys.

2.1 Magnetic interactions

Magnetic interactions enable communication between magnetic moments in solids, which is critical for spontaneous magnetization. Various magnetic interactions and their impact on long-range magnetic order are examined. Figure 2.1 provides a summary of the magnetic interactions, including their strength and range.

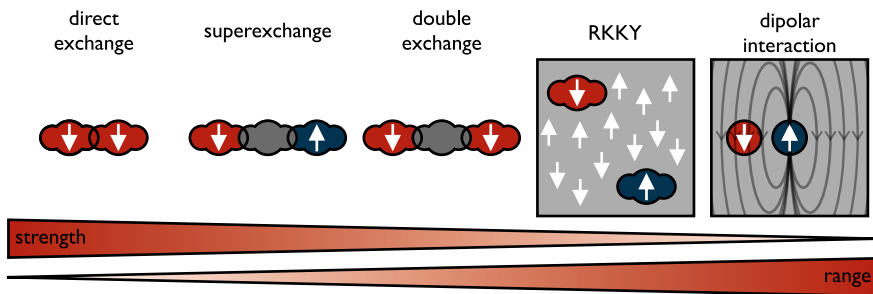


Figure 2.1: Magnetic interactions – summary graph showing the scheme, strength, and range of typical magnetic interactions. Illustration concept adapted from [13].

Magnetic dipolar interaction

The first type of magnetic interaction is magnetic dipolar interaction, which involves two magnetic dipoles μ_1 and μ_2 separated by the distance r . The

energy between them is described by [14]:

$$E_{\text{dipol}} = \frac{\mu_0}{4\pi r^3} \left[\mu_1 \cdot \mu_2 - \frac{3}{r^2} (\mu_1 r) \cdot (\mu_2 r) \right], \quad (2.1)$$

where μ_0 is the magnetic permeability of free space. The magnetic dipolar interaction diminishes as the distance between dipoles increases (as $1/r^3$), and it relies on dipoles' mutual alignment. The interaction's strength is usually around 10^{-23} J, comparable to thermal vibration energy at 1 K. That means the magnetic dipolar interaction is typically too weak to affect the long-range magnetic order of most materials, except at very low temperatures below 1 K [14].

Direct exchange interactions

Another group of magnetic interactions are exchange interactions. Their simplest form is the direct exchange, which occurs between electrons of neighboring magnetic atoms. To understand their origin, the interaction model between two electrons will be considered. Electrons are fermions, so the system of two electrons must be entirely antisymmetric under the exchange of any particle pair, according to the symmetrization postulates. Therefore the total wave function of the system Ψ also should be antisymmetric. There are two cases when it is possible. The first is when the spatial component is symmetric while the spin component is antisymmetric (singlet state), and the second is the other way around (triplet state). The wave functions and antisymmetric two-electron spin functions are described by the following equations [14]. The wave function of singlet state Ψ_S is:

$$\Psi_S = \frac{1}{\sqrt{2}} [\psi_a(\mathbf{r}_1)\psi_b(\mathbf{r}_2) + \psi_a(\mathbf{r}_2)\psi_b(\mathbf{r}_1)\chi_S], \quad (2.2)$$

where ψ_a and ψ_b are the wave functions of single electrons a and b. The antisymmetric two-electron spin function (total spin quantum number $S = 0$, $M_s = 0$):

$$\chi_S = \frac{1}{\sqrt{2}} [|\uparrow\downarrow\rangle - |\downarrow\uparrow\rangle], \quad |0, 0\rangle. \quad (2.3)$$

The wave function of the triplet state is:

$$\Psi_T = \frac{1}{\sqrt{2}} [\psi_a(\mathbf{r}_1)\psi_b(\mathbf{r}_2) - \psi_a(\mathbf{r}_2)\psi_b(\mathbf{r}_1)\chi_T], \quad (2.4)$$

with the antisymmetric two-electron spin function (total spin quantum number $S = 1$, $M_s = 1, 0, -1$):

$$\chi_T = \begin{cases} |\uparrow\uparrow\rangle & |1, 1\rangle \\ \frac{1}{\sqrt{2}} [|\uparrow\downarrow\rangle + |\downarrow\uparrow\rangle] & |1, 0\rangle \\ |\downarrow\downarrow\rangle & |1, -1\rangle \end{cases} \quad (2.5)$$

The energies of singlet and triplet states are:

$$\begin{aligned} E_S &= \int \Psi_S^* \hat{\mathcal{H}}_{\text{Heis}} \Psi_S d\mathbf{r}_1 d\mathbf{r}_2, \\ E_T &= \int \Psi_T^* \hat{\mathcal{H}}_{\text{Heis}} \Psi_T d\mathbf{r}_1 d\mathbf{r}_2, \end{aligned} \quad (2.6)$$

where $\hat{\mathcal{H}}_{\text{Heis}}$ is the Hamiltonian which can be parameterized and rewritten as an effective Hamiltonian containing a constant term representing the system's average energy (1 singlet + 3 triplets states) and the spin-dependent term (where \mathbf{S}_1 and \mathbf{S}_2 , are the spins of two electrons) [14]:

$$\hat{\mathcal{H}}_{\text{Heis}} = \frac{1}{4}(E_S + 3E_T) - (E_S - E_T)\mathbf{S}_1 \cdot \mathbf{S}_2. \quad (2.7)$$

The half of the energy difference between the singlet and triplet state is called the exchange integral J , and it is defined as [14]:

$$J = \frac{E_S - E_T}{2} = \int \psi_a^*(\mathbf{r}_1)\psi_b^*(\mathbf{r}_2)\hat{\mathcal{H}}_{\text{Heis}}\psi_a(\mathbf{r}_2)\psi_b(\mathbf{r}_1)d\mathbf{r}_1 d\mathbf{r}_2. \quad (2.8)$$

Spin-dependent term of effective Hamiltonian thus can be written as:

$$\hat{\mathcal{H}}_{\text{Heis}}^{\text{spin}} = -2J\mathbf{S}_1 \cdot \mathbf{S}_2. \quad (2.9)$$

Heisenberg proposed the model of Hamiltonian, which assumes that the interaction described above applies to all neighboring atoms of the system. Thus, the generalized Heisenberg Hamiltonian takes the form [15]:

$$\hat{\mathcal{H}}_{\text{Heis}} = -2 \sum_{i>j} J_{ij} \mathbf{S}_i \cdot \mathbf{S}_j, \quad (2.10)$$

where J_{ij} is the exchange constant between i^{th} and j^{th} spins (\mathbf{S}_i and \mathbf{S}_j). The exchange integral's magnitude is determined by the degree of orbitals overlap. As the orbitals move away from each other, the overlap integral decreases. If the exchange integral value is greater than 0, the energy of the singlet state is higher than that of the triplet state, and the latter is preferred, which corresponds to ferromagnetic coupling. When the singlet state is favored ($J < 0$) the coupling is antiferromagnetic [15].

This coupling of direct exchange can either be ferromagnetic or antiferromagnetic, depending on the integral exchange value. The direct exchange interaction is strong, but it is limited to short distances only. This is because the overlap integral must be positive for exchange without intermediaries to occur. In practice, direct exchange interaction is rarely observed due to insufficient orbital overlap. For example, in REMs, the 4f electrons that carry the magnetic moment are strongly localized near the nucleus, and the probability of their orbitals overlapping is too small to allow direct exchange [15]. Even for 3d metals, where the spin-polarized orbitals extend more from the nucleus, a direct exchange may not be the primary magnetic interaction. In metals, the conduction electrons interaction cannot be neglected, and it contributes to magnetic interactions through another type of exchange interaction, namely indirect exchange interaction [14].

Indirect exchange in ionic solids – superexchange

The direct exchange cannot occur, when the distance between two magnetic ions is too large, for example when a non-magnetic ion separates them. This is the case for transition metal oxides or fluorides. Then the interaction between the 3d orbitals of transition metals occurs as a result of the hybridization of the 3d orbitals with the 2p orbitals of oxygen/fluorine. This type of indirect magnetic interaction is called superexchange [16, 17]. The exchange integral of this type interaction J_{SE} may be described by [14]:

$$J_{SE} \sim -\frac{h_p^2}{U_C}, \quad (2.11)$$

where U_C is the Coulomb energy required to make an excited state and h_p is the hopping parameter proportional to the energy width of the conduction band. The superexchange energy depends on metal–non-metal bond length and the angle between metal–non-metal–metal bonds. Figure 2.2 presents two main cases of superexchange interaction. In the first case, shown in Figure 2.2 a), all three atoms are aligned along the same axis. Due to the Pauli exclusion principle, the only possible configuration is the antiferromagnetic coupling of metal atoms. The strength of the magnetic interaction depends on the bond angle, overlap integral, and magnetic moments. In the case where the bonding of metal atoms is 90° angle, the exchange occurs in two stages similar to double exchange (described in the next paragraph). First, the interaction occurs between $d\gamma \rightleftharpoons p\sigma$ and $d\gamma' \rightleftharpoons p\sigma'$, and further, it is mediated *via* Coulomb interaction within the intermediate atom. The small overlap integral (due to the symmetry) and the possible configurations lead to the weak ferromagnetic interaction.

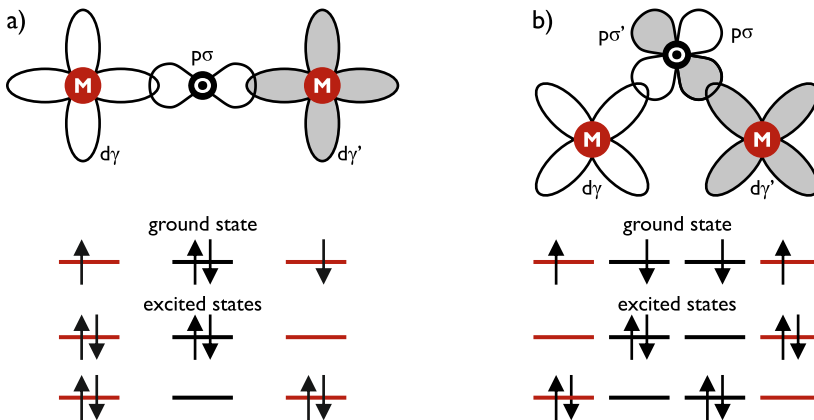


Figure 2.2: Superexchange – diagrams showing two possible scenarios of interactions between magnetic atoms mediated by non-magnetic ion: a) all three atoms are bonded along the same axis (180°) and b) bond angle between metal atoms is 90° .

Indirect exchange in magnetic ions with mixed valency – double exchange

Double exchange, also known as Zener exchange interaction, occurs between ions with mixed valency. When two ions vary with valency, the electrons are enabled to hop through the non-magnetic ion. The name double exchange comes from the two-step nature of the process that takes place during this interaction. An electron from a non-magnetic atom jumps over to a magnetic atom and is immediately replaced by an electron from a second magnetic atom. According to Hund's Rule probability of such interaction is higher when the neighboring atoms are aligned parallel, thus the ferromagnetic order is preferred. The hopping with spin reversion is also possible however, it requires more energy and thus is less likely. Hopping strongly depends on the relative orientation of the spins and the bond angle between metal–non-metal–metal and reaches its maximum value when this angle is 180° [15].

Indirect exchange in metals – RKKY

In the study of magnetic interactions in metals, it is important to consider the role of conduction electrons near Fermi energy which cannot be ignored when analyzing structures formed by atoms with localized magnetic moments surrounded by non-magnetic atoms. Atoms with strongly localized magnetic moments spin-polarize surrounding conduction electrons, which further polarizes the other magnetic atoms. This interaction is known as RKKY interaction (or itinerant exchange), named after the scientists who discovered it (Malvin Ruderman, Charles Kittel, Tadao Kasuya, and Kei Yosida). Exchange integral J_{RKKY} is described by [14]:

$$J_{\text{RKKY}}(r) \propto \frac{\cos(2k_{\text{F}}r)}{r^3}, \quad (2.12)$$

where k_{F} is a Fermi surface radius and r is a separation distance between magnetic atoms. RKKY has a relatively long range and oscillates so it can cause both ferromagnetic and antiferromagnetic ordering, depending on the separation distance between the magnetic atoms [15].

Anisotropic exchange interaction

Aside from the Heisenberg interactions, which lead to collinear magnetic ordering, there are also interactions that result in non-collinear spins' arrangement. One of them is the Dzialoshinsky-Moriya (DM) interaction, which is an antisymmetric indirect exchange that occurs in materials without inversion symmetry. This interaction requires a mediator with high spin-orbit coupling, affecting the mutual orientation of the spins in magnetic atoms. Hamiltonian of the DM interaction is described by [14]:

$$\hat{\mathcal{H}}_{\text{DM}} = - \sum_{i \neq j} \mathbf{D}_{ij} \cdot (\mathbf{S}_i \times \mathbf{S}_j), \quad (2.13)$$

where \mathbf{D}_{ij} is a DM interaction vector resulting from the interplay of two spins with the atom with large spin-orbit coupling. Initially, the spins are

arranged parallelly (see Figure 2.3 a)). In the presence of an atom with high spin-orbit coupling (see Figure 2.3 b)), the mutual configuration of the considered spins. Due to the cross-product between the spins, their relative perpendicular arrangement is preferred. As a result, the DM interaction causes the canting of spins and the formation of chiral structures, with the helicity determined by the \mathbf{D}_{ij} vector, which depends on the broken symmetry of the compound. In general, DM is not a strong interaction and is observed as a weak ferromagnetic behavior in antiferromagnetic structures. However, in materials with significant spin-orbit coupling and lack of inversion symmetry, its strength may be comparable with Heisenberg's isotropic interactions.

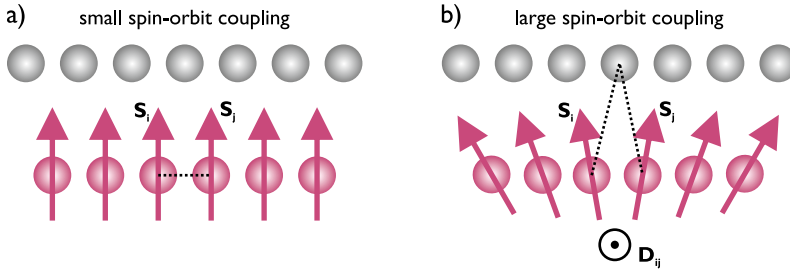


Figure 2.3: Dzyaloshinsky-Moriya interaction – schemes showing the influence of an atom with high spin-orbit coupling on the magnetic structure: a) magnetic moments arrangement without an atom with high spin-orbit coupling, b) magnetic moments arrangement in the presence of an atom with high spin-orbit coupling.

Summary of magnetic interactions

Another interaction leading to the anisotropic arrangement is the symmetric anisotropic exchange interaction, which reaches its minimum energy for the antiparallel alignment of spins. Other interactions contributing to the anisotropic arrangement are shape and crystal field anisotropies. Shape anisotropy results from the dimension confinement and it becomes significant when considering the edges of terraces or islands. Crystal field anisotropy arises from the electrostatic interactions between compounds and their intrinsic properties as orbitals shape and orientation.

The overall exchange Hamiltonian may be described using three terms: Heisenberg isotropic exchange ($\hat{\mathcal{H}}_{\text{Heis}}$), antisymmetric anisotropic exchange ($\hat{\mathcal{H}}_{\text{DM}}$), and symmetric anisotropic exchange [13]:

$$\hat{\mathcal{H}} = -\frac{1}{\hbar} \sum_{i \neq j} J_{ij} \mathbf{S}_i \cdot \mathbf{S}_j - \frac{1}{\hbar} \sum_{i \neq j} \mathbf{D}_{ij} \cdot (\mathbf{S}_i \times \mathbf{S}_j) - \frac{1}{\hbar} \sum_{i \neq j} \mathbf{S}_i \cdot \mathbf{J}_{ij}^{\text{S}} \cdot \mathbf{S}_j, \quad (2.14)$$

where \hbar is the reduced Planck's constant and $\mathbf{J}_{ij}^{\text{S}} = \frac{J_{ij} + J_{ij}^{\text{T}}}{2} - \mathbf{J}_{ij}$ is the exchange integral of symmetric anisotropic exchange (where T means transposition).

2.2 Thin films growth

The growth process of thin films, including surface alloys, occurs in three stages: nucleation, early growth, and late growth. During the nucleation stage, atoms or molecules approach the substrate. Their kinetic energy may vary from the order of tens of eV when evaporated, up to 2 – 30 eV when sputtered [18], depending on the method used to generate the beam of atoms and molecules. Before the nucleation, the substrate is exposed to incident vapor and covered with mobile atoms and clusters that grow in size with continuous vapor deposition. Various scenarios can occur after an atom collides with the substrate, as shown in Figure 2.4. An atom can desorb back to

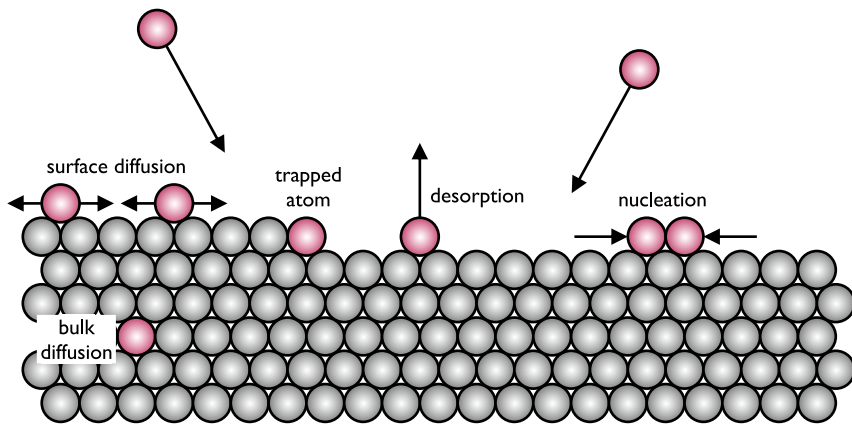


Figure 2.4: Nucleation stage – a scheme of possible scenarios of adatoms adsorption on the surface in nucleation stage.

vapor (desorption process), an adatom (adsorbed atom) can settle down and diffuse over the surface (surface diffusion process), or it can also diffuse into the bulk of the crystal (bulk diffusion process). According to Kossel’s model of crystallization, the adatom tends to form the highest possible number of bonds with the atoms on the surface [19]. On an ideally flat surface, after reaching the substrate adatom makes few bonds with the underlying atoms. However, if the strength of the interaction is weak enough, the adatom may diffuse on the surface looking for the most energetically advantageous position to adsorb. Depending on the environment in which the adatom is (how many bonds it already has), its interactions with other adatoms may vary. The substrate is not a perfectly flat single terrace but there are steps, voids, inclusions, and other defects. The adatoms often prefer to nucleate on these imperfections. For instance, they may be trapped by surface defects. At the surfaces with low density of such nucleation centers the probability of the adatoms nucleation away from these nucleation centers increases. Also with the decreased temperature the probability of such nucleation increases due to the diffusion suppression [19]. Surface diffusion leads to the nucleation and formation of islands. The thermal efficiency of the diffusion process

$D(T)$ may be described using Arrhenius equation [18]:

$$D(T) = D_0 \exp\left(-\frac{E_d}{k_B T}\right), \quad (2.15)$$

where D_0 is the temperature dependent pre-exponential factor, E_d activation energy of the diffusion process, k_B is the Boltzmann constant, and T is the temperature. After the nucleation, the early growth stage starts. Small islands start to merge in the coalescence process. The number of islands decreases which results in local exposure of the substrate where further nucleation can occur. The coalescence process occurs until the interconnected network with voids in the middle is formed. The voids shrink and are filled due to further deposition. There are two types of islands merging: Ostwald and Smoluchowski ripening [20]. Ostwald ripening is when small islands break apart and the parts diffuse to merge with larger islands causing them to grow. Smoluchowski ripening occurs when the whole islands diffuse and merge directly with the larger islands.

The general topology of a thin film's growth may be deduced in terms of the chemical potentials of the first few atomic layers. The chemical potential per atom $\mu(n)$ of n -th layer is expressed by [21]:

$$\mu(n) = \mu_\infty + [\varphi_a - \varphi'_a(n) + \varepsilon_d(n) + \varepsilon_e(n)], \quad (2.16)$$

where μ_∞ is a chemical potential of the bulk of adsorbate material, φ_a is desorption energy of deposited atom from the wetting layer (formed by the same type material as adsorbate), $\varphi'_a(n)$ is desorption energy of deposited atom from the substrate surface, $\varepsilon_d(n)$ is the misfit dislocations energy per atom, and $\varepsilon_e(n)$ is the homogeneous strain energy per atom. The values in square brackets depend in a complex way on the thickness of the growing film and the lattice mismatch between the substrate and the adsorbate layer. The growth modes are classified into three categories: island (Volmer-Webber), layer (Frank-van der Merwe), and layer plus island (Stranski-Krastanov), which are illustrated in Figure 2.5. The thermodynamic criterion for the

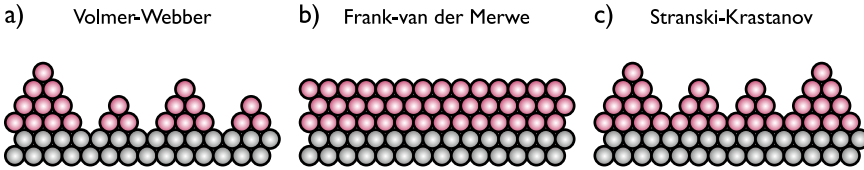


Figure 2.5: Thin films growth – a scheme of growth modes: a) island (Volmer-Webber), b) layer (Frank-van der Merwe), c) layer plus island (Stranski-Krastanov).

mechanism of thin epitaxial film growth can be defined based on the relationship between the cohesive and adhesive forces (φ_a and $\varphi'_a(n)$) and the correlation between misfit dislocations and homogeneous strain energies.

1. $d\mu/dn < 0$ when $\varphi'_a(n) < \varphi_a$ at any value of misfit – Volmer-Webber growth mode

2. $d\mu/dn > 0$ when $\varphi'_a(n) > \varphi_a$ at small misfit values – Frank-van der Merwe growth mode
3. $d\mu/dn \geq 0$ when $\varphi'_a(n) > \varphi_a$ at large misfit values – Stranski-Krastanov growth mode

The Volmer-Webber growth mode occurs when the attracting force between adatoms is much stronger than the interaction of these adatoms with the substrate thus stable clusters grow as three-dimensional (3D) islands. The opposite is observed for the Frank-van der Merwe growth mode, where the binding of adatoms with the substrate is much stronger than the interactions with other adatoms within the layer. Here, the formation of a full first monolayer (ML) before forming the next one is thermodynamically favored. The last one, the Stranski-Krastanov growth can be described by both inequalities. The initial stage follows the $d\mu/dn > 0$ and layer-by-layer growth is induced. Further, at a critical thickness, the strain induces a sign reversion of the chemical potential, and the island growth is continued. The third stage of the thin film growth process, called also the late stage of growth, refers to the interaction between structures formed in previous stages, and it not always occurs.

The growth may be controlled by deposition rate or substrate temperature. Providing additional thermal energy to the system while evaporation occurs, not only supports the diffusion process but also when this energy is high enough to exceed the energy of activation allows some phenomena to occur. The reactive growth process was involved in the preparation of samples analyzed within the dissertation. Additional thermal energy provided during the sample preparation allowed for overcoming the surface alloys activation energy and Pt overlayers formation.

Chapter 3

State of the art

Binary magnetic alloys have been widely investigated in many aspects so far. The most studied group is the system involving two transition metals. The combination of transition metals with REMs has also been well studied, while the least popular is the combination of REMs with NMs. Most of the investigations have been on bulk materials or thin films with thicknesses ranging from a few nanometers to micrometers. It is commonly known that material properties can vary significantly depending on their dimensions (3D *vs.* 2D) or thickness. This has been observed in surface alloys and their bulk counterparts, as reported in the studies [6–8].

3.1 Rare earth metals – noble metals surface alloys

There are only few reports regarding 2D surface alloys of REM-NM, and they mainly refer to Au [6–8, 22–27], Ag [27–30], and Cu [27, 31] as a NM substrates. REM-NM surface alloys can be successfully produced by reactive growth by deposition of REM on (111) face of NM single crystal held at elevated temperature [6–8, 22–29]. All of these alloys have a well-defined atomic structure with REM-NM₂ stoichiometry [6–8, 22–24], shown in Figure 3.1 a). Furthermore, they have a long-range ordered superstructure known as the moiré pattern [6–10, 22–32]. That is an interference pattern resulting from the imposition of two or more atomic lattices with varying lattice constants a , which may be additionally shifted and/or rotated with respect to each other. In the case of surface alloys, the moiré pattern appears due to the mismatch between the unit cell size of the surface alloy and the substrate, as well as the relative rotation between these lattices.

The first scientific report that pioneered further research on 2D REM-NM surface alloys focuses on the GdAu₂ surface alloy [6]. The growth temperature T of GdAu₂ ranges from 550 K to 700 K [6, 10, 26, 32]. The moiré pattern of GdAu₂ looks like a triangular net, which proved to be typical for

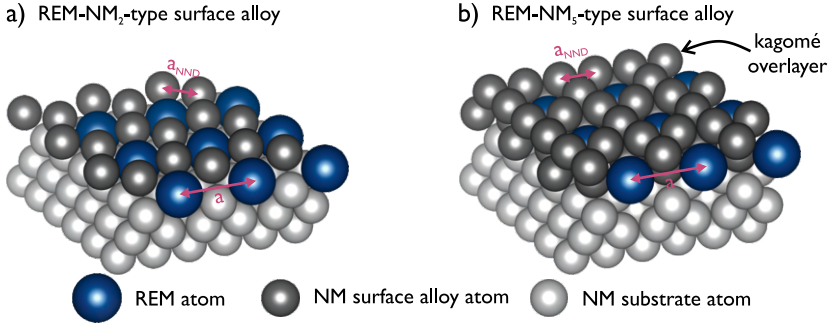


Figure 3.1: Models of REM-Pt surface alloys – with a) REMPt₂ and b) REMPt₅ stoichiometry. The main interatomic distances: the lattice constant a , and nearest-neighbor distance a_{NND} , are marked with arrows.

most REM-NM combinations. The moiré pattern lattice constant $d_{\text{moiré}}$ of GdAu₂ is between 3.7 – 3.8 nm [6, 8, 10, 23]. Further analysis has shown a bias-dependent atomic structure, allowing for the observation of the Gd and Au lattices separately [6, 8]. In the literature, there are some inconsistencies related to the terminology, so for clarity in this dissertation, a_{NND} means the nearest-neighbor distance (NND) between the closest atoms of the surface alloy, *i.e.*, lattice atoms of NM or NM-REM, while $a_{\text{REM-NM}_2}$ (surface alloy lattice constant) means the distance between the closest REM atoms that form an atomic unit cell of the surface alloy. For GdAu₂ a_{NND} is between 290 – 313 pm [6] indicating an expansion of the unit cell in comparison to its substrate ($a_{\text{Au}(111)} = 288$ pm [33]). An increase in the unit cell size is explained as a consequence of the different atomic radii of both elements [24]. Size of GdAu₂ a_{NND} is simultaneously much smaller than the typical Gd(0001) interatomic distance $a_{\text{Gd}(0001)} = 364$ pm [34]. The unit cell size varies between $a_{\text{GdAu}_2} = 511 - 550$ pm depending on the source [6, 10, 11, 23, 24]. GdAu₂ surface alloy has been identified as (110) close-packed face of the bulk GdAu₂ alloy [6]. Various studies using STM and LEED data have revealed that the moiré pattern, surface alloy, and substrate lattices rotate in relation to each other [6, 8, 11, 23]. Consistently, in multiple reports, moiré pattern found to be rotated relative to the alloy lattice $\alpha_{\text{m-a}}$ about 30° [6, 11]. A detailed analysis of the 2D fast Fourier transform of the large-scale STM atomic resolution image found the rotation more precisely to be $30.80 \pm 0.15^\circ$. However, it is still unclear whether the moiré pattern rotation ($\alpha_{\text{m-s}}$) and surface alloy rotation ($\alpha_{\text{a-s}}$) relative to the substrate are 0° and 30° [6] or 33° and 5° [23], respectively, as reported in different studies. The moiré pattern corrugation of 60 pm mainly results from the vertical modulation of the surface alloy atoms that are adsorbed in various positions relative to the substrate [23]. Displacement of the Gd and Au atoms results not only from the buckling due to the differences in their atomic radii but also from the adsorption sites. There are three possible configurations, depending on the relative position of surface alloy atoms to the substrate: top, fcc, and hcp. Theoretical calculations of the GdAu₂ surface alloy relaxation showed that,

depending on the adsorption site, the coupling of the surface alloy with the substrate can differ in strength which also affects the distance between the atoms of the surface alloy and the substrate [23]. In addition, moiré pattern corrugation also depends on the scanning parameters, *i.e.*, the bias voltage. This suggests some contribution originating from electronic states. However, the corrugation factor induced by changes in the density of states (DOS) is relatively small compared to the dominant impact of vertical displacements of surface alloy atoms [23]. The surface alloy GdAu₂ exhibits ferromagnetic order with an in-plane easy magnetization axis, unlike the antiferromagnetic bulk GdAu₂ alloy [8, 9]. In the case of bulk alloy, the structure frustration leads to antiferromagnetic coupling of Gd atoms of adjacent alloy layers *via* RKKY interaction. The formation of a surface-confined structure allows for the natural ferromagnetic state of the Gd crystal to occur. The coercive field H_C was found to be 2 mT using magneto-optic Kerr effect [28] and 17.5 mT using spin-polarized STM [8]. The Curie temperature T_C is estimated to be 19 ± 5 K. The atomic resolution investigation revealed the influence of defects, such as dislocation lines, on the structural and magnetic properties. The surface alloy domains separated by the dislocation line are shifted by half of a unit cell with respect to each other [8].

Another phase of GdAu₂ namely double layer (2 L) GdAu₂ has been investigated when a larger amount of Gd is deposited [7]. It grows in a Frank-van der Merwe mode, but its layer stacking is different from that of the bulk GdAu₂ [7]. Similarly to GdAu₂ surface alloy, it exhibits ferromagnetic order, and its lattice constant is about 543 pm, which is similar to that of single layer GdAu₂ case. X-ray photoelectron diffraction data suggests that the distance between two alloy layers d is approximately 220 pm, which agrees well with the theoretically calculated relaxed structure of 240 pm. With higher Gd coverage, the moiré pattern changes to a tile-shaped pattern with locally broken periodicity. The apparent corrugation decreases, indicating stress relief of the structure [27], while its lattice constant remains unchanged [7].

Apart from GdAu₂, many other REMs are shown to form surface alloys with NMs such as Au(111), Ag(111), and Cu(111). Tables 3.1 and 3.2 summarize the structural and growth parameters, as well as the magnetic and electronic properties of all surface alloys investigated so far. In all cases, alloy formation occurs during a reactive growth process, with a substrate temperature ranging from 470 K to 750 K, and is more dependent on the REM type than on the NM substrate. They all share a well-defined atomic structure with REM-NM₂ stoichiometry that differs with interatomic distances, resulting in surface alloy lattice constants in the range 490 – 550 pm. The difference between the atomic radii of the constituent elements and their interaction with each other has the greatest effect on the $a_{\text{REM-NM}_2}$ value. It also influences long-range order, resulting in various $d_{\text{moiré}}$ in range 3.1 – 3.8 nm for Au(111)-based surface alloys, 2.1 – 2.5 nm for Cu(111)-based surface alloys, and 3.2 – 4.6 nm for Ag(111)-based surface alloys.

Table 3.1: REM-NM state of the art – overview of REM-NM surface alloys’ structural and growth parameters: alloy formation temperature and structural parameters.

surface alloy	growth T (K)	$d_{\text{moiré}}$ (nm)	$a_{\text{REM-NM}_2}$ (pm)	a_{NND} (pm)	$\alpha_{\text{m-a}}$ (°)	$\alpha_{\text{a-s}}$ (°)
LaAu ₂	780 [22]	3.2 ± 0.2 [22]	530 ± 30 [22]	310 ± 20 [22]	30 ± 4 [22]	30 [22]
CeAu ₂	750 ^a [22]	3.3 ± 0.2 [22]	540 ± 30 [22]	310 ± 20 [22]	30 ± 4 [22]	30 [22]
EuAu ₂	575 [26]	3.3 ± 0.1 [26]	550 [26]		30 [26]	30 [26]
GdAu ₂	550 [6, 10]		511 [23]			
	600 ^b [32]	3.7 [8, 23]	530 [23]	313 [6]	30 [6, 11]	30 [6]
	675 [26]	3.8 ± 0.2 [6, 10]	$540 [11, 24]$		30.80 ± 0.15 [8]	
	690 [9]		550 [6, 10]			
2 L GdAu ₂	550 [7]		543 [7]			30 [7]
TbAu ₂	573 [25]	3.68 ± 0.10 [25]	540 ± 20 [25]		30.0 ± 0.2 [25]	30 [25]
DyAu ₂	570 – 630 [27]	3.6 – 3.7 [27]	550 ± 30 [27]			30 [27]
HoAu ₂	573 [25]	3.66 ± 0.05 [25]	540 ± 10 [24, 25]		30 [24, 25]	
	693 [24]	3.76 ± 0.10 [24]				
ErAu ₂	573 [25]	3.76 ± 0.04 [25]	540 ± 10 [25]		30 [25]	
YbAu ₂	573 [24]	3.65 ± 0.10 [24]	540 [24]		30 [24]	
GdAg ₂	600 [28]	3.2 ± 0.1 [28]	$515 - 560$ [29]	300 [28]	30 [28]	30.0 ± 4.5 [28]
		$3.2 - 3.4$ [29]	520 ± 10 [28]			
DyAg ₂	575 [30]	4.62 [30]	520 ± 30 [27]			30 [27]
	570 – 630 [27]		510 ± 15 [30]			
DyCu ₂	570 – 630 [27]	2.1 – 2.5 [27]	520 ± 30 [27]	288 [27]	18.8 [27]	28 – 29 [27]
ErCu ₂	473 [31]	2.47 ± 0.10 [31]	490 ± 20 [25]	280 ± 10 [31]		30 [31]

The surface alloys GdAg₂ and DyAg₂ exhibit intricate tessellated moiré patterns, consisting of hexagonal antiphase domains surrounded by domain walls [27]. Similarly, GdAu₂ shows a disrupted triangle-shaped moiré pattern due to dislocation lines separating two domains [8]. All investigated surface alloys display a rotation relative to the substrate and moiré pattern lattices. In most studies, the rotation between the surface alloy lattice and the NM substrate is 30°, similar to the rotation between the moiré pattern lattice and the surface alloy which is 30°. Depending on the method chosen to determine the angle, the values may differ slightly.

Magnetic studies have been conducted on several surface alloys, re-

^a gives 70% of the sample covered with surface alloy

^b with subsequent post-annealing in 700 K gives the best quality of the surface alloy

^c value obtained using XMCD method

^d value obtained using magneto-optic Kerr effect method

Table 3.2: REM-NM state of the art – overview of REM-NM surface alloys’ magnetic and electronic properties: Curie temperature, coercivity, easy magnetization axis, and work function.

surface alloy	T_C (K)	H_C (mT)	easy magnetization axis	$\phi_{\text{REM-NM}_2}$ (eV)
EuAu ₂	13 [26]		out-of-plane [26]	
GdAu ₂	19 ± 5 [32]	17.5 [8] 2 [28]	in-plane [8, 9]	
2 L GdAu ₂				4.72 [7]
TbAu ₂				4.25 ± 0.10 [25]
HoAu ₂	22 [24]		out-of-plane [24]	4.3 [25]
ErAu ₂				4.3 [25]
GdAg ₂	75 ± 5 ^c 85 ± 5 ^d [28]	1 [28]	in-plane [28]	

vealing strong magnetic anisotropy. GdAu₂ and GdAg₂ have an in-plane easy magnetization axis, with different T_C values of 19 K [32] and 85 K [28], respectively. In contrast, EuAu₂ and HoAu₂ exhibit an out-of-plane easy magnetization axis with T_C values of 13 K [26] and 22 K [24], respectively. This leads to the conclusion that T_C depends not only on substrate type but also on the involved REM. Some of the Au(111)-based surface alloys have been investigated in terms of their work function $\phi_{\text{REM-NM}_2}$, which generally falls between the substrate ϕ_{NM} and REM’s ϕ_{REM} work function. For instance, the estimated ϕ_{TbAu_2} is 4.3 ± 0.1 eV [25], which is between the Au(111) (5.31 eV [35]) and Tb (3 eV) work functions. In other cases, the values of the work functions are of a similar order: $\phi_{\text{HoAu}_2} = 4.3$ eV [25], $\phi_{\text{ErAu}_2} = 4.3$ eV [25], $\phi_{2\text{LGdAu}_2} = 4.72$ eV [7].

3.2 Rare earth metals – Pt compounds

In the previous Subsection, it was demonstrated that changing the material of the substrate and REM leads to a significant improvement in the properties of surface alloys. The Néel temperature change was already observed in bulk alloys, where it is 9 K for DyAg₂ and 31 K for DyAu₂ [36]. This is also true for surface alloys, where in the case of Gd compounds, the T_C changes from 19 K to 85 K for GdAu₂ and GdAg₂, respectively [28]. Subsection 3.1 focuses on 2D surface alloys of REMs with NMs, including Au, Ag, and Cu. Another worth noting NM is *platinum*. First, Pt does not carry any magnetic moment and behaves like a paramagnet but its contribution to magnetic properties is not negligible [37]. Pt is easily polarizable and when forming alloys serves as a mediation center between magnetic REM atoms.

It is expected that due to the easy polarization, Pt will demonstrate stronger coupling in RKKY magnetic exchange interaction compared to other NM. Second, Pt also has very high spin-orbit coupling, which may influence the electronic and magnetic structure of surface alloys. In atomic resolution scale measurements, non-collinear magnetic order resulting from DM interaction may be observed. Pt is also the base element of the proton exchange membrane fuel cell cathodes due to its high activity toward the oxygen reduction reaction. The great potential of proton exchange membrane fuel cells as a new energy-efficient power source forced the search for new materials with lower Pt loadings, enhanced catalytic properties, and long-term stability under working conditions. The alloying of Pt with REMs has been found to improve activity significantly [38–40], with GdPt_5 and YPt_3 being the most active polycrystalline alloys based on Pt for the oxygen reduction reaction, showing a six-fold improvement in activity over pure Pt [41, 42]. In this regard, the Gd-Pt system is mainly studied in terms of polycrystalline and thick-film samples and their catalytic properties [39–49].

Bulk REM-Pt alloys

Bulk Gd-Pt compounds can take many phases, depending on the Gd:Pt ratio [50]. GdPt has FeB structure type [50, 51] and is ferromagnetic with T_C about 66.0 – 67.6 K [52, 53]. GdPt_2 with MgCu_2 cubic structure is also ferromagnetic [54, 55] but its Curie temperature is not clear. Taylor *et al.* estimated T_C as 22 K [54], while Wallace and Vlasov obtained 47 K [56]. Taylor *et al.* explain the difference in T_C as a dependence on the Gd amount, which is a complex function with a minimum for $\text{GdPt}_{2.33}$ [54]. Theoretical calculations by Baranovskiy *et al.* pointed to a T_C as 135 K, while their experimentally determined value is 46.5 K [55]. GdPt_5 adopts a hexagonal CaCu_5 and orthorhombic AuBe_5 structure [43, 50]. It is also ferromagnetic, with T_C of 13.9 K [57]. Gd-Pt system may also forms Gd_3Pt_4 with rhombohedral structure and GdPt_3 with AuCu_3 cubic structure [50].

Bulk Dy-Pt compounds are mainly studied as DyPt_2 alloys. This alloy is known to be a ferromagnet, but its T_C value is not clearly defined. Some studies suggest that it can be 25 K [56], while others indicate that it may depend on the strength of the magnetic field, reaching 9.2 K for 10 mT and 29 K for 8 T [58]. The coercive field of DyPt_2 is 66 mT. Additionally, it is possible that this alloy may exhibit a non-collinear structure while in a ferromagnetic state [58].

Studies comparing various bulk polycrystalline REM-Pt_5 alloys have led to some general observations. In principle, bulk REM-Pt_5 exhibit either hexagonal CaCu_5 or orthorhombic AuBe_5 structures [39, 42, 43, 50]. The basic difference between these two phases is the stacking of layers, which results in different c parameters of the unit cell. However, the a parameter of the unit cell is the same for both compositions. The covalent radius of REMs decreases toward REMs with a higher atomic number, resulting in a contraction of $a_{\text{REM-Pt}_5}$ [43]. Due to the difference in atomic radii of REM and Pt, lateral compressive strain occurs. This strain is defined as the rela-

tionship between the a_{NND} of the alloy layer compared to a_{NND} of the pure Pt layer. As a result of the contraction of the lanthanide atomic radii, the compressive strain increases [43]. In catalytic studies, Pt overlayer formation occurs as a result of the oxygen reduction reaction. This Pt overlayer provides the kinetic stability of the alloy against dissolution and is usually of a few atomic layers thick [38, 40, 42, 44]. Additionally, the Pt overlayer forms when the alloy is annealed at a high enough temperature, which depends on the REM and is approximately a single layer thick [48].

Size-confined REM-Pt compounds

Due to the numerous coverage unit definitions used within analyzed literature, in this work, I will use the reference unit – unit cell (u.c.), which is the amount of REM required to form a unit cell thick layer of the REM-Pt₅ alloy. Some authors use alternative definitions such as the monolayer (ML) unit, which is defined as a layer of REM atoms with a thickness of one atom. The 1 ML coverage REM amount corresponds to 3 u.c. Alternatively, some authors use the layer thickness in Angstrom, as a definition of REM coverage, which after conversion gives that 10 Å is equal to 2 MLs or 6 u.c.

The Ce-Pt system is the most extensively studied in terms of the structural properties of dimensionally confined systems. However, the results have revealed a wide variety of surface structures and the conclusions are inconsistent, making it difficult to interpret the structural properties of REM-Pt surface alloys. Generally, REM-Pt₅ bulk alloys consist of alternating REM-Pt₂ and kagomé Pt₃ layers [42, 53]. For quasi-2D systems, there are predictions of a more complex structure resulting from rotations of these layers with respect to each other, their stacking sequence, and even the presence of different stoichiometry layers, such as REM₂-Pt layer or hexagonal pure Pt layer (Pt₄) [48, 59, 60]. The model of the REM-Pt₅ surface alloy is shown in Figure 3.1 b).

The first studies using x-ray photoelectron spectroscopy and LEED by Tang *et al.* showed that the intermixing of Ce with Pt atoms starts above 770 K regardless of the Ce coverage in the range starting from below 3 u.c. (submonolayer) up to about 16 u.c. (5.4 MLs). They identified the coverage corresponding to 3 u.c. (1 ML) of Ce using the x-ray photoelectron spectroscopy Ce-Pt intensity ratio before annealing [61]. Tang *et al.* identified three different alloy structures within investigated Ce coverages, while Baddeley *et al.* using a higher temperature (1000 K) recognized five different structures using LEED and STM within a slightly smaller Ce coverage range *i.e.* from below 3 u.c. (submonolayer) to 9 u.c. (3 MLs). They also pointed out that Tang *et al.* misestimated the coverage. Baddeley *et al.* estimated the coverage of 3 u.c. (1 ML) using the Auger intensity of Ce (82 eV), and according to their findings, it is approximately half that assigned to 3 u.c. (1 ML) in Tang *et al.* studies [59]. In 2009 Essen *et al.* investigated the temperature-dependent behavior of the low-dimensional Ce-Pt system for the first time and observed a LEED pattern evolution for consecutive annealing temperatures in the range from below 800 K to 1000 K [62]. Five

years later, Kemmer *et al.* presented comprehensive studies of coverage-dependent structures in a wide range of 1 u.c. to 11 u.c. [63]. Further investigations supported by theoretical calculations by Praetorius *et al.* and Ienaga *et al.* focused not only on the alloy structure but also on termination layer analysis [60, 64, 65]. Despite multiple studies, there is still no clear interpretation of the structure and growth conditions for the Ce-Pt system, and many ambiguous conclusions are drawn.

For the lowest of investigated Ce coverage – 1 u.c., Kemmer *et al.* found $(2 \times 2) + (1 \times 1)$ coexisting LEED patterns [63]. For the same coverage, Praetorius *et al.* observed only the (2×2) LEED pattern without fingerprints of the Pt(111) signal [64]. The same was the case for Ienaga *et al.* and they assigned (2×2) LEED pattern to 1 ML of the CePt₆ structure with Pt kagomé interface layer and hexagonal Pt₄ termination layer [60]. In the case of 2 u.c. Kemmer *et al.* observed (1.98×1.98) also called compressed (2×2) , which they identified as several layer thick, and CePt₂ terminated structure [63]. Similar (2×2) pattern was observed by Praetorius *et al.* [64]. For Ce coverage in the range between 1 u.c. – 2 u.c. (in publication determined as submonolayer regime), Tang *et al.* and Essen *et al.* reported an unchanged Pt (111) (1×1) LEED pattern [61, 62]. For coverage between 2 u.c. – 3 u.c. (in publications determined as submonolayer regime) Baddeley *et al.*, and Berner *et al.*, and Essen *et al.* observed modified surface structures [59, 62, 66, 67]. Baddeley *et al.* noted the $(5.6 \times 5.6)R30^\circ +$ weak (1.95×1.95) LEED pattern and $(5.4 \times 5.4)R30^\circ$ structure based on STM. They interpreted it as 1 ML of CePt₅, which is terminated with Pt kagomé layer [59]. Berner *et al.*, on the other hand, recognized islands aggregated at the step edges. However, they observed an island with no high degree of order when annealing at 900 K. Only samples annealed to 1000 K revealed two ordered structures, which they identified as CePt₅ [66, 67]. Essen *et al.* observed ideal structures (2×2) for 800 K and its evolution to $(2 \times 2) + (1.98 \times 1.98)R30^\circ$ for 900 K – 1000 K [62]. The further increase in coverage to 3 u.c. – 6 u.c. (1 ML – 2 MLs) also presents conflicting results. Tang *et al.* observed LEED patterns $(1.94 \times 1.94) +$ satellites and $(1.96 \times 1.96) +$ satellites assuming that they are derived from the CePt₃ Pt-terminated structure [61]. Baddeley *et al.* found the coexistence of (1.95×1.95) and similar to $(5.6 \times 5.6)R30^\circ$. The former is assigned to CePt₅ covered with an additional CePt₂ overlayer [59]. Essen *et al.* observed $(2 \times 2) + (1.98 \times 1.98)R30^\circ$ with satellites [62], while Kemmer *et al.* observed compressed $(2 \times 2)R30^\circ$ pattern with satellites, which is alternatively called $(\frac{10}{9}\sqrt{3} \times \frac{10}{9}\sqrt{3})R30^\circ$ [63]. A similar pattern was identified by Praetorius *et al.* They observed $(\frac{10}{9}\sqrt{3} \times \frac{10}{9}\sqrt{3})R30^\circ$ with satellites for coverage of 3 u.c. and $(\frac{10}{9}\sqrt{3} \times \frac{10}{9}\sqrt{3})R30^\circ$ without satellites for coverage of 5 u.c. Coverages above 6 u.c. (2 MLs) led Tang *et al.* to LEED pattern $(1.96 \times 1.96) + (1.96 \times 1.96)R30^\circ$. The structure was determined as CePt_{2+x}, where $x = 0.45 - 0.55$. Higher coverage, above 10 u.c. (3.5 MLs) changes the Ce:Pt ratio and x is equal 0.23 then [61]. Baddeley *et al.* observed the (1.95×1.95) LEED pattern with satellites and the coexistence of $(1.95 \times 1.95) + (1.95 \times 1.95)R30^\circ$, depending on the anneal-

ing temperature for 6 u.c. (2 MLs) coverage. The former is observed for 800 K, and the latter for 1000 K. Coverages above 9 u.c. (3 MLs) revealed only the coexistence of $(1.95 \times 1.95) + (1.95 \times 1.95)R30^\circ$ [59]. Similarly, Essen *et al.* noticed (1.98×1.98) for 6 u.c. (2 MLs), and the coexistence of $(1.98 \times 1.98) + (1.98 \times 1.98)R30^\circ$ for 9 u.c. (3 MLs) [62]. In Tang *et al.* studies, all surfaces were expected to be Pt-rich. More insightful analysis of Baddeley *et al.*, Kemmer *et al.*, and Praetorius *et al.* revealed a variety of structures that differ with reactivity. This clearly points to different termination layers. It is either mixed CePt_2 , pure Pt with kagomé Pt_3 or hexagonal Pt_4 symmetry.

There is a small number of literature about alloying Pt with other REM, however, there are few noteworthy publications. One such report involved the deposition of 3 u.c. (1 ML) [68, 69] and 6 u.c. (10 Å) [70, 71] of La, followed by post-annealing at 873 – 973 K. This resulted in the formation of relatively inert structures that are most likely Pt-terminated and have a LEED pattern of (2×2) . A similar result was obtained by depositing 3 – 6 u.c. (1 – 2 MLs) of Tm. The formation of alloys starts at 823 K and up to 1073 K forming a sharp LEED (2×2) pattern. Above that temperature, some satellite spots become visible [72]. A study by Ulrikkeholm *et al.* investigated the Gd-Pt system involving different growth modes and coverages ranging from 12 – 380 u.c. (2 – 63 nm) [48]. They observed Gd oxidation directly after deposition, therefore to remove the contamination, the surface was sputtered prior to annealing and alloy formation. Deposition of 12 u.c. (2 nm) thin Gd layer and subsequent post-annealing process at 473 K showed that the surface is Gd dominated. The intermixing process starts at 773 K, while at 1073 K the Pt overlayer forms, analogous to the Tm case. To simulate the bulk GdPt_5 alloy, a thicker Gd layer of 120 u.c. (20 nm) and a reactive growth process with 1073 K were involved. In such a case, two energetically similar structures (1.9×1.9) and $(1.9 \times 1.9)R30^\circ$ were observed with the same probability within the preparation processes. The authors claim that the resulting structure does not behave as a bulk GdPt_5 crystal. Its structure was predicted as a complicated composition of 18 layers with non-equal distances between layers. It consists of alternating and shifted layers: Pt_3 kagomé, mixed hexagonal GdPt_2 and Gd_2Pt , Pt_4 hexagonal pure Pt [48].

The various REM-Pt structures, which differ in their structural and chemical properties, suggest that their formation is more sensitive to the coverage and temperature differences than in the case of REM with Au, Ag, or Cu systems. Thus, differences in interpretations may result from the use of different temperatures or ambiguously estimated REM surface coverage. Such an inconclusive analysis shows the complexity of REM-Pt systems and suggests the need for a deeper understanding of this topic.

Chapter 4

Methods

The following Chapter describes both experimental and theoretical methods used to investigate 2D surface alloys in this dissertation. The primary experimental instrument used to investigate local structural and electronic properties is an STM. A detailed description of its construction and operating principle are presented in the first Subsection. Further, the concept of tunneling, starting with elastic tunneling through a one-dimensional potential barrier and ending with the Tersoff-Hamann approach is introduced. Next, STM imaging operating modes and differential conductance measurements are described. In the following Subsections, principles of global averaging techniques used for the characterization of structural (LEED), chemical (AES), and magnetic properties (XMCD) are described. These Subsections contain a general description of the techniques as well as the operation principles and setup construction. Finally, the last Subsection provides the basics of the supporting theoretical technique (DFT) and implemented codes.

4.1 Scanning tunneling microscopy

Scanning tunneling microscopy (STM) allows for the local investigation of electronic properties in real space with atomic resolution. Its operating principle is based on a quantum-mechanical phenomenon known as the quantum tunneling effect, described in detail in Section 4.1.1. In terms of classical physics, crossing through the barrier with higher energy than the energy of the particle itself is impossible. In quantum mechanics, however, considering wave-particle matter duality, there is a certain probability for such electrons to overcome the barrier [73]. The first successful tunneling experiment was conducted in 1981 by Gerd Binnig, Heinrich Rohrer, Christoph Gerber, and Eduard Weibel from the Zurich Research Laboratory of International Business Machines. They published results of the experiment proving the exponential dependence of the tunneling resistance on the distance between the two electrodes – a tungsten probe and a platinum plate [74]. This experimental confirmation of exponential dependence of tunneling resistance on

the distance between electrodes, and thus its enormous sensitivity, together with the possibility of continuous measurement of variations in tunneling current gave rise to the concept of using this phenomenon in the study of surface morphology. The results they showed are recognized as the first step towards designing the STM, and 1981 is considered the date of its birth. Merely one year later, the practical application of the tunneling effect in terms of surface research resulted in the publication describing the principle of operation of STM [75]. Its usefulness was confirmed by the first STM image with atomic resolution, showing the topography of the reconstructed Si(111) silicon surface with the (7×7) reconstruction [76]. In 1986, Gerd Binnig and Heinrich Rohrer were recognized with the Nobel Prize "for their design of the scanning tunneling microscope" [77]. This pioneering research gave rise to the development of scanning probe microscopy-related techniques. The illustrative setup scheme of STM is shown in Figure 4.1. Although I used various STM systems for the research presented in the dis-

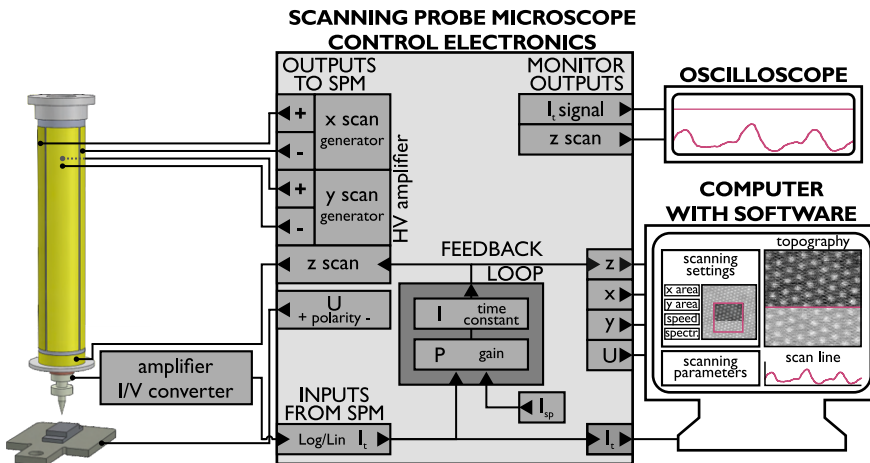


Figure 4.1: Scanning tunneling microscopy – a scheme of the experimental realization of an STM setup along with devices for control and signal processing.

sertation, they all have the same configuration, therefore I will describe only that type of STM setup. The scanning probe is housed in the piezoscanner using a special probe holder. The motion of the probe is possible by the use of piezoelectric materials. These are the materials that deform (contract/expand or bend) due to the applied voltage (applied electric field). This phenomenon is known as the reverse piezoelectric effect. Precise movement of the probe is provided by a piezoelectric scanner [78], which in this case is a piezoelectric tube. The tube is covered with one inner electrode, called z electrode, and four outer electrodes $x+$, $x-$, $y+$, and $y-$. Outer electrodes provide a raster scan of the sample's surface, while the z electrode is responsible for the movement in a normal direction to the sample's surface. Various scenarios of the energy level diagrams interactions between two electrodes (probe and sample) are shown in Figure 4.2. Assuming temperature equal to 0 K and large separation distance between electrodes, their

electrons occupy electronic states up to the Fermi levels of probe $E_{F,p}$ and sample $E_{F,s}$ (see Figure 4.2 a)). Electrons are kept within the metal due to the potential barrier, which height is called work function ϕ . That is the energy needed to remove an electron from a solid with Fermi energy E_F to the vacuum at infinite distance $E_{vac} = E_F + \phi$. When the probe and sample are approached, the narrowing of the potential barrier between electrodes allows for tunneling. The electrons tunnel between electrodes so their Fermi levels equalize (see Figure 4.2 b)). After reaching this equilibrium point the same number of electrons tunnel from probe to sample, as the other way around, and the net tunneling current is equal to zero. Whenever the probe and sample differ with work functions ($\phi_s \neq \phi_p$) the barrier adopts a trapezoidal shape. To keep the tunneling current flowing, a bias voltage U (in the range of up to a few volts) is applied between the sample and the probe. In such case $E_{F,p}$ and $E_{F,s}$ are shifted with respect to each other by eU , where e is an elementary charge. Depending on the voltage polarity, electrons can tunnel between the probe's atoms and the sample surface's atoms or the other way around, revealing occupied or unoccupied states. In the setups I worked on, the probe is grounded, and the U is applied to the sample. Using this convention, positive U will cause tunneling of electrons from the probe to the sample, revealing unoccupied sample states (see Figure 4.2 c)). On the other hand, negative U will result in the tunneling from the sample to the probe reproducing occupied sample states (see Figure 4.2 d)) [73, 79]. Before tunneling occurs, it is necessary to approach the probe close enough

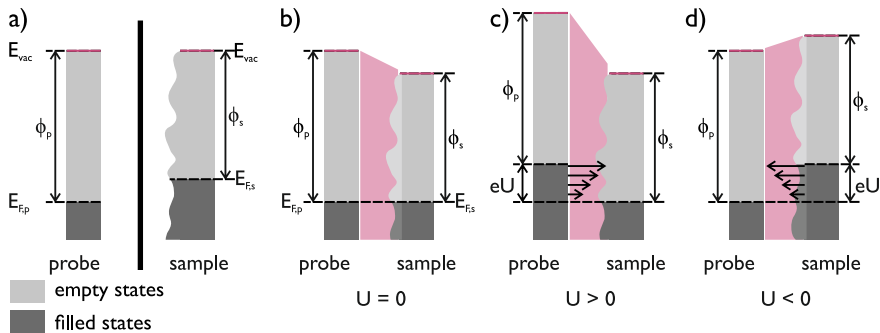


Figure 4.2: Energetic level diagrams in STM setup – a) energetic levels configuration when probe-sample distance is too large to enable tunneling, b) equilibrium configuration for decreased probe-sample distance allowing for tunneling without applied bias voltage, c) energetic level diagrams for positive applied bias, d) energetic level diagrams for negative applied bias.

to the sample so that their wave functions (ψ_p and ψ_s) overlap. The coarse approach is achieved by the combination of piezostacks with the piezoscaner movement in the z direction. The piezoscaner with the probe inside moves towards the sample while extending, and the tunneling current is monitored. If the current signal is lower than the user-specified tunneling current setpoint I_{sp} for the fully extended scanner, the scanner retracts and the piezostacks take a step towards the sample. This process is repeated un-

til the tunneling current signal I_t reaches the desired value of I_{sp} . The probe and sample must be close enough to overlap their orbitals then tunneling of electrons with energy lower than the potential barrier may occur. In practice, the typical probe-sample distance allowing for tunneling of electrons is approximately 0.3 – 1 nm in UHV conditions (the exact value depends on the investigated sample surface and the value of U) [79]. I_t can reach values from a few pA to even several hundred nA. It is convenient to convert such a small current signal to a voltage signal. This is achieved using a current-voltage (I/V) converter combined with a preamplifier with a gain in the range of $10^7 - 10^9$. Further, I_t is processed by STM control electronics and/or lock-in depending on the selected operating mode. Operating modes are described in detail in Subsections 4.1.2 and 4.1.3. Briefly, I_t is fed to the STM electronics and (1) registered as an image in constant height mode, (2) used as a reference signal for the feedback loop that keeps the constant I_t value in constant current mode or (3) registered as a I_t signal. Within the differential conductance measurements, the I_t is split and additionally, it is fed to the lock-in whence, after processing, the lock-in output signal is fed to the STM electronics. The electronics are connected to a computer, allowing the user to adjust and control operating parameters and process gathered signals. The research carried out within the dissertation was performed using analog electronics from RHK Technology, Inc. The control units allow the user to set parameters such as U , bias polarity, I_{sp} , feedback loop parameters (time constant and gain), initial sample position x , y , z , and slope compensation parameters. The same control unit also allows the user to monitor the parameters such as x , y , z , I_t , and U in real-time. The second control unit is responsible for the coarse approach. Additionally, some operation values are provided by software (scanning speed, image area size, spectroscopy mode, spectroscopy position, *etc.*). Output signals from the control units are visualized in the software to display experimental results.

4.1.1 Theoretical concept of tunneling effect

Quantum tunneling is a complex phenomenon that cannot be explained in terms of classical physics. According to classical physics, a particle cannot pass through a barrier with higher energy than its own. However, electrons are quantum-mechanical particles, and the principles of quantum mechanics are used to describe their properties accurately. The wave-particle duality concept explains that there is a certain probability for a particle to pass through a potential barrier with higher energy than the energy of the particle.

Elastic tunneling through a one-dimensional potential barrier

The simplest model to represent quantum tunneling is elastic tunneling through a one-dimensional potential barrier. In this model, the STM is simplified to the one-dimensional model where the vacuum represents the potential barrier with height V and width a , while the probe and the sample are represented by the left and right side of the barrier, respectively, as shown in Figure 4.3. In quantum physics, a particle with energy E and mass

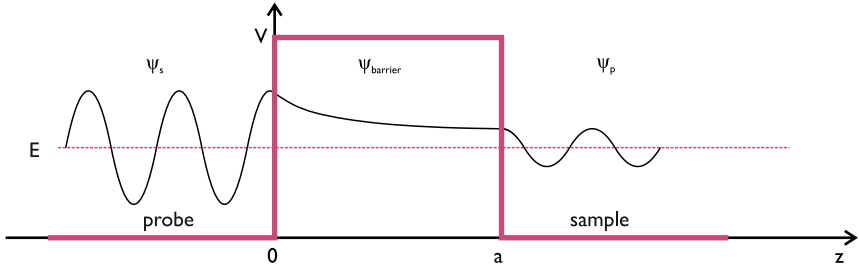


Figure 4.3: The tunneling effect – scheme of one-dimensional quantum tunneling of a particle with energy E through a potential barrier with height $V > E$, and width a . The wave functions of tunneling electron with energy E within three regions: sample, barrier, and probe are denoted ψ_s , ψ_{barrier} , and ψ_p , respectively.

m_e can be described by a wave function ψ that follows the one-dimensional time-independent Schrödinger equation:

$$-\frac{\hbar^2}{2m_e} \frac{d^2}{dz^2} \psi(z) + V(z)\psi(z) = E\psi(z), \quad (4.1)$$

where \hbar is Planck's constant divided by 2π . The wave functions for three regions can be described by:

$$\psi_s = e^{ikz} + Ae^{-ikz}, \quad (4.2)$$

$$\psi_{\text{barrier}} = Be^{-\kappa z} + Ce^{\kappa z}, \quad (4.3)$$

$$\psi_p = De^{ikz}, \quad (4.4)$$

where the A , B , C , and D are coefficients related to the reflection and transmission of the electron through the barrier, and they are calculated from functions and their derivatives at the interfaces: sample–barrier and barrier–probe, $k = \frac{\sqrt{2m_e E}}{\hbar}$ is a wave vector, and $\kappa = \frac{\sqrt{2m_e(V-E)}}{\hbar}$ is the decay constant that describes an electron permeating the barrier in $z+$ direction. In the barrier area, the electron can move in both $z+$ and $z-$ directions. The barrier transmission coefficient is defined as a relationship between incident probability current j_i and transmitted probability current j_t [79]:

$$j_i = \frac{\hbar k}{m_e}, \quad (4.5)$$

$$j_t = -i \frac{\hbar}{2m_e} \left(\psi_p^*(z) \frac{d}{dz} \psi_p(z) - \psi_p(z) \frac{d}{dz} \psi_p^*(z) \right) = \frac{\hbar k}{m_e} |D|^2, \quad (4.6)$$

$$\frac{j_t}{j_i} = |D|^2 = \frac{1}{1 + \frac{(k^2 + \kappa^2)^2}{4k^2 \kappa^2} \cdot \sin^2(\kappa a)}. \quad (4.7)$$

Assuming strong attenuation ($\kappa a \gg 1$), transmission coefficient can be approximated to [79]:

$$T_r \approx \frac{16k^2 \kappa^2}{(k^2 + \kappa^2)^2} \cdot e^{-2\kappa a}. \quad (4.8)$$

From the above approximation, some general conclusions can be drawn. The dominant factor contributing to T_t is the $\exp(-2\kappa a)$ factor, which explains the high sensitivity of STM. Changing the barrier width by approximately 1 Å leads to a decrease in I_t by one order of magnitude. This implies that the tunneling process only occurs between the sample and the most prominent atom of the probe. Another factor that influences I_t is the decay rate, which is the square root of an effective barrier height $\sqrt{V - E}$.

Bardeen's approximation

The derivation above only applies to a one-dimensional system and mainly describes the dependence of I_t on the spacing between the probe and sample, without considering the contribution from DOS of the sample and probe. In 1961, John Bardeen introduced a theory that describes the tunneling of electrons between two metal electrodes separated by a thin oxide layer [80]. This theory can also be used to explain tunneling in STM [81]. In Bardeen's theory, the probe and sample are two independent subsystems, that weakly interact with each other through overlapping wave functions of both subsystems. He independently solved Schrödinger equation for both sample and probe and then derived an expression describing the probability of a transition between two quantum states of a system under the influence of a periodic perturbation, using time-dependent perturbation theory and Fermi's Golden Rule. After these approximations, I_t corresponds to the transfer of electrons between the two sub-systems summed over all τ states of probe p and ν states of sample s, and is expressed by [80]:

$$I_t = \frac{2\pi e}{\hbar} \sum_{\nu, \tau} \{f(E_\tau)[1 - f(E_\nu + eU)] - f(E_\nu + eU)[1 - f(E_\tau)]\} \cdot |M_{\nu\tau}|^2 \delta(E_\nu - E_\tau), \quad (4.9)$$

where $f(E) = \left(\exp\left(\frac{E}{k_B T}\right) + 1\right)^{-1}$ is the Fermi-Dirac function (describing probability of occupation of the total probe and sample electronic states at temperature T and energy E), k_B is Boltzmann constant, E_ν (E_τ) is the energy of state ψ_ν^s (ψ_τ^p) in the absence of tunneling, $M_{\nu\tau}$ is the tunneling matrix element between the unperturbed electronic states of the sample ψ_ν^s and probe ψ_τ^p , and the $\delta(E_\nu - E_\tau)$ is a factor of the energy conservation in case of elastic tunneling. The tunneling matrix has to be calculated to find the tunneling current value. It is described by Bardeen as [80]:

$$M_{\nu\tau} = -\frac{\hbar}{2m_e} \int_{\Gamma} (\psi_\tau^{p*} \nabla \psi_\nu^s - \psi_\nu^s \nabla \psi_\tau^{p*}) d\Gamma. \quad (4.10)$$

The expression in parentheses corresponds to the tunneling current density, and it is integrated over the whole separation surface Γ lying entirely within the vacuum (barrier) region separating the sample and probe. To calculate the tunneling current operator, the exact wave functions ψ_ν^s and ψ_τ^p are required. As the atomic structure of a probe remains unknown, the model of probe wave function ψ_τ^p is crucial.

Tersoff-Hamann model

In 1983 Jerry Tersoff and Donald R. Hamann utilized Bardeen's theory to describe STM [81, 82]. They considered STM as two separated 3D electrodes: the sample, defined as a superposition of periodic plane waves, and the probe, modeled as a locally spherical s-wave function. At low U (~ 10 meV) and low temperatures, Bardeen's equation describing tunneling current (Eq. 4.9) takes the form [81]:

$$I_t = \frac{2\pi e^2}{\hbar} U \sum_{\nu, \tau} |M_{\nu\tau}|^2 \delta(E_\nu - E_F) \delta(E_\tau - E_F). \quad (4.11)$$

It follows from the above, that the I_t depends on the probe's DOS and the sample's local density of states (LDOS) at the center of the effective probe's curvature at the quasi-Fermi energy of the sample. Quasi-Fermi energy refers to the energy at which the sample has occupied states after the electronic states shift that results from the application of U . Tersoff-Hamann approximation allows for the understanding that STM topography images do not solely reflect the sample topography, but rather a combination of the topography with the contour plot of sample's LDOS and the probe's DOS at the Fermi energy level. Although the Tersoff-Hamann model provides a basic understanding of STM images, it has limitations. For instance, most probes are made from tungsten, platinum-iridium alloy, or other transition metals hence d-orbitals dominate instead of s-orbitals as assumed. C. Julian Chen derived further systematic approximations of probe wave functions analyzing contributions of various p- and d-orbitals of the probe and calculating corresponding tunneling matrix elements [83]. Additionally, the Tersoff-Hamann model also neglects the interactions between the probe and the sample which may affect the sample wave function and further the STM topography. As assumed before, it is applied for low temperature and low bias only. To extend this approach to the finite bias voltage range and different probe shapes, the signal has to be integrated over the LDOS of the sample ρ_s and the probe ρ_p , and transmission coefficient T_{TH} in the range from E_F to $E_F + eU$ [84]:

$$I_t \propto \int_{E_F}^{E_F + eU} \rho_s(E) \rho_p(E - eU) T_{TH}(E, eU, z) dE. \quad (4.12)$$

T_{TH} describes the voltage drop-off in the barrier region and depends, for example, on ϕ_s and ϕ_p , and describes the contribution of particular electronic states to I_t .

4.1.2 Surface imaging

One of the most basic operating modes in STM is sample surface imaging, also known as topography imaging. It is important to note that in STM, the term *topography* refers to a combination of the sample surface topography and LDOS of the probe and sample. The resulting STM images vary depending on the applied U . Surface imaging serves as a basis for statistical analysis

or further experiments such as point tunneling spectroscopy or atoms and molecules manipulation. There are two operating modes: constant height mode and constant current mode.

Constant height mode

A schematic illustration of the constant height mode (CHM) is shown in Figure 4.4 a). As the name suggests, the probe's position is kept at a constant height while the modulation of I_t is recorded. The changes of I_t signal are directly digitized as a function of the lateral position of the probe relative to the sample surface, represented by U_x and U_y voltages. Using CHM, images are presented as a matrix $I_t(x, y)$, with I_t presented as a function of the probe's position x and y . Direct registration of I_t enables the utilization of the full sensitivity of the exponential relation between barrier height and I_t . The greatest advantage of the CHM mode is that vertical height information is directly available by extracting the value from the registered I_t signal as changes of local tunneling barrier height. Direct registration of the signal also allows for high scanning speeds. In this mode where no signal correction is needed, the maximum scanning rate is limited only by the lowest mechanical resonance frequency of the STM unit, preamplifier bandwidth, and analog-to-digital converters in control electronics. Therefore CHM is suitable for registering atomic-scale on-surface dynamic processes such as surface diffusion. However, the main drawback of CHM is that it is only suitable for imaging atomically flat surface regions and requires high thermal stability of the probe-sample system. The inability to control the tunneling signal increases the risk of crashing the probe if the above assumptions are not met [73, 79]. In practice, CHM is usually used to zoom in on a surface that was visualized before by means of imaging mode using a feedback loop.

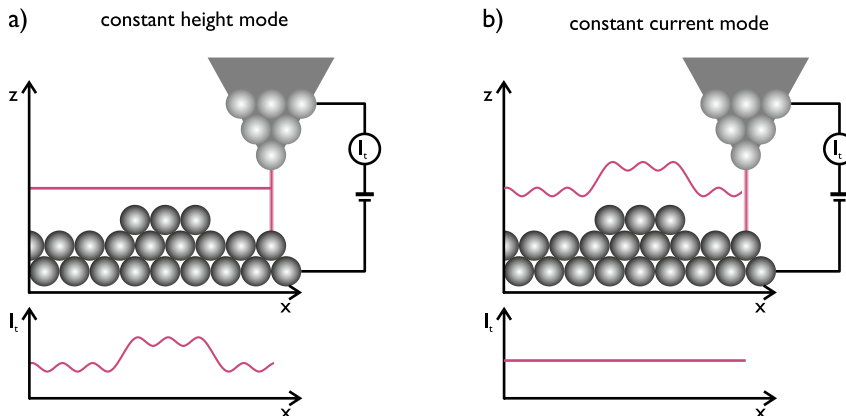


Figure 4.4: STM imaging operating modes – a) constant height mode – z position is fixed and changes in the tunneling current are registered, b) constant current mode – I_t is kept constant by the feedback loop and the voltage signal from the z electrode is recorded.

Constant current mode

The constant current mode (CCM) is the most commonly used operating mode of the STM. In this mode, the probe scans the surface while its vertical position is adjusted by the feedback loop to maintain a constant value of I_t (as shown in Figure 4.4 b)). The I_t signal after I/V conversion, amplification, and linearization, is fed to the PI controller where it is compared to the I_{sp} value set by the user (as seen in Figure 4.1). The resulting error signal is used to adjust the probe's vertical position by multiplying it using proportional gain (P-part of the feedback loop) and then integrating it (I-part of the feedback loop) using a characteristic time constant value. The P- and I-modified signals are then summed up and amplified by a high-voltage amplifier before being fed directly to the z electrode of the piezoscanner. This causes the probe's height adjustment through the contraction/extension of the piezoscanner, thereby maintaining a constant value of I_t . The output signal from the feedback loop, U_z , is recorded as a function of voltages representing the lateral position of the probe relative to the sample surface. These signals are then translated into the matrix $z(x, y)$ and serve to reproduce the STM image. It is important to optimize the feedback loop parameters before each experiment since the operation of the feedback loop depends on various factors such as probe characteristics, preamplifier gain, or high voltage gain [73]. Although maintaining a constant value of I_t allows for the investigation of samples with different corrugations, it also increases the scanning time due to the additional reaction time needed for the feedback loop to compensate the signal [79].

4.1.3 Differential conductance measurements

Apart from imaging modes, various spectroscopic modes such as $I_t(U)$, $I_t(z)$, $z(U)$ or derivatives like $\frac{dI_t}{dU}$, $\frac{dI_t}{dz}$, $\frac{dz}{dU}$ have been developed over the years. The tunneling process between the sample and probe depends on three parameters: I_t , U , z . The spectroscopic modes can be used to identify the relations between these parameters by fixing one of them and registering the dependence between the other two. These signals can be measured at fixed lateral probe position, along the specified line, or at various probe lateral positions (x, y) . The lock-in technique is claimed to provide better results than the conventional $I_t(U)$ signal registration method [79]. The Lock-in technique allows not only to reduce the signal-to-noise ratio significantly but also to record the derivative signal directly from lock-in without the need for further mathematical analysis, as in the case of the conventional method. This technique was used in all presented measurements and will be described in more detail below.

Lock-in amplifier

Lock-in amplifiers are commonly used to filter frequency and phase incoherent signals in order to extract specific signals from a noisy environment [85]. In the STM context, the lock-in technique is used not only to reduce noise

but also because it allows for the use of nonlinear current-voltage dependence and selective measurement at the fundamental frequency or any of its harmonics. The modulated bias voltage induces oscillation of the tunneling current with the frequency of the modulation signal and an amplitude proportional to the derivative of the tunneling current with respect to the bias voltage dI_t/dU . Figure 4.5 shows the adaptation of lock-in to the STM setup. To generate the sinusoidal modulation signal $U_{\text{mod}} \cdot \cos(\omega_{\text{mod}}t)$, which

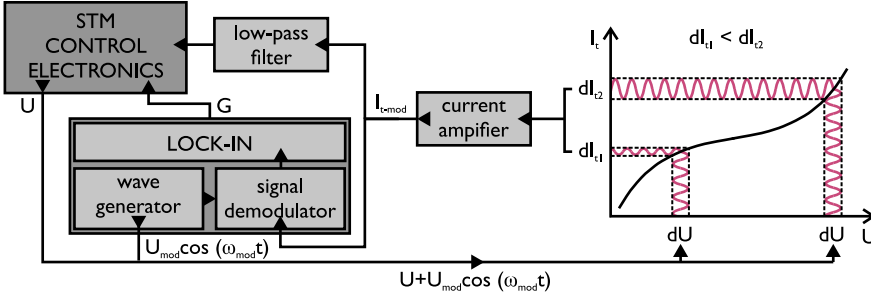


Figure 4.5: Differential conductance measurements – lock-in adaptation to the STM setup.

typically has a high frequency ω_{mod} of the order of kHz and small amplitude U_{mod} of mV-order, an internal or external wave generator is used. The value of ω_{mod} is determined by the preamplifier bandwidth and is usually set to the highest possible prime number. The higher the frequency, the shorter the integration time of the modulated signal can be, which is especially important for differential tunneling conductance mapping, which is time-consuming. The modulation parameter U_{mod} can be adjusted to control energy resolution and signal intensity. The lower the value of U_{mod} , the higher the energy resolution is, but also the signal intensity decreases. U , generated by STM electronics, and reference signal are added together and further applied to the tunneling probe-sample junction. Hereby the tunneling current is affected by the reference modulation. The modulated tunneling current $I_{t-\text{mod}}$ can be expressed using Taylor expansion [85]:

$$\begin{aligned}
 I_{t-\text{mod}}(U + U_{\text{mod}}\cos(\omega_{\text{mod}}t)) = \\
 I_t + \frac{dI_t(U)}{dU}U_{\text{mod}}\cos(\omega_{\text{mod}}t) + \frac{dI_t^2(U)}{dU^2}U_{\text{mod}}^2\cos(\omega_{\text{mod}}t)^2 + \dots,
 \end{aligned}
 \tag{4.13}$$

where I_t is the tunneling current without applied modulation. By choosing the n -th harmonic, it is possible to filter the tunneling current n -th order derivative. After I/V conversion and amplification, the modulated tunneling current signal is split into two paths. The first is fed through a low-pass filter to the STM electronics as a I_t signal. The second goes to the lock-in, where it is integrated over a time longer than a period of the modulating function. It is then demodulated by comparison of registered I_t signal with reference modulation signal and extracted as a differential tunneling conductance $G = dI_t/dU$, which is fed to the STM electronics. The lock-in allows to extraction

of signals in a specific frequency range around the ω_{mod} , efficiently rejecting all other frequency components. The lock-in technique was used for point and line tunneling spectroscopies at constant height, differential tunneling conductance mapping, and field emission spectroscopy.

Tunneling spectroscopies at constant height

The most common STM spectroscopic mode is registering dI_t variation as a function of dU . Figure 4.6 summarizes various operating modes of STM for the fixed vertical position of the probe. The simplest approach, shown in Figure 4.6 with blue color, is the differential conductance (dI_t/dU) spectroscopy, also known as point tunneling spectroscopy (PTS). The lateral probe position is fixed and the dI_t/dU signal is recorded. Measurements of dI_t/dU curves can be extended to multiple spectra records registered along the defined line (line tunneling spectroscopy (LTS) – Figure 4.6 indicated with gray color) or even every pixel of the image (current imaging tunneling spectroscopy (CITS)). The probe's position for spectroscopic measurements is defined using previously made overview topography. The user defines the point, line, or area for spectra records, respectively for PTS, LTS, and CITS. Then, the probe is positioned at the desired height by determining the stabilization bias U_{stab} and tunneling current I_{stab} . The feedback loop is turned off, and while the U signal is ramped within the given energy range, the I_t and dI_t/dU are registered. By calculating the derivative from the Eq. 4.12 it is possible to explain how to interpret obtained differential tunneling conductance results [86].

$$\begin{aligned} \frac{dI_t}{dU} &\propto \rho_s(E_F + eU)\rho_p(E_F)T(E_F + eU, eU, z) \\ &+ \int_{E_F}^{E_F + eU} \rho_s(E)\rho_p(E - eU) \frac{dT(E, eU, z)}{dU} dE \\ &+ \int_{E_F}^{E_F + eU} \rho_s(E) \frac{d\rho_p(E')}{dE'} T(E, eU, z) dE. \end{aligned} \quad (4.14)$$

Assuming the ρ_p and T constant in the considered energy range, the two integrals in Eq. 4.14 vanish and the expression simplifies to:

$$\frac{dI_t}{dU} \propto \rho_s(E_F + eU)\rho_p(E_F)T(E_F + eU, eU, z). \quad (4.15)$$

In general, the dI_t/dU measurements are a good approximation to the sample's LDOS at an energy value given by eU [79, 86].

Differential tunneling conductance mapping

Another spectroscopic mode is differential tunneling conductance mapping, also known as dI_t/dU mapping, shown in Figure 4.6 with yellow color. By combining the high lateral resolution of the STM imaging mode with the high energy resolution of the spectroscopic mode, the spatial distribution of the sample's LDOS can be resolved. dI_t/dU signal is recorded at all (x, y)

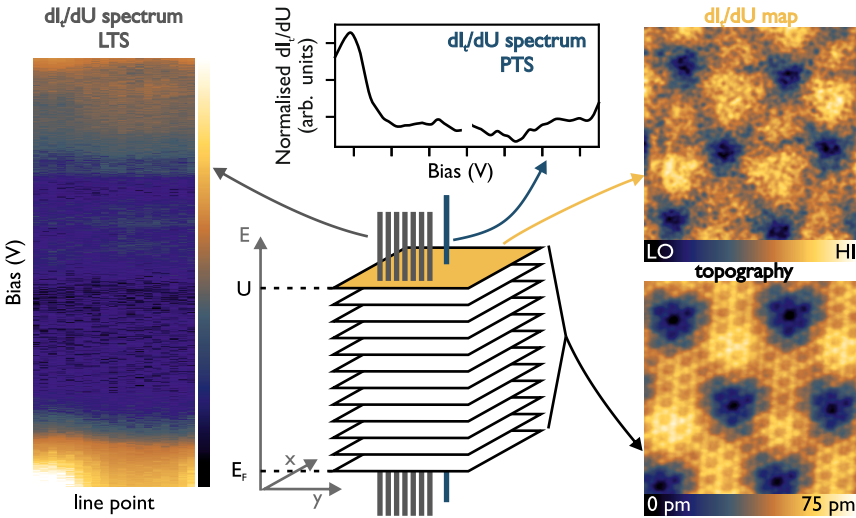


Figure 4.6: STM spectroscopic modes – top-central panel (blue) – the differential conductance spectroscopy at fixed point (PTS); left panel (gray) – the differential conductance spectroscopy along the line (LTS); top-right panel (yellow) – differential conductance mapping; bottom-right panel (black) – topography mode.

points of topography matrix, at specific energy value eU . Registration of dI_t/dU maps simultaneously with the topography (that shows the integration of electronic states from E_F to the energy given by U) allows for direct correlation of topographic and spectroscopic features of the sample (compare in Figure 4.6). dI_t/dU maps can be recorded while both topography modes CHM and CCM are involved. Within this mode, the use of the lock-in technique is crucial to ensure the energy selectivity of the recorded dI_t/dU signal. Since in CCM, the feedback loop is active over the measurement it may cause some artifacts, that can be reduced by averaging the forward and backward registered dI_t/dU maps.

Field emission spectroscopy

Tunneling of the electrons, described in Subsection 4.1.1, is not the only way to transfer electrons between electrodes. Already in 1897, Robert W. Wood observed that when a strong electric field is applied to a cold metal surface, electrons may be emitted from it [87]. In 1928 Ralph Fowler and Lothar Nordheim explained this phenomenon known as field emission or Fowler-Nordheim tunneling, by describing the transmission of electrons through the surface potential barrier at the metal–vacuum interface using quantum-mechanical tunneling [88].

In field emission mode, STM operates with a U value that exceeds the local tunneling barrier height. Starting from the probe–vacuum interface, there is a potential barrier at the surface, that keeps electrons within the probe. This barrier is called the image potential barrier, and its height is

known as the work function ϕ . The simplest model has a Coulomb-like trend, and with increasing distance from the surface of the probe z , it approaches exponentially to the energy level E_{vac} as depicted with a dashed line in Figure 4.7 [89]. When a high negative electric field is applied, the potential barrier is modified, resulting in a triangular barrier of finite thickness with height reduced by a factor $\Delta\phi$. The effect of reduction of the image potential barrier caused by the electric field is called the Schottky effect [90].

When considering the other side of the tunneling junction, electrons emitted from the probe's surface, after tunneling through the reduced potential barrier, are accelerated towards the surface by an electric field. Between the image potential and the sample's surface, electrons are described as traveling waves. Electrons are partially reflected from the sample's surface and travel back toward the probe, where they are reflected again at the z_x point of image potential. In other words, the electrons are trapped in the potential well. Depending on the width and height of the well, numerous reflections of electrons may result in constructive and destructive interference. For certain energies, resonance conditions are met, and standing waves are formed. These discrete energetic states are called field emission resonance (FER) states [91, 92], and they are associated with the image-potential states (IPSs). IPSs are formed as a Rydberg-like series of bound quantum states arising in a one-dimensional potential well, similar to the electrons in hydrogen atoms.

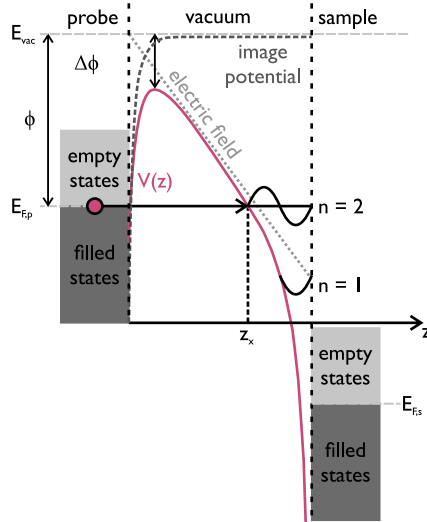


Figure 4.7: Field emission spectroscopy – a scheme of influence of negative electric field (gray dotted line) on the image potential (gray dashed line). Modified image potential, reduced by a $\Delta\phi$ factor is marked with a color line. Figure reproduced from [89].

In experiments, the z/U step-like characteristic and dI_t/dU signal are registered in a CCM by positioning the probe at a measurement point and ramping U in the range above ϕ , which is typically from 3 to 10 V

in this dissertation. The step-like shape of z/U characteristic, and oscillations observed in dI_t/dU signal are the experimental fingerprints of FER states. The oscillations observed in the derivative signal are also known as Gundlach oscillations, named after Karl Heinz Gundlach, who calculated the transmission coefficient for a trapezoidal potential barrier as a function of applied voltage in 1966 [93].

Normalization

As follows from the Eq. 4.14, the spectroscopic signals not only contain information about ρ_s but also information about the T and ρ_p , especially for high U values. ρ_p and T , that increases monotonically with U , are superimposed on spectroscopic information forming background signal. These effects can suppress relevant features of ρ_s , therefore it is common to normalize spectroscopic data. The most widely used normalization procedure, proposed by Randall M. Feenstra in 1987, is to divide dI_t/dU by the total conductance of the tunneling junction I_t/U [94, 95].

$$g = \frac{dI_t/dU}{I_t/U} [1]. \quad (4.16)$$

The normalized signal is a dimensionless quantity. This procedure may cause an artifact around 0 V since the I_t value crosses zero, but it can be removed by setting the normalized dI_t/dU signal to unity at U equal 0 V.

4.2 Low-energy electron diffraction

Low-energy electron diffraction LEED is a powerful method widely used in materials science research for investigating real-time surface structure in reciprocal lattice. The concept of LEED was developed based on diffraction methods used to study the crystal structure of bulk materials. This technique uses the diffraction of low-energy electrons from the surface of the sample being studied. The diffraction of electrons by crystalline surfaces was first demonstrated by Clinton Davisson and Lester H. Germer in 1927 while working at Bell Telephone Laboratories [96]. They investigated angle-dependent electron scattering from the polycrystalline nickel sample. During their experiment, they accidentally oxidized the surface of the sample. To remove the oxidation layer they annealed the sample high enough to form a nearly monocrystalline sample. In consequence, after thermal treatment, they observed sharp diffraction peaks at certain angles which they later assigned as interference patterns of electrons scattered from the surface. Davisson and Germer were awarded in Nobel Prize in 1938 for their experiment [97]. Their discovery is even more important because it was the first experimental confirmation of Louis de Broglie's hypothesis about the wave nature of electrons [98]. In the early 1960s, advances in electronics and UHV technology made it possible to implement the electron scattering phenomenon in an experimental technique named low-energy electron diffraction. Figure 4.8 shows the typical experimental setup of the LEED

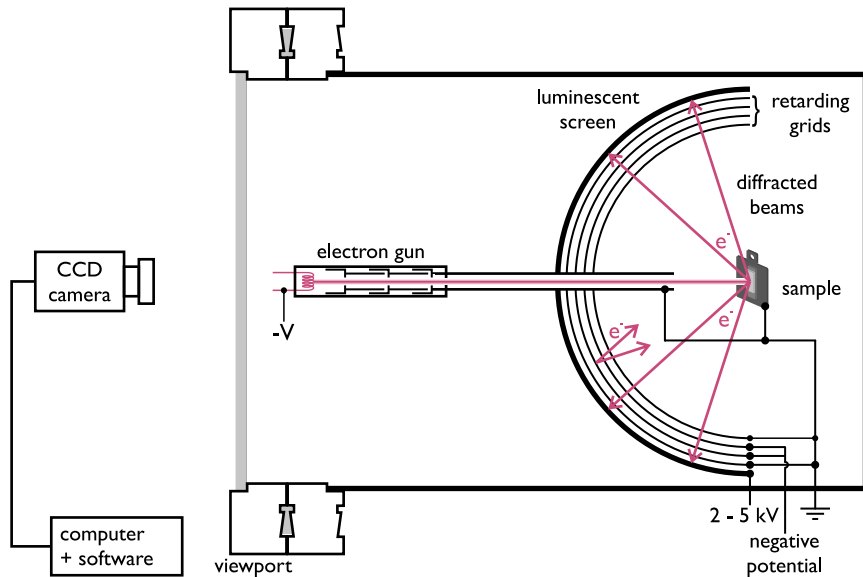


Figure 4.8: Low-energy electron diffractometer – scheme of the experimental realization of a spectrometer for LEED and AES experiments.

technique. The sample is centered perpendicular to the electron beam and LEED optics. An electron gun consisting of heated filament and focusing lenses emits a narrow monoenergetic beam of electrons with energy E_{beam} in the range from 0 – 500 eV [99]. Electrons are accelerated toward the grounded sample by applying a negative voltage, equal to the desired electron beam energy, to the filament. Electrons may interact with the sample in three ways: they can be reflected, diffracted, or collected by the sample. The second way is used in the LEED technique. After a collision with the sample's surface, electrons diffract in numerous directions depending on the surface structure. Diffracted electrons returning to the LEED optics first pass through the zero-field region and then pass through a set of retarding grids. The first one, known as the shielding grid, is grounded and it shields the second grid, which has a negative potential. The second and the third grids, called suppressor, serves as a filter to repel electrons with energy lower than the incident electron beam energy. Electrons with lower energy are the result of inelastic diffraction and they would increase the background noise. The fourth grid is grounded and shields the luminescent screen which carries positive high voltage. Electrons that pass through the grids are accelerated into the phosphorous screen by the positive high voltage in range 2 – 5 keV applied to the screen [100]. Incident electrons induce a phosphor glow on a luminescent screen with spatial distribution and intensity depending on the surface structure and incident electron energy. Additionally, LEED optics are covered with a protecting shield made from material with very high permeability. It is used to avoid the influence of stray magnetic fields on the electrons' paths. The obtained LEED pattern is called the Fraunhofer

diffraction pattern which is the Fourier transform of the surface atom arrangement [101]. LEED patterns are recorded through the viewport opposite the luminescent screen. In the past, they were recorded manually using photos or videos, but later, computer-controlled CCD cameras were used for automatic acquisition.

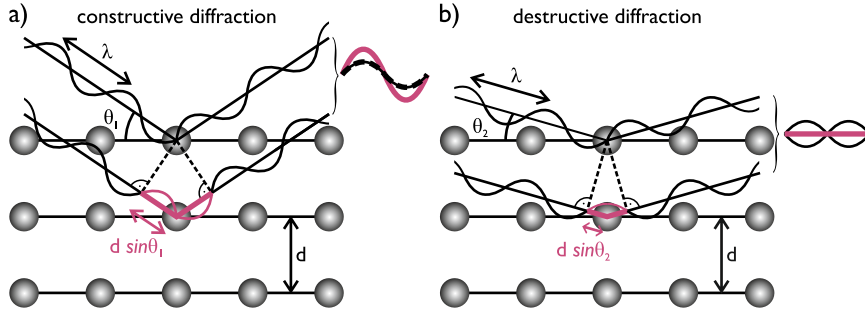


Figure 4.9: Bragg diffraction – scheme of two possible diffraction scenarios: a) constructive diffraction – condition for constructive interference is fulfilled, b) destructive diffraction.

De Broglie's hypothesis of wave-particle duality suggests that every material object can be described in two ways: as a set of particles or as a wave. In the context of LEED, the wavelength of electrons λ can be expressed as:

$$\lambda = \frac{h}{\sqrt{2m_e e U_A}}, \quad (4.17)$$

where h is a Planck's constant and U_A is the acceleration voltage. To observe the diffraction effect of electrons on the atomic structure of the surface, the wavelength of electrons needs to be comparable to the interatomic distances of the sample. This is true for energies commonly used in LEED, ranging between 0 – 500 eV. Similar to x-ray, electron diffraction follows the Bragg's law [102]. Considering the sample as a set of parallel planes with interatomic distance d the condition for constructive interference is [99]:

$$n\lambda = 2d \sin \theta, \quad (4.18)$$

where n is a diffraction order (integer) and θ is the angle between the incident wave and the sample's surface. This condition can be derived from Figure 4.9. Incident electron wave is diffracting on every atom of each plane. A wave diffracted on a single atom is spherical, but for atoms within the same plane the fronts of these spherical waves form the front of a plane wave and thus the considerations can be limited to the diffraction on the planes only. The diffracted waves will constructively interfere when the path difference between adjacent waves is equal to an integer multiple of the wavelength. Initially, LEED was used for qualitative studies of surface periodicity to understand the size of the surface unit cell and surface symmetries. However, with the development of computational techniques, it is now widely used for quantitative investigations. By recording numerous LEED patterns for

various energies, it is possible to extract I-V curves that plot the dependence of the Bragg's spot intensity as a function of the energy of the incident electron beam. These curves are used in iterative computational procedures to determine the geometrical structure of surface atoms. Based on geometry from the LEED patterns, initial atoms arrangement is proposed. Further, using computational methods, theoretical I-V curves are calculated and compared with experimental results. If the results are not matched well within the level of compliance assumed by the user, the model is adjusted and the process is iteratively repeated until the theoretical and experimental results give satisfactory agreements [101].

4.3 Auger electron spectroscopy

Auger electron spectroscopy (AES) is a non-destructive and surface-sensitive technique, that determines the chemical composition of surfaces using the energy of emitted electrons. AES is a form of electron spectroscopy and it is based on analysis of the energy distribution of Auger electrons. Auger effect (sometimes called Auger-Meitner effect) was discovered in the 1920s independently by Lise Meitner [103] and Pierre Auger [104]. They found that if a core electron is removed from the atom, a secondary electron may be released. This emission process is shown in Figure 4.10. The primary beam

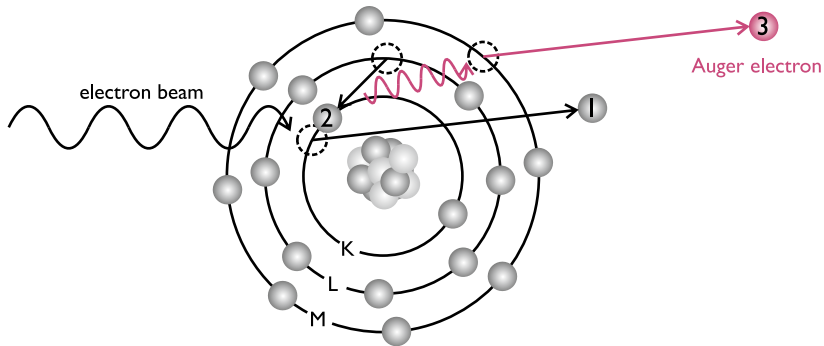


Figure 4.10: Auger electron spectroscopy – scheme of Auger electron emission process. The electron beam causes the emission of a primary electron (1), resulting hole is filled by an electron from a higher shell (2), which at the same time emits excess energy (marked with the color wave) causing the emission of Auger electron (3).

of electrons, typically with the energy of 3 – 20 keV [105], collides with an atom, causing a core electron (1) to be ejected from the inner electron shell, leaving a vacancy. This vacancy is then filled by an electron from a higher energy level (2), releasing excess energy. Mostly, that energy is ejected as an x-ray emission, but sometimes the competing process may occur. Energy is then transferred to another electron, and if it is higher than its binding energy, the electron (3) is released from the atom. This secondary electron is known as an Auger electron. The kinetic energy E_{Auger} of the Auger electron, written in terms of electrons binding energies referenced to the

Fermi level, describes the relation [99, 100]:

$$E_{\text{Auger}} = E_1 - E_2 - E_3 - U_{\text{HH}}, \quad (4.19)$$

where E_1 is the binding energy of the core electron (initially ejected from an atom), E_2 is the binding energy of the electron filling the vacancy, E_3 is the binding energy of Auger electron, U_{HH} is a hole-hole repulsion energy. Auger electron energy depends on the energy of atomic levels, rather than the energy of the primary electron beam. Binding energies E_1 , E_2 , E_3 are known, and they are specific for elements, while U_{HH} is an extra energy resulting from the screened Coulomb interaction of the final state vacancies and relaxation of the other surrounding electrons. It is on the order of 0 – 10 eV and usually, it is neglected, since it does not affect the element identification process. Overall, element identification using AES is based on the measurement of Auger electrons' kinetic energy E_{Auger} . In general, it is not necessary to analyze in detail the entire process of Auger electron emission to identify the element. The major Auger electron energies are tabulated and presented in the form of graphs in reference handbooks [106, 107].

AES experimental setup requires several basic components. These include an electron gun with focusing lenses to form an electron beam, an electron energy analyzer to collect and analyze the distribution of Auger electrons, and a computer to support the experiment. The two most commonly used types of analyzers are concentric hemispherical and cylindrical mirror analyzers [99]. Four grid LEED analyzer can also be used as an analyzer for AES (Figure 4.8). It gives lower efficiency than previously mentioned analyzers, but it is convenient to combine with LEED within a single setup if both surface structure and chemical composition need to be investigated. This type of setup was used within the dissertation, therefore, on the basis of its construction, the operating principle of the AES will be described. AES electronics consists of three main elements: a sweep generator that supplies retarding grids with potential, a signal generator to modulate the voltage, and a lock-in amplifier for signal detection. Additionally, effective improvement of the gathered signal is achieved using a preamplifier combined with the collector to enhance the registered signal [108]. Auger spectra can be registered in two forms: direct and derivative. The direct spectrum $N(E_{\text{Auger}})$ presents the total electron signal registered as a function of Auger electrons' kinetic energy. Auger electron peaks are rather low intensity and in this case, that signal is superimposed on a large, slowly varying background signal. The background is the result of the emission of secondary and backscattered electrons as a side effect of the interaction between the electron beam and sample. There may be observed a strong peak from elastically backscattered primary electrons with the energy of incident beam energy. Discrete peaks on the low energy side of elastic peak arise due to electrons that have lost the energy due to interaction with plasmons. The broad peak at energies below 50 eV is due to secondary electrons that collide many times inelastically. A Lock-in amplifier is used to detect the modulated signal as a derivative of $N(E_{\text{Auger}})$. This method increases the signal-to-noise ratio and suppresses

the effect of background noise. Thus another form of AES spectra is the presentation of derivative $dN(E_{\text{Auger}})/dE_{\text{Auger}}$. The AES peaks are then more pronounced, and it is more convenient to use the derivative form for qualitative analysis [105]. To identify elements accurately, not only the AES peaks' energy positions are important but also their shape and relative intensity. Special care must be taken when analyzing two elements whose AES signals are overlapping. Signals can be compared using handbooks or using computer identification software that allows rapid peak identification. AES can also be used for quantitative analysis to identify the chemical composition of the surface. Once the identification of the elements is done, the intensities of element signals are compared to calculate relative concentrations [105, 108]. The AES technique has also some limitations. Auger electron emission is a three-electron process, thus hydrogen and helium are not detectable.

4.4 X-ray spectroscopy techniques

In 1895, Wilhelm Röntgen discovered the existence of electromagnetic radiation known as x-rays [109], which have higher energy than ultraviolet (UV). This discovery led to the development of research techniques using x-rays, which are classified as either soft (0.1 – 3 keV) or hard (above 3 keV) depending on their energy [110]. X-rays have a wavelength comparable to interatomic distances in solids, allowing for atomic resolution studies of material inner structures. Various techniques have been developed over the years using x-ray radiation, especially using modern, 3-rd generation, synchrotron facilities. The following Subsection will focus on the x-ray absorption spectroscopy and x-ray magnetic circular dichroism methods.

4.4.1 X-ray absorption spectroscopy

X-ray absorption spectroscopy XAS is essential to understanding the XMCD method. Absorption edges were first observed by Maurice de Broglie in 1913, who registered K absorption edges of Br and Ag contained in the photographic emulsion [111]. Further analysis was necessary to correctly interpret these results, but it is recognized as the first step toward the development of the XAS technique.

X-rays can interact with matter in several ways. It can be partially or completely absorbed, elastically (Rayleigh) or inelastically (Compton) scattered or it may cause the emission of photons or electrons with characteristic energy [112]. The absorption process dominates for x-rays below 20 keV [112], for which at the same time the scattering processes are negligible. In general, absorption intensity decreases with the increasing incident beam energy, however, for certain energy values, there are exceptions. This is due to additional absorption channels that arise when the energy of the incident radiation corresponds to the binding energy of a core level [112]. Therefore, in the absorption spectrum sharp discontinuities appear, which are called absorption edges. The edges are labeled using so-called x-ray notation that refers to the state of the core electron excited by incident x-ray

radiation, as shown in Figure 4.11. The x-ray notation scheme involves using letters K, L, M, and so on, which denote the principal quantum number, while the subscript indicates the spin-orbit split subshell from which the core electron is excited. Within this dissertation, the focus is on $M_{4,5}$ edges of REM, which describe $3d^{10}4f^n \rightarrow 3d^9 4f^{n+1}$ resonant transition, *via* excitation of the $3d_{3/2}$ and $3d_{5/2}$ core electrons, respectively. The energy of core level electrons is element-specific, which gives XAS its chemical selectivity. The values of core level energies are tabulated and can be found in x-ray handbooks [113] and the Center for X-Ray Optics website [114].

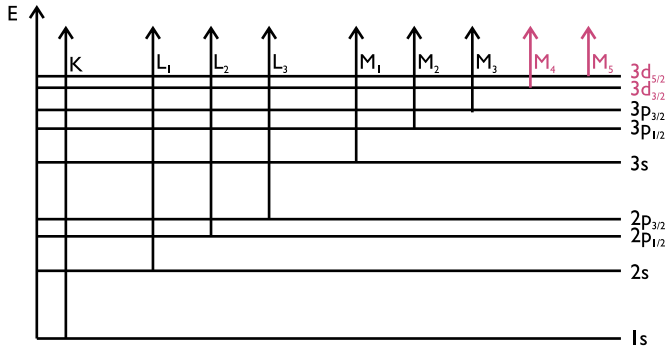


Figure 4.11: X-ray notation scheme – M_4 and M_5 edges correspond to the excitation of $3d_{3/2}$ and $3d_{5/2}$ core electrons – the point of interest for REM investigation.

When a photon is absorbed, a core level electron is excited to an empty state above the Fermi level, creating a core hole. The lifetime of the core hole is very short, lasting only 10^{-15} seconds [110] before it decays. The two main decay paths are fluorescence or Auger electron emission [110]. The mechanism of the latter was already explained in Subsection 4.3 in terms of electron beam interaction with matter. In the fluorescence process, the core hole is filled with another electron that possesses higher energy than the core hole. The energy difference between the core hole and shallow electron is then emitted as electromagnetic radiation in the fluorescence process, usually as x-rays, UV radiation, or visible light. Both, fluorescence and Auger electron emission may lead to the creation of other core holes, which then are filled until all core levels are filled again. The XAS spectrum depicts the dependence of the total linear absorption coefficient $\mu(E^x)$ on the x-rays energy E^x . Therefore, detecting $\mu(E^x)$ is the key element of the XAS method. Figure 4.12 shows various detection modes used in XAS/XMCD techniques. In the simplest case, for samples with known thickness x , $\mu(E^x)$ can be calculated using Lambert-Beer's law [115]:

$$I_{\text{tr}}^x(E^x, x_{\text{eff}}) = I_0^x(E^x) \cdot \exp[-\mu(E^x)x_{\text{eff}}] = I_0^x(E^x) \cdot \exp\left[-\frac{\mu(E^x) \cdot x}{\cos\alpha}\right], \quad (4.20)$$

where $I^x(E^x, x_{\text{eff}})$ is the transmitted beam intensity, $I_0^x(E^x)$ is the incident beam intensity with energy E^x , $x_{\text{eff}} = x/\cos\alpha$ is the effective path length (α

is the beam incident angle with respect to the sample's surface normal).

It is possible to investigate samples of any thickness using XAS by analyzing the decay process of core holes (see Figure 4.12). The decay of the

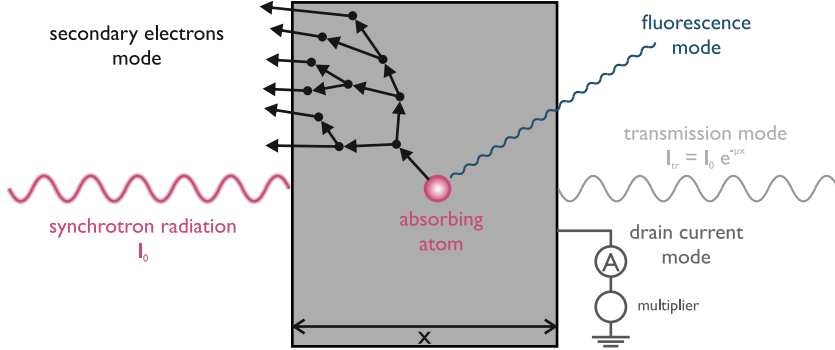


Figure 4.12: X-ray absorption detection modes – a scheme of detection modes used in XAS/XMCD techniques.

core holes results in the emission of electrons, photons, or ions, which can be used to indirectly investigate the intensity of x-rays absorption. This gives rise to various detection modes such as fluorescence and electron yields [110]. Both can be registered as a total yield or as a partial yield, which distinguishes the respective energy of the registered species. Soft x-rays, which were used in the research discussed below, have poor fluorescence yield, while the dominant decay path is the Auger effect. One of the detection modes is an Auger electron yield, which detects the primary emitted Auger electrons. However, the more commonly used detection mode is the total electron yield (TEY), which registers low-energy secondary electrons created after the emission of Auger electrons [115, 116]. Using TEY mode all electrons escaping from the surface of the sample are detected independently on their energy. Despite the fact that the incident soft x-rays penetrate to a depth of several tens of nanometers into the sample, the TEY operating mode allows for investigation only of the near-surface region of the sample. Due to the numerous scattering of the secondary electrons, they have a very short escape depth λ_e . The number of electrons that can be released from the sample decreases exponentially with the distance into the sample [117]. In fact, the probing depth of TEY is about 1 – 10 nm depending on the sample composition [110]. The signal registered by the TEY method may be affected by the self-absorption (saturation) effect, which occurs when the x-ray penetration depth is small compared with the effective λ_e . The angle-dependent TEY signal is expressed using the dependence [112]:

$$I_{\text{TEY}} = \frac{I_0^x(E^x) N_e \mu(E^x) \lambda_e}{\cos \alpha} \cdot \frac{1}{\frac{\mu(E^x) \lambda_e}{\cos \alpha} + 1} = \frac{I_0^x(E^x) N_e \lambda_e}{\lambda_x} \cdot \frac{1}{\frac{\lambda_e}{\lambda_x} + 1}, \quad (4.21)$$

where N_e is the averaged number of secondary electrons escaped from the sample in a cascade caused by a single Auger electron, $\lambda_x = \cos \alpha / \mu(E^x)$

describes x-ray attenuation length. The TEY signal is recorded using a pico amperemeter to detect the small signal and channeltron electron multiplier to amplify the signal [110], or as a drain current flowing from the ground to the sample to compensate for the electron emission current [116].

Absorption of x-rays in the matter is commonly described using an absorption cross-section parameter σ_{abs} , which describes the probability of photon interaction with matter in a specific process. It is defined as a transition probability per unit time W_{fi} to photon flux I_{ph} ratio, and it is proportional to the linear absorption coefficient [112]:

$$\mu \propto \sigma_{\text{abs}} = \frac{W_{\text{fi}}}{I_{\text{ph}}}. \quad (4.22)$$

In order to determine the transition probability W_{fi} the initial ψ_i and final ψ_f states of the absorbing atom (with the energies E_i , and E_f , respectively) are analyzed. Initially, the electron is in a deep core state (atom's ground state), and after the absorption electron is promoted into the previously unoccupied state. The transition probability of the quantum system between two states may be approximated using Fermi's Golden Rule [110]:

$$W_{fi} = \frac{2\pi}{\hbar} |\langle \psi_f | T_o | \psi_i \rangle|^2 \delta(E_f - E_i - \hbar\Omega). \quad (4.23)$$

The delta function provides the energy conservation within the transition and points out that the transition occurs only if the E_f is equal to the sum of E_i and x-ray energy $\hbar\Omega$. $|\langle \psi_f | T_o | \psi_i \rangle|^2$ gives the transition rate, with T_o , as a transition operator that is related to the interaction Hamiltonian H_{int} .

The Lippman-Schwinger equation can be used to describe the T_o using H_{int} by disregarding spin interaction and using Taylor expansion. This allows for obtaining the first-order transition operator T_1 [110], which specifies electric dipole and electric quadrupole transitions. When dealing with x-rays that have energy below 10 keV, it is possible to use the dipole approximation (also called first approximation) by neglecting the electric quadrupole transition term [110]. Including the T_1 operator into Fermi's Golden Rule, it is possible to analyze the allowed transitions of excited core electrons upon the x-ray absorption. However, not every transition is allowed for x-ray absorption, and so-called x-ray absorption selection rules (dipole selection rules) are employed to determine available final states. The matrix element $|\langle \psi_f | T_1 | \psi_i \rangle|^2$ is nonzero if the difference in orbital quantum number l of the initial and final state is equal to 1 and the spin is conserved [110]:

$$\Delta l = \pm 1, \quad (4.24)$$

$$\Delta s = 0. \quad (4.25)$$

Thus the transition $s \rightarrow p$, $p \rightarrow s/d$, and so on are allowed. Selection rules greatly facilitate the analysis by limiting the number of possible transitions. The first approximation limit XAS to the dipole transitions only. The XAS spectrum should reproduce the partial density of states (PDOS) of the $\Delta l =$

± 1 level combined with Lorentzian broadening. The broadening occurs due to the finite lifetime of a core hole, and according to Heisenberg's principle, the uncertainty of its energy. When considering quadrupole transitions, the permitted final states l may differ by 2 or 0 from the initial state [112]:

$$\Delta l = 0, \pm 2, \quad (4.26)$$

therefore the transitions $s \rightarrow d$, $p \rightarrow f$ or $p \rightarrow p$ are allowed. However, they are 100 times weaker than electric dipole transitions and they can be neglected in most cases. It is worth pointing out that despite the weak signal their fingerprints are visible in the XAS spectrum as pre-edge structures in K edges of 3d metals and L edges of REM.

The XAS spectrum can be divided into three regions which are shown in Figure 4.13. Pre-edge peaks arise due to quadrupole-allowed transitions,

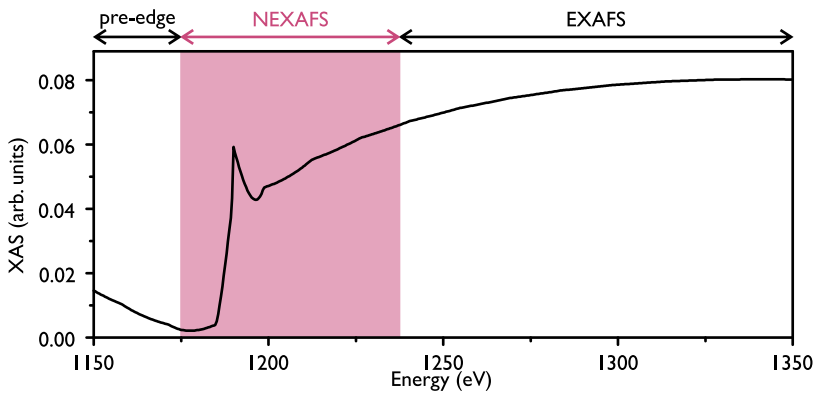


Figure 4.13: X-ray spectroscopy – a scheme of classification of XAS technique depending on energy region with respect to the edge energy E_0 .

forbidden by dipole selection rules ($\Delta l = \pm 2$). A further part of the spectrum covers the area from the adsorption edge E_0 up to 30 – 50 eV above E_0 [112, 118], and corresponds to near edge x-ray absorption fine structure (NEXAFS), alternatively called x-ray absorption near edge structure. The latter is more commonly used to describe solids and inorganic complexes (hard x-ray experiments), while NEXAFS refers to the surfaces (soft x-rays experiments) [118]. Thus I will use NEXAFS to describe this region of the spectrum. The shape of the spectrum reflects the excited state electronic structure around the absorbing atom. Peaks' positions mainly depend on the binding energy of the core electron, but they can also reveal information about the chemical environment of an absorbing atom. For the same element with varying environments, when its oxidation state increases, the peaks are slightly shifted (up to a few eV) toward higher energy. Different edge shapes can be observed due to selection rules of allowed electron transition [112]. The last region, above $E_0 + 50$ eV up to several hundred (or even thousands) eV, is called extended x-ray absorption fine structure [112]. It provides information about the atomic environment and the close neighborhood of the absorbing atom. It is essential to emphasize that the above

description is merely an introduction to the core level techniques and it is based on the single electron approximation. A proper description of strongly correlated electron systems requires considering many-body effects, such as the charge-transfer effect or intra-atomic multiplet coupling effect. A detailed description of these effects can be found in [110, 112, 115].

4.4.2 X-ray magnetic circular dichroism

An important development of the XAS technique came with the prediction of XAS signal dependence on incident radiation polarization. This phenomenon is called dichroism and occurs when the material symmetry is broken due to charge anisotropy (natural dichroism) or anisotropic spin distribution (magnetic dichroism) in the material [112, 119]. Radiation may be linearly or circularly polarised giving rise to the four techniques: x-ray natural linear dichroism, x-ray magnetic linear dichroism, x-ray natural circular dichroism, and x-ray magnetic circular dichroism (XMCD). The XMCD technique is used to investigate magnetic materials and their properties.

The XMCD effect was predicted in 1975 by James L. Erskine and Edward A. Stern. They described theoretical calculations of $M_{4,5}$ edge of Ni [120]. In 1987, Gisele Schütz *et al.* presented for the first time the experimental results of XMCD for K edge of Fe foil [121]. To define the XMCD signal, I will follow the configuration where $\mu_{+(-)}$ indicates XAS for right (left) circularly polarized radiation. In this configuration, the polarization vector of the incident beam (\mathbf{P}) and sample magnetization (\mathbf{M}) are aligned anti-parallel (parallel) (see Figure 4.14) [110, 122]. Instead of $+(-)$, it is

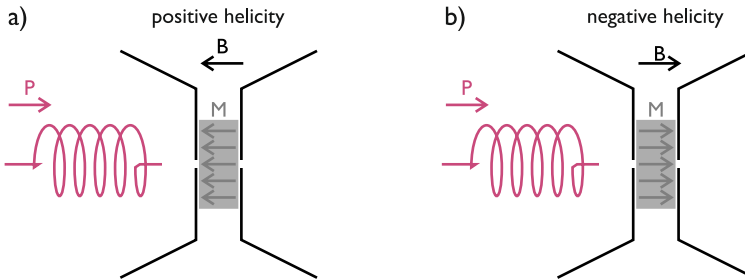


Figure 4.14: X-ray circular polarisation direction definition – a) positive (right) circular polarisation – sample magnetization and wave vector are aligned antiparallel, b) negative (left) circular polarisation – sample magnetization and wave vector are aligned parallel.

also common to use index $R(L)$. The XMCD signal $\Delta\mu$ is calculated as the difference between XAS signal recorded for circularly polarized light with opposite helicity for a magnetized sample [110].

$$\Delta\mu = \mu_{+}(\mathbf{B}) - \mu_{-}(\mathbf{B}) \quad (4.27)$$

The XMCD signal depends on the relative helicity orientation of the photon beam and magnetization direction of the sample. Therefore, the same effect

can be obtained for the change of magnetic field direction, as for the change of beams helicity [110]:

$$\Delta\mu = \mu_-(-\mathbf{B}) - \mu_-(\mathbf{B}) = \mu_+(\mathbf{B}) - \mu_+(-\mathbf{B}) = \mu_-(-\mathbf{B}) - \mu_+(-\mathbf{B}). \quad (4.28)$$

The XMCD process can be described using a two-step model involving a one-electron approximation (schematically depicted in Figure 4.15). The

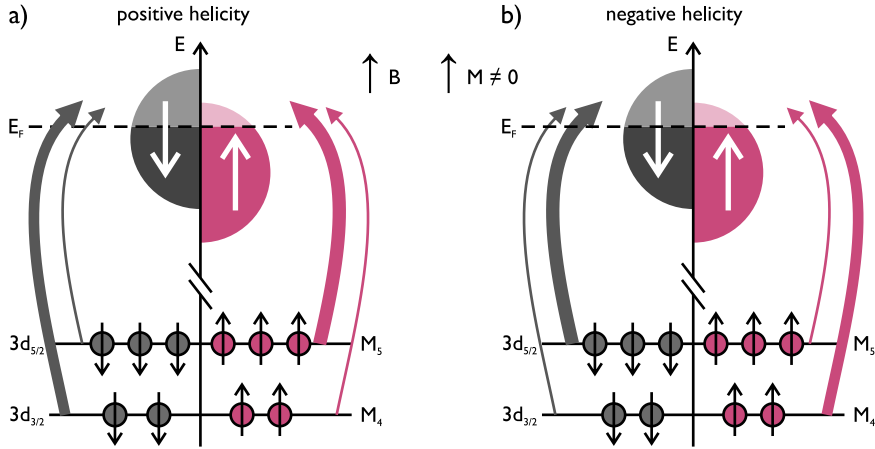


Figure 4.15: Two-step model of XMCD – scheme of XMCD process induced by a) positively circularly polarized x-ray beam, b) negatively circularly polarized x-ray beam. The thickness of the grey and pink arrows indicates the probability of transition.

incoming photon beam's helicity is aligned parallel or antiparallel to the 3d states' orbital moments. The orbital moment of the incoming photon is transferred to the core electron. In respect of selection rules ($\Delta s = 0$), the orbital moment of the incident photon must not influence the spin of the excited electron. The 3d core level is split into $3d_{3/2}$ and $3d_{5/2}$ states due to spin-orbit coupling, where the spin and angular moments are coupled antiparallel and parallel, respectively. As a consequence, the incident beam induces a selective interaction depending on the spin's direction. When the configuration is parallel (antiparallel), the electrons with spin-up (spin-down) are favored to excite [116]. The probability of such core electrons' excitation (disregarding the number of unoccupied final states) may be derived using Clebsch-Gordan coefficients and the transition matrix elements calculation [110, 112]. The total probabilities of a photon with helicity of $\pm\hbar$ to excite a spin up or spin down electron from the $3d_{3/2}$ and $3d_{5/2}$ core levels are summarized in Table 4.1.

In the second step of this process, an excited electron probes the polarization of the unoccupied 4f states. Two cases can be distinguished by considering an incident beam with $+\hbar$ and excitation of the core electron from the $3d_{3/2}$ level into the 4f final states. If the available final states have more holes with the same (opposite) sign as the excited electron then the M_4 edge remains positive (negative). An external magnetic field keeps the

Table 4.1: M_{4,5} transition probabilities – the total probabilities of the excitation of a spin-up or spin-down electron from the 3d_{3/2} and 3d_{5/2} core levels [123].

helicity	3d _{3/2}		3d _{5/2}	
	↑	↓	↑	↓
+ħ	25%	75%	67%	33%
-ħ	75%	25%	33%	67%

states aligned in a non-random direction, so no dichroism can be obtained without an external magnetic field because then the transition probability is independent of the helicity of the incident x-ray beam.

As derived above, the spin polarization of excited core electrons is opposite for M₄ and M₅ edges, while the orbital polarisation remains the same for both edges. Using this fact, it is possible to distinguish between the spin and orbital contributions to a dichroic signal separately using magneto-optical sum rules [116, 124, 125]. In 1992 Theo Thole and coworkers showed that the integral of the XMCD signal over a given absorption edge allows to determine the ground-state expectation value of the orbital angular moment $\langle L_Z \rangle$ [124]. One year later, Paolo Carra and coworkers introduced another formula to use the XMCD signal to calculate the effective spin moment $\langle S_Z \rangle$ [125]. The sum rules are transition-specific, so the equations presented below are in the most general form, and the prefactors related to different transitions (listed in Table 4.2) [115, 126] have to be included:

$$\frac{a}{n_H} \cdot \langle L_Z \rangle = - \frac{\int_{M_4+M_5} [\mu_+(E^x) - \mu_-(E^x)] dE^x}{\int_{M_4+M_5} [\mu_+(E^x) + \mu_-(E^x) + \mu_0(E^x)] dE^x}, \quad (4.29)$$

$$\frac{c \langle S_Z \rangle + d \langle T_Z \rangle}{n_H} = - \frac{\int_{M_5} [\mu_+(E^x) - \mu_-(E^x)] dE^x - b \int_{M_4} [\mu_+(E^x) - \mu_-(E^x)] dE^x}{\int_{M_4+M_5} [\mu_+(E^x) + \mu_-(E^x) + \mu_0(E^x)] dE^x}, \quad (4.30)$$

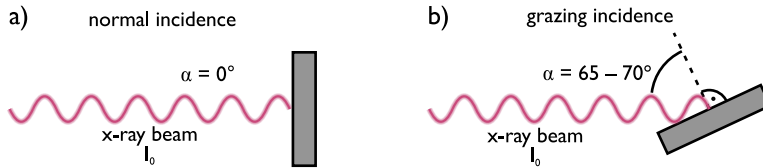
a , b , c , and d are the prefactors dependent on the transition, n_H is the number of holes present in the final state shell, $\langle L_Z \rangle$ and $\langle S_Z \rangle$ are the expectation values of orbital and spin moments projection along the photon beam direction, $\mu_+(E^x)$, $\mu_-(E^x)$, and $\mu_0(E^x)$ are the absorption spectra measured with the photon angular momentum vector aligned parallel, antiparallel, and perpendicular to the magnetic field vector, respectively. Usually, only the first two are measured, while the $\mu_0(E^x)$ is approximated by the averaging of the two circular polarized absorption spectra, thus the denominator reduces to $3/2(\mu_+(E^x) + \mu_-(E^x))$. To calculate the spin moment the value of $\langle T_Z \rangle$ is required. It is the expectation value of the intra-atomic magnetic dipole operator describing possible asphericity of the spin density distribution. In practice, the $\langle T_Z \rangle$ value may be determined experimentally using another technique, approximated based on theoretical calculations, or treated as zero since its value is much smaller than the value of the spin

Table 4.2: Sum rules – prefactors values for various transitions [115].

l_i	l_f	a	b	c	d
s	p	1	–	–	–
p	d	1/2	2	2/3	7/3
d	f	1/3	3/2	2/3	2

moment. Originally, the sum rules were derived in an atomic framework, so certain assumptions were made to apply them to XMCD [112]. These assumptions include neglecting the exchange splitting for the core levels, any energy dependence of the wave functions, and many-body effects. The sum rules also have some limitations, the most important of which is clear energy separation of the edges to calculate the spin moment projection. An indistinct border between the edges would make it impossible to clearly divide the spectrum into two separate edges.

When the photon beam orbital moment direction is aligned parallel (antiparallel) with the magnetization direction, the dichroism effect reaches its maximum (minimum) signal. The value is in between when the alignment is perpendicular. By conducting an angle-dependent analysis of XMCD spectra using sum rules, the microscopic origin of anisotropy can be concluded [110]. If the beam is incident along the normal to the sample surface, it gives out-of-plane contrast. On the other hand, if the beam is incident in a grazing angle, it gives the in-plane contrast (see Figure 4.16). Pure in-plane contrast is impossible to obtain due to the system geometry. It is impossible to set the beam parallel to the sample, therefore the grazing angle is a small angle between the sample surface and the x-ray beam. Practically, the grazing angle must be smaller than the magic angle, which is $\alpha = 65 - 70^\circ$ with respect to the sample's normal. XMCD can also be used for magnetic field-dependent study. Hysteresis loops can help in understanding complex magnetic structures and estimating the contribution of component atomic species to the magnetic properties of the system and their interactions [116].

**Figure 4.16: XAS/XMCD setup configurations** – the concept of normal and grazing configurations of the incidence x-ray beam with respect to the sample.

4.5 Density functional theory

The density functional theory (DFT) is a quantum-mechanical computing method, widely used in physics, chemistry, and materials science. It predicts

the electronic structure of many-body systems such as atoms, molecules, surfaces, and even crystal structures. The DFT is based on two theorems developed by Pierre Hohenberg and Walter Kohn, known as Hohenberg–Kohn theorems [127].

1. *theorem on the equivalence of the electron density and the electronic wave function* – the non-degenerated ground state electron density of the system of interacting electrons $\rho_0(\mathbf{r})$ explicitly describes the external potential in which the electrons move, and hence $\rho_0(\mathbf{r})$ determines all other physical properties of the system including the ground state wave function,
2. *theorem on the existence of an energy functional that minimizes for ρ_0* – there is a certain energy functional depending on the electron density of the system ρ , labeled $E_V^{\text{HK}}[\rho]$, that minimizes only for the ideal ground state electron density ρ_0 .

The DFT describes the system of N interacting electrons using electron density $\rho(\mathbf{r})$ instead of their wave functions $\psi(1, 2, \dots, N)$. The electron density distribution interacting on electron 1 is described by [128]:

$$\rho(\mathbf{r}) = N \sum_{\sigma_1 = -\frac{1}{2}, \frac{1}{2}} \int d\tau_2 d\tau_3 \dots d\tau_N |\psi(\mathbf{r}, \sigma_1, \mathbf{r}_2, \sigma_2, \dots, \mathbf{r}_N, \sigma_N)|^2, \quad (4.31)$$

where ρ is the function of the position vector \mathbf{r} in three-dimensional space. The electron density distribution is obtained by integrating $|\psi|^2$ over the spin (σ) and spatial coordinates (\mathbf{r}) of all N electrons except one (in this case, it is electron 1) and additionally summing over the spin coordinate (σ_1). τ_N denotes here the N -th electron characterized by σ_N and \mathbf{r}_N .

The Hohenberg–Kohn theorem was further developed by Walter Kohn and Lu Jeu Sham, who created a practical implementation of the theorem called Kohn–Sham equations. They proposed a fictitious system (called the Kohn–Sham system) consisting of N electrons that do not interact with each other at all (assuming an electron charge equal to zero). Within this system, instead of the interaction of electrons with nuclei, the electrons are affected by an external potential $\nu_0(\mathbf{r})$. The external potential is estimated so the density ρ is equal to the ground state of the real electron system ρ_0 . Since the electrons do not interact with each other, the system can be reduced to the one-electron problem. The wave functions of these electrons can be easily determined using the Slater determinant, called the Kohn–Sham determinant. Kohn and Sham proposed a general expression for the electronic ground-state energy of such a system [128–130]:

$$E_{\text{gs}} = T_0 + \int \nu_0(\mathbf{r})\rho(\mathbf{r})d\mathbf{r} + J[\rho] + E_{\text{xc}}[\rho], \quad (4.32)$$

where T_0 is the kinetic energy of not interacting electrons, $\int \nu_0(\mathbf{r})\rho(\mathbf{r})d\mathbf{r}$ describes interaction of electrons with the nuclei and $J[\rho]$ is the energy of

Coulomb interaction of ρ with itself. The last term $E_{xc}[\rho]$ is called exchange-interaction energy and describes any other contribution to the energy such as correlation between electrons, their kinetic energy, spin exchange energy, *etc.* The exact form of E_{xc} functional is unknown so only approximations are used within DFT calculations. There are several approximations that allow for calculating the system's properties quite accurately [128, 131, 132]. The simplest approximation is the local density approximation (LDA). Within this approach, the electron density can be treated as locally homogeneous. Thus at any point of the system, the E_{xc} functional is the same and it is determined by [131, 132]:

$$E_{xc}^{\text{LDA}}[\rho] = \int \epsilon_{xc}(\rho)\rho(\mathbf{r}) d^3\mathbf{r}, \quad (4.33)$$

where ϵ_{xc} is the exchange energy per one particle of a spatially homogeneous electron density ρ . LDA is suitable to describe a system with slowly varying spatially electron density. Local spin density approximation LSDA is an extended version of the LDA method and it includes local spin density contribution. However, LDA and LSDA fail when the electron density is not homogeneous and changes rapidly within the electron gas density. Crucial improvement comes with gradient functionals that consider the gradient of the electron density to account for the inhomogeneity of the true electron density. Exchange-energy functional for generalized gradient approximation takes the form [128, 130, 132]:

$$E_{xc}^{\text{GGA}}[\rho] = \int f(\rho_\alpha, \rho_\beta, \nabla\rho_\alpha, \nabla\rho_\beta) d^3\mathbf{r}, \quad (4.34)$$

where ρ_α and ρ_β refers to spin-density.

Chapter 5

Experimental setup

Preparation and characterization of surface alloys require the use of sophisticated instrumentation and suitable conditions. For this purpose, I used ultra-high vacuum (UHV) systems equipped with specialized preparation tools and analytical instruments, which are described in the following Chapter. The initial experiments of preparation and structural and electronic properties characterization were conducted in the group of Prof. Roland Wiesendanger at the Institute of Applied Physics and Interdisciplinary Nanoscience Center Hamburg at the University of Hamburg, using the UHV system described in the Subsection 5.1. As a part of my doctoral studies, I was involved in the modernization of the UHV system at the Institute of Physics at the Poznan University of Technology described in Subsection 5.2. The main goal was to upgrade the system with a home-built multipurpose STM head designed by Ph.D. Eng. Maciej Bazarnik, which is detailed in Subsection 5.2.1. After the modernization, I used this system for further preparation and investigation of structural and electronic properties of REM-Pt surface alloys. To study magnetic properties, I conducted experiments involving the XMCD technique at two synchrotron facilities, as described in Subsections 5.3 and 5.4.

5.1 UHV system with VT STM in Hamburg

The UHV system used in the initial experiments in Hamburg, shown in Figures 5.1 and 5.2, is a custom-made Omicron UHV system and consists of three separate chambers: load lock, preparation, and analysis. The load lock and preparation chambers are independently connected to the pumping system of the turbomolecular pump and diaphragm forepump. The load lock chamber is separated from the preparation chamber with a DN40 CF gate valve. A transfer manipulator connected to the load lock enables to load of up to 4 samples/probes at a time and transfer them to the preparation chamber. Both preparation and analysis chambers are equipped with ion getter and titanium sublimation pumps, thus reaching base pressure

5×10^{-11} mbar. There is a continuous digital registration of the pressure readout from Bayart-Alpert ionization gauges in both chambers. The entire UHV system is mounted on a rigid metal frame placed on a separate foundation to decouple it from low-frequency vibrations of the building. The

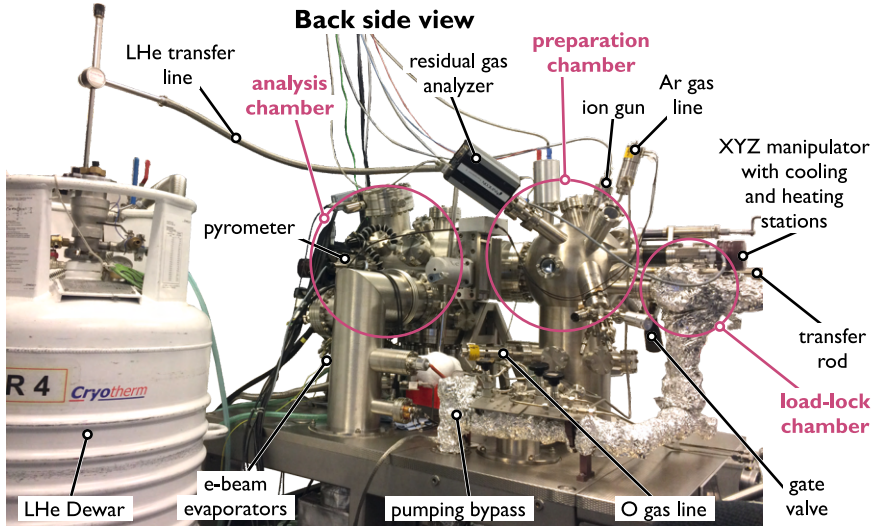


Figure 5.1: UHV system in Hamburg – back view photo of the preparation and analysis chamber. The most important facilities used in this dissertation are marked.

preparation chamber was used for refreshing the probe *via* sputtering and flashing processes, as well as for substrate cleaning between sample preparations. The samples/probes handling system is customized to fit with the $11 \times 11 \text{ mm}^2$ size with the handle sample plates and probe shuttles. The preparation chamber is equipped with basic surface preparation instrumentation. Transfer manipulator that combines two stations for cooling down to 100 K and for resistive heating in the range of 300 – 1000 K. Temperature control is possible using thermocouples mounted to the sample receptacles in the manipulator. An ion sputtering gun integrated with an Ar gas line is focused on the sample in the transfer manipulator position enabling annealing of the sample during sputtering or directly after sputtering without the necessity to transfer it. There is a second annealing station, reaching a much wider temperature range of 900 – 2700 K, that is a home-built e-beam heating station. The preparation chamber is also equipped with a leak valve connected to the oxygen gas line, enabling annealing in the oxygen atmosphere. The e-beam evaporator is attached to the port focused on the sample in the transfer manipulator position allowing for a reactive growth process. Additionally, there is a mass spectrometer for residual gas analysis and 10-position storage for samples and probes. Several, various sizes and localization windows allow to view inside the chamber. Sample/probe transfer within the preparation chamber stations is done using a wobble-stick manipulator. A linear transfer rod is used to transport between the preparation and analysis chambers.

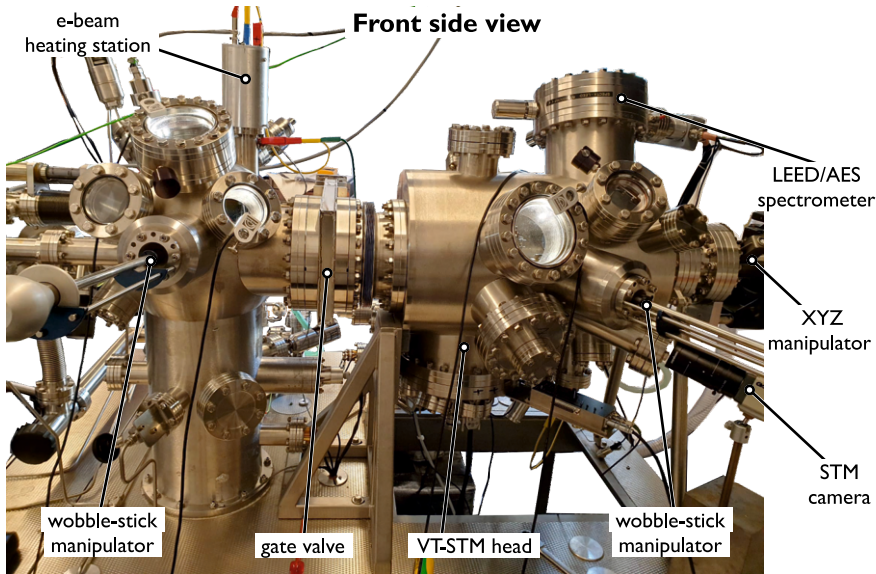


Figure 5.2: UHV system in Hamburg – front view photo of the preparation and analysis chamber. The most important facilities used in this dissertation are marked.

The preparation and analysis chambers are separated by a large gate valve. The analysis chamber consists of sample characterization tools, such as VT STM and LEED/AES spectrometer, as well as a clean molecular beam epitaxy setup. An analysis chamber was used for the alloy growth process and sample analysis. A 3D XYZ manipulator is attached to the analysis chamber, enabling annealing and cooling of the sample in the range of 100 – 1000 K. Using a 3D XYZ manipulator, the sample is positioned for the desired process: evaporation, LEED/AES analysis, or temperature control. Temperature control during the reactive growth of alloys is crucial. Therefore, in addition to the thermocouple in the sample receptacles of cooling and heating stations, it can also be controlled with a pyrometer. There are five e-beam evaporator ports that are focused on the sample placed in the 3D XYZ manipulator, and one focused directly on the sample receptacle in VT STM. A wobble-stick manipulator is used to transfer the sample between the transfer rod, 3D XYZ manipulator, and VT STM.

The VT STM head, shown in Figure 5.3, is cooled by a flow cryostat that is permanently connected to the 100 L He Dewar standing next to the UHV system foundation. Four cooling braids connected to the cold finger of the cryostat are directly connected on top of the STM head. In this setup, the entire STM head and its shields are cooled down to the setpoint temperature, resulting in extremely high thermal stability. Thermal shields surrounding the head reduce radiation effects. However, this setup has its drawbacks. The response time to any setting changes is longer, and it also elongates the cooling time of the STM starting from RT. The approximate temperature is adjusted by coolant flow control using a needle valve in the

transfer line between the Dewar and the cryostat and by a gas block valve between the cryostat and vacuum pump. Temperature stability at the level of 0.01 K is obtained using a heater placed in the cryostat. The combination of flow and heater settings allows to achieve a high stability temperature in the range of 20 – 300 K. To minimize mechanical noise, the STM is decoupled from the chamber by four springs and an eddy-current damping stage. The tunneling current signal is amplified by a variable gain low-noise current amplifier. The STM is computer-controlled using analog electronics, as depicted schematically in Figure 4.1. Spectroscopic results were obtained using lock-in with a built-in modulation signal generator.

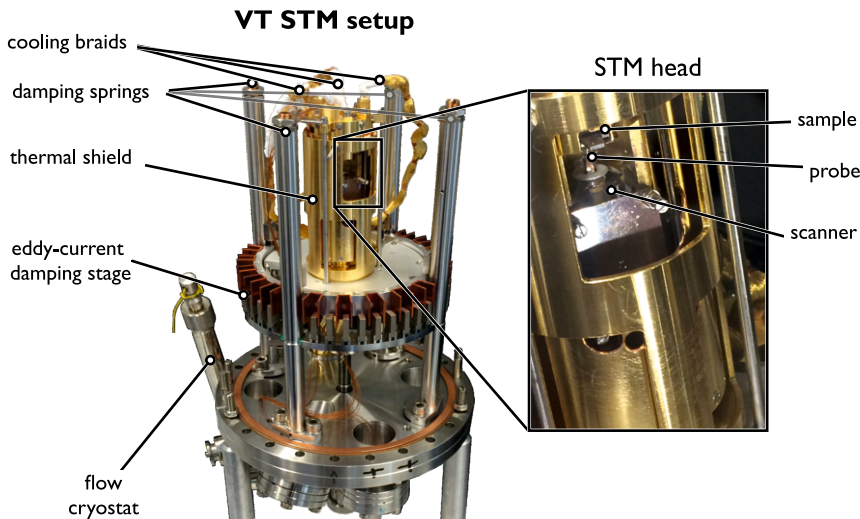


Figure 5.3: VT STM setup used in Hamburg – photo of VT STM assembly and zoom in on the STM head. The most important constructional elements are marked.

5.2 UHV system with VT STM in Poznan

At the Institute of Physics, Poznan University of Technology, a UHV VT STM system was used for the preparation of surface alloys and characterization of their structural and electronic properties. Originally, the setup designed by Ph.D. Eng. Maciej Bazarnik, and further modified by Ph.D. Eng. Emil Sierda, was equipped with an Omicron UHV RT STM/AFM hybrid. The description of the initial form of the full setup can be found in [133]. To achieve better resolution and thermal stability for improved quality results, the system was upgraded to a VT STM head designed by Ph.D. Eng. Maciej Bazarnik. I was involved in the assembly works of the STM head and upgrades of other UHV system elements to adapt the initial system to the design of the new STM head. The current state of the UHV system and its modifications are described below. Photos of the system in the final state are shown in Figures 5.4 and 5.5. The UHV system is a three-chamber setup consisting of a load lock, preparation, and analysis chambers.

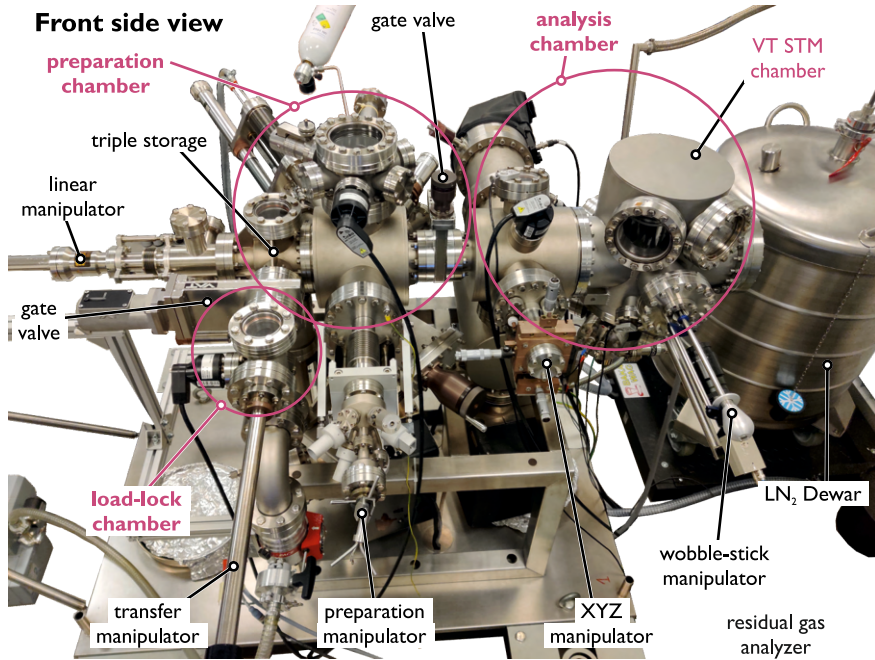


Figure 5.4: UHV system in Poznan – front view photo of the preparation and analysis chamber. The most important facilities used in this dissertation are marked.

The load lock is directly connected to the turbomolecular pump, which is coupled with a diaphragm pump by flexible hoses and separated by a butterfly valve. Pressure in the range from atmosphere to 0.001 mbar is controlled using a gauge integrated with a diaphragm pump controller. The further pressure range is monitored using a cold cathode gauge sensor connected directly to the load lock chamber. The linear and rotation transfer manipulator attached to the load lock chamber has one slot for commercial Prevac sample shuttles and transfers the sample/probe to the preparation chamber. The DN63 CF gate valve separates the load lock and preparation chambers. Both preparation and analysis chambers are equipped with ion-getter pumps and titanium sublimation pumps. In the preparation chamber, the pumps are separated from the chamber through a large gate valve, enabling the use of gases such as Ar and O without switching off the ion pump. The cold cathode pressure gauges measure pressure separately in both chambers. The base pressure of the system is 1×10^{-10} mbar. The system is decoupled from mechanical vibrations of the building and machines from other laboratories placed in the same building using two-stage decoupling. The UHV system is mounted on a rigid frame placed on containers with sand and, in turn, on a separate foundation. The preparation chamber is equipped with a linear magnetic manipulator that allows for the transfer of the sample shuttle between the load lock transfer manipulator, preparation manipulator, storage, and analysis chamber. The preparation chamber has one main focal point at the intersection of the transfer and preparation manipulators.

The preparation manipulator is a linear manipulator that allows cooling the sample shuttle down to the cryogenic temperatures, or anneal using different methods. Direct heating or e-beam heating can be used depending on the sample shuttle. The temperature of the sample can be controlled through K-type and C-type thermocouples, as well as a pyrometer mounted opposite the heating station. New mounting elements have been designed to hold a sample plate with dimensions of $12 \times 12 \text{ mm}^2$ and a handle instead of the standard Omicrom sample plates. There is also a special all-metal shuttle for LEED/AES experiments. A triple-position vertical storage is located in the preparation chamber, enabling quick sample shuttle exchange. The ion sputtering gun, combined with the Ar gas line and leak valve, is focused on the sample position in the preparation manipulator. There is also a leak valve and oxygen gas line attached to the multiport on top of the chamber. Three evaporators, including two metal e-beam evaporators and a triple home-made molecular evaporator, are centered on the focal point enabling a reactive growth process or deposition on a cooled substrate. A quartz-crystal microbalance controls the deposition rate of molecules or material from e-beam evaporators. A mass spectrometer, with a range of up to 100 amu, is attached to the preparation chamber for residual gas analysis. There are also a few spare DN40 CF ports in multiport on top of the chamber and the DN100 CF viewport directly above the focal point to observe the inside of the chamber.

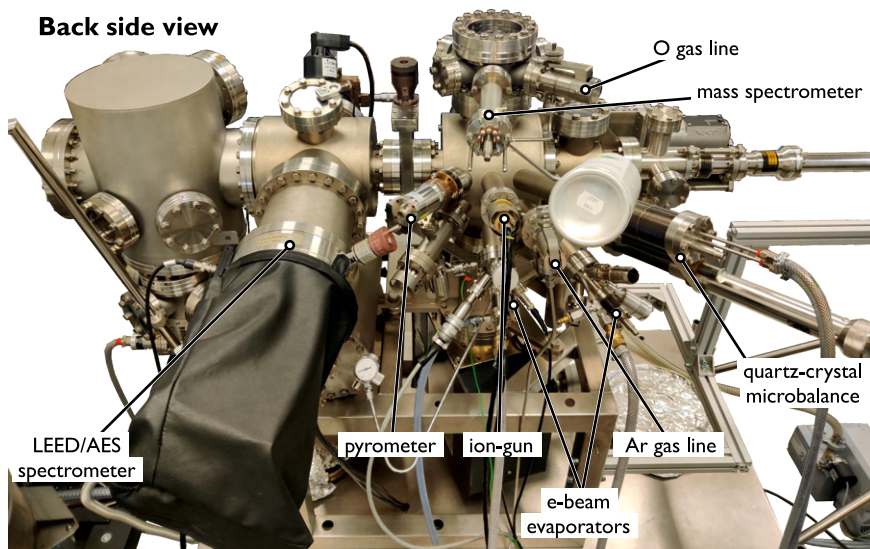


Figure 5.5: UHV system in Poznan – back view photo of the preparation and analysis chamber. The most important facilities used in this dissertation are marked.

The analysis chamber is separated from the preparation chamber by a gate valve. The analysis chamber is made up of two directly-connected segments. The first one, which is closer to the preparation chamber, apart from the aforementioned pumps and gauge, includes LEED/AES spectrom-

eter and XYZ manipulator. The sample on the LEED/AES sample shuttle is inserted into the XYZ manipulator handling using the long transfer rod from the preparation chamber. The sample position with respect to the spectrometer is adjusted using the XYZ manipulator. The second segment is a custom-made chamber, which I have designed for the new VT STM head.

The VT STM head is positioned off-center in the chamber to allow for the transfer manipulator from the preparation chamber. A wobble-stick manipulator, located in front of the VT STM head, picks up the sample/probe from the sample shuttle on the transfer rod. Two large DN100 CF windows in the top front facilitate manipulation control of the sample/probe to the VT STM head or storage. The 10-position storage, located next to the outer shield, includes two positions with a wider separation distance between them, which are dedicated to the tip shuttle storage. The other positions are intended for samples. Two DN40 CF ports are located in the front-down position, focused on the sample position in the VT STM head. One port is dedicated to the camera for controlling the coarse approach, while the other is intended for mounting the evaporator to enable deposition on the cold substrate directly in the VT STM head. A large CF window is located on the right side, revealing the view through the entire system up to the transfer rod in the preparation chamber. There are also two spare DN63 CF ports. On the bottom of the chamber, there is the DN250 CF flange. Asymmetric reducer from DN250 CF to DN100 CF enables for non-centered attachment of the VT STM head. Between the flow cryostat described in detail in Subsection 5.2.2, there is a multiport for the electrical connection of the VT STM head. The STM head is computer-controlled using analog electronics, as depicted schematically in Figure 4.1. Spectroscopic results were obtained using a lock-in amplifier with a built-in wave function generator.

5.2.1 Multipurpose STM head

The multipurpose STM head was designed by Ph.D. Eng. Maciej Bazarnik and I participated in the assembly and modifications of the head prototype. Figure 5.6 shows a visualization of the design and photography of the assembled head. The tube piezoscanner from EBL Products Inc. is the heart of the STM head. It is an EBL #4 tube made from lead zirconate titanate, with an outer diameter of 6.35 mm, 0.51 mm thick wall, and length of 38.6 mm. Four gold-coated copper electrodes, with axial segmenting of 90° quadrants, are on the outer side of the piezotube. The fifth electrode is on the inner wall of the piezotube and wraps on the top of the outer wall to ease the connections. The scanner bends by applying the voltage to its electrodes, due to the inverse piezoelectric effect, as described in Subsection 4.1. Since the bending range depends on temperature, reference samples were imaged to calibrate the scanner sensitivity for various temperatures. Lateral sensitivity was estimated on the base of interatomic distances using atomic-resolution images, while the vertical calibration was derived from the step height by imaging several monoatomic terraces of clean surfaces. At 300 K the Au(111) sur-

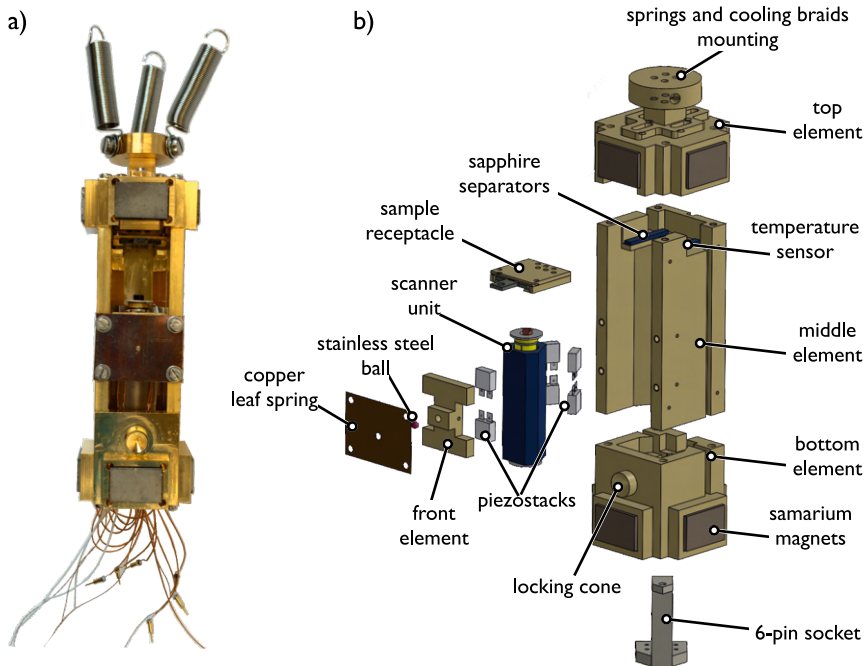


Figure 5.6: STM head – a) photography and b) project visualization of STM head designed by Ph.D. Eng. Maciej Bazarnik. The most important elements of the construction are marked.

face was measured, reaching the lateral sensitivity of 80.7 nm/V and vertical sensitivity of 13.48 nm/V. For 75 K, the Pt(111) surface served to calibrate the scanner reaching 25.8 nm/V and 4.31 nm/V for lateral and vertical sensitivity, respectively. The probe, in a tungsten probe holder, is placed in an insulating probe receptacle body with a copper holder and leaf spring. The outer side of the probe receptacle body is partially covered with the conductive layer. The probe receptacle body is drilled in the bottom, to put the I_t cable inside (coaxial subminiature cable MMK5001 from el-spec GmbH Electronic-Vertrieb). The inner conductor is soldered to the copper holder, while its shield (outer conductor) is glued to the conductive layer on the outer wall of the receptacle. The bottom of the piezotube is glued with a sapphire prism by a centering end cap, which positions the piezotube centrally with respect to the hole in the prism. The probe receptacle body is glued to the upper part of the piezotube and the I_t wire is led through the piezotube. The ceramic elements of piezoscaner assembly are made from SHAPAL™ Hi M Soft ceramics. Cables for piezoscaner electrodes are glued directly to the electrodes and they are led along the unpolished prism walls. For $x+$, $x-$, $y+$, and $y-$ electrodes the twisted pair cable with two copper 0.1 mm diameter wires is used. For the Z electrode, same as for I_t , a coaxial subminiature cable is used. The body of the STM head consists of three main elements, namely the top, middle, and bottom, which are screwed to-

gether. Most of the body parts are made of phosphor bronze (CuSn_8) coated with $20 \mu\text{m}$ of the gold layer, except where otherwise stated. The middle part contains the sample receptacle with a leaf spring tightening the sample inside. Two sapphire separators are placed between the sample receptacle and the middle part to ensure that the sample is electrically isolated from the STM body but at the same time maintains good thermal contact. A cryogenic temperature sensor, DT-600 series silicon diode from Lake Shore Cryotronics, Inc., is glued to the side of the sample receptacle. The location of the temperature sensor is selected, so the temperature is measured as close as possible to the sample, to reduce the temperature uncertainty factor. The twisted pair cables, made of kapton-insulated Cu wire FTAK01010 from Kurt J. Lesker, are used for four-point temperature measurement. The cables are led along the chamfer on the right side of the body and go down to the socket. The coaxial subminiature cable, dedicated to the bias, is attached to the top of the sample receptacle and goes through the chamfer in the STM body on its left side. There are six piezostacks with $2 \mu\text{m}$ traveling length model $P - 1 \times 1.0 \times T$ PICA Shear Actuators from PI Ceramic GmbH. Four of them are glued to the middle part of the body, while two others are glued to the front element which presses the prism with the scanner. Piezostacks are located in pairs, diagonally, with a 10 mm distance between the inner edges of the pair. The front element is mounted to the body using a copper leaf spring screwed to the body and a stainless steel ball. Tightening the screws can regulate the pushing force exerted on the prism, enabling the slip-stick mechanism used for the coarse approach of the prism which carries the piezoscanner. Four piezostacks cables are led through the chamfer in the STM body on its backside, while the cabling of the front element goes directly down to the socket through the bottom element. The top and the bottom parts contain four CoSm magnets $15 \times 10 \times 5 \text{ mm}$ (each) glued to the grooves. The bottom part has a through hole inside to bring out the cabling. On the front side, there is a counter-cone and on the back side, there is a cone used for locking the STM head and increasing the thermal contact. From the bottom, there is a Macor[®] 6-pin socket for piezostacks cabling. The top part is an assembly containing not only the magnets but also the connection of the cooling braids and springs. The cooling braid is a modification introduced to increase the thermal contact of the STM head with an inner thermal shield. It is formed as a spring-shaped combination of three braids made of oxygen-free copper wires of section area 1.5 mm^2 and a single strand with 0.1 mm diameter. The three braids are attached to the STM head by screwing them to the spring mount element, while their other ends are soldered and screwed to the top panel of the inner thermal shield. The cooling braid is formed in such a way as not to affect the position of the head (do not press, pull or twist it). Mounting of the STM head to the inner thermal shield is by three springs made of nonmagnetic, stainless steel, with 58 coils and a wire diameter of 0.25 mm . The STM head has a two-level damping stage. The springs isolate the STM head and limit the transmission of vibrations, while magnets in the top and bottom parts of the body reduce vibrations *via* eddy current damping. Both, springs and cooling braids are

screwed to the top panel of the internal thermal shield using sapphire washers to avoid their galvanic contact. The STM head assembly is shrouded by the inner thermal shield made of gold-coated oxygen-free copper. The bottom part of the shield is attached to the cryostat heat exchanger, which allows the whole assembly to be cooled down to the desired temperature. Four 270 mm length rods are screwed into the base and serve as a frame for the shield. Side and top panels are screwed together to the rods forming a rigid frame. The front panel contains sliding doors that enable the sample and probe to be inserted and removed from the STM head. This design also permits single atoms, molecules, and clusters to be deposited without removing the sample from cryogenic conditions. The front panel also features a locking screw plate. Tightening the screw into the counter-cone pushes the STM body to the back, thus the cone in the STM body fits into the counter-cone in the back panel of the inner thermal shield (which position is also regulated), increasing the thermal contact with the internal shield. Initially, that was the main thermal contact point. The addition of cooling braids has improved the cooling efficiency of the STM head. The locked position is also used to exchange samples and probes. Unscrewing the locking screw breaks the galvanic contact of the STM head with the chamber. A 16-pin socket for cryostat connections (cryostat temperature and heater) is screwed to the bottom of the front panel. The left panel contains the 24-pin PEEK socket for all signals from the STM head. The second-stage thermal shield made of aluminum surrounds the inner thermal shield and STM head. The outer shield base is press-fitted onto the cryostat. The tube with 66 mm inner diameter and 395 mm height is screwed to the base. Within the tube, there is a rotating slide giving access to the part of the inner thermal shield and STM head. Photographs of the shields are shown in Figure 5.7. Cooling

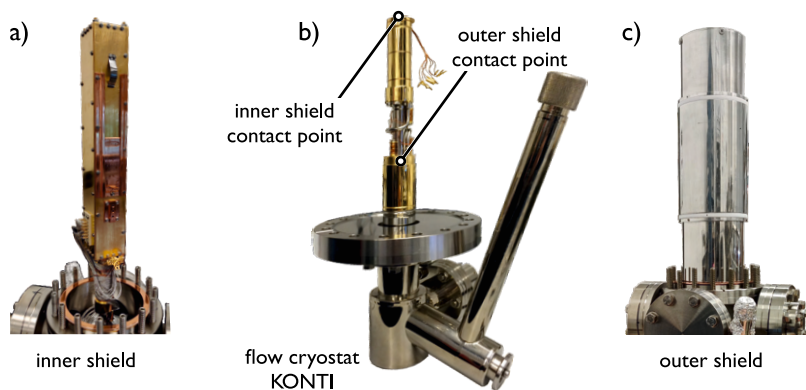


Figure 5.7: Multipurpose STM head – photographs of thermal shields with marked contact points to the cryostat; a) inner shield, b) cryostat and shields' contact points, c) outer shield.

down the whole STM head assembly with the inner thermal shield gives a relatively large heat load to cool down, but the great advantage of this solution is its high thermal stability at the level of 0.001 K. The graph of cooling

down the temperature of cryostat (blue) and STM head (pink) using liquid nitrogen (LN_2) is shown in Figure 5.8 a). The cryostat cools down with a linear dependence to the setpoint within 3 hours, and the entire setup can be cooled down from RT in less than 24 hours. The proposed design allows for very efficient use of LN_2 with an amount of less than 4 kg per 24 hours. In the setup described in Subsection 5.2, the cryostat is connected to the 200 L Dewar for LN_2 storage CS200S from CryoVac Gesellschaft für Tieftemperaturtechnik mbH & Co.KG. Figure 5.8 b) shows the LN_2 consumption graph, proving the efficiency of the implemented setup.

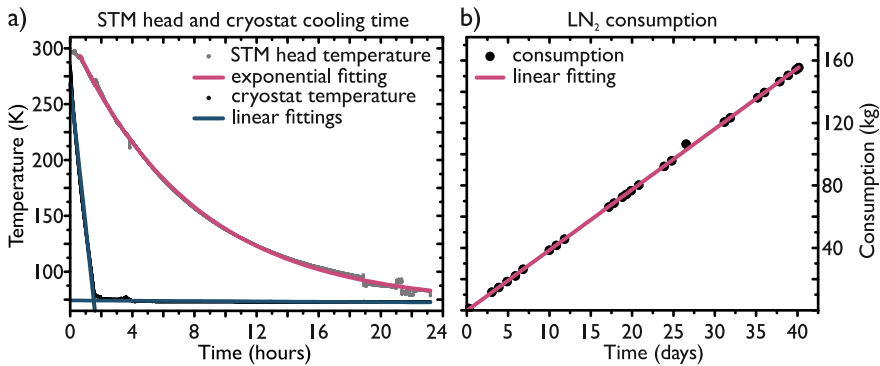


Figure 5.8: Operating parameters of VT STM setup cooled with LN_2 – graphs of main operating parameters; a) STM head and cryostat cooling time, from RT to the operating temperature of 73 K, b) LN_2 consumption during normal operation.

5.2.2 Cryostats

In the VT STM systems described in Subsections 5.1 and 5.2, flow cryostats are utilized to cool down the heads. The following Subsection will focus primarily on the construction and operational principle of the flow cryostats and their integration into the STM heads. The second part proposes the concept of adaptation of the STM head described in Subsection 5.2.1 to the low temperature (LT) setup with Joule-Thomson (JT) effect cryostat is proposed.

Continuous-flow cryostat

Continuous-flow cryostats require a permanent supply of cooling liquid, typically liquid helium (LHe) or liquid nitrogen (LN_2). The VT STM system in Hamburg, described in Subsection 5.1, uses LHe as a cooling agent, while VT STM in Poznan (Subsection 5.2) uses LN_2 . However, both cryostats allow for the operation of both cooling liquids. Both systems use KONTI flow-cryostats from CryoVac Gesellschaft für Tieftemperaturtechnik mbH & Co KG. A scheme of the continuous-flow cryostat operating principle is shown in Figure 5.9. The cooling liquid is stored in a storage Dewar placed next to the system, but on a different foundation than the UHV system to

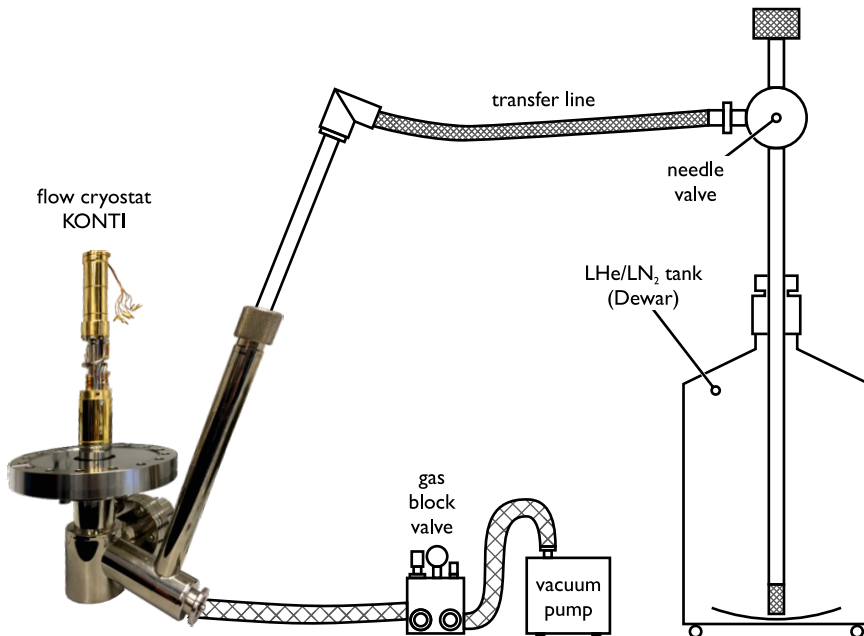


Figure 5.9: Continuous-flow cryostat – scheme, combined with photography, of continuous-flow cryostat presenting operating principle and the most important elements.

avoid mechanical vibrations. The cryostat is connected to the Dewar using a stainless-steel U-tube transfer line with rigid sides and a flexible coaxial tube between them. On the Dewar side, the transfer line is introduced using a sliding o-ring seal down to the bottom of the Dewar to enable the use of the entire cooling liquid. The cooling liquid is drawn into the transfer line by the vacuum pump connected to the opposite side of the circuit. The flow of the cooling liquid is regulated mainly through the needle valve on the transfer line and additionally by the gas block valve regulating pumping speed. The needle valve allows for precise flow regulation, which is essential to maintain low cooling liquid consumption and stable temperature. The cooling liquid is fed into the cryostat through the transfer line, where it is transformed into the gaseous form and fed further to the main heat exchanger. The VT STM head is connected to the external side of the exchanger, and cooling occurs through direct heat conduction. The heat exchanger is designed to provide homogeneous heat distribution. Temperature control is performed by manipulating the flow rate supported by a heater with a PID control loop. A solid thermal contact between the heat exchanger and the VT STM head is necessary for effective heat transfer. After flowing through the main heat exchanger, the gaseous cooling agent is fed to the secondary heat exchanger, where the remaining gas cools down the thermal screen around the main heat exchanger creating a low heat radiation environment. The cooling agent gas leaves the cryostat and goes to the vacuum pump through the gas block valve [134]. Considering the price and deficiency of LHe, the VT STM

cooling system in Hamburg is connected to the helium recovery installation. Helium gas from the pump is further transformed into a liquid using a helium liquefier installation. In the case of LN₂ cooling line in Poznan, there is no recovery system. Cooling retention time is dependent on the volume of cooling liquid available. In principle, both systems are cooled continuously, while the cooling liquid is refilled without warming up the VT STM head. LHe is refilled from the external Dewar to the operating Dewar, which is permanently connected to the cryostat. LN₂ Dewar in Poznan is refilled directly and the cooling system is disconnected for this time. Both refilling methods require a few hours to restore the measurement conditions.

Closed-cycle cryostat

The following Subsection outlines the utilization of the LT system with the STM head, as described in Subsection 5.2.1. The final form of the cooling system is the result of Ph.D. Eng. Maciej Bazarnik's cooperation with Cryoandmore Budzylek GbR, who collaborated on the production of a cryostat for LT STM purposes allowing for operation at temperatures below 2 K. Sub-4 K ultra-low vibration UHV closed-cycle system is a cooling system al-

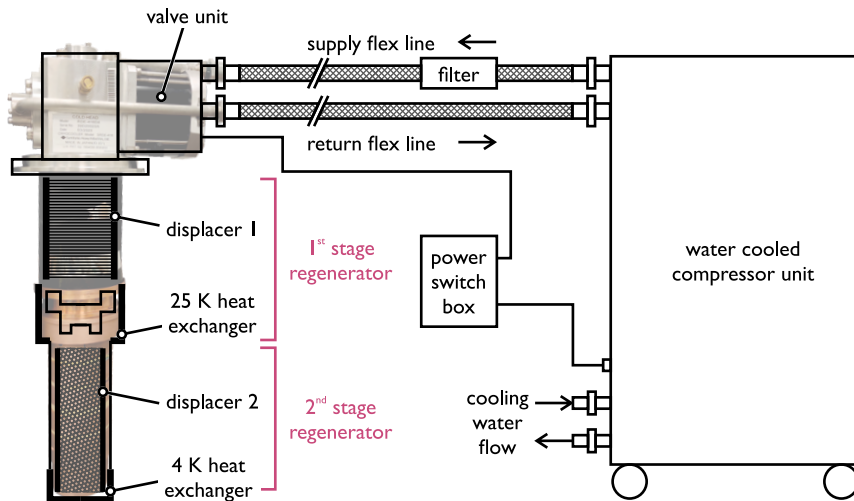


Figure 5.10: Gifford-McMahon refrigeration cycle – scheme, combined with photography, showing the Gifford-McMahon refrigeration cycle.

lowing for continuous operation at a temperature of 4 K in a closed circuit using only the Gifford-McMahon cooling stage. Alternatively, it can operate at a temperature below 2 K using an additional Joule-Thomson (JT) circuit. The first cooling level, down to 4 K, is achieved using Sumitomo RDK-415D2 cold head shown in Figure 5.10. It is a two-stage closed-cycle cryocooler that operates on the Gifford-McMahon refrigeration cycle. The high-pressure He gas is supplied from the compressor through the supply line, which includes a filter unit to the cold head. Within the cold head, the high-pressure He flows through the valve unit and passages to the displacer assemblies. There

are two stages of displacer-regenerator assemblies. The first stage displacer assembly is connected to the Scotch yoke, which is set into motion by the motor through the crank. The Scotch yoke converts the rotational movement of the motor to the reciprocation motion of the displacer. The crank is also responsible for the movement of the rotary valve which controls the opening time of the He gas supply and return lines. The displacer assembly slides within the cylinder and the He gas flowing through the porous material (the regenerator) is cooled down *via* the JT effect, as shown in 5.11. At

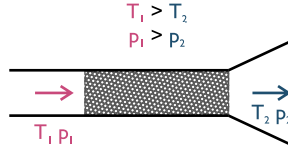


Figure 5.11: Joule-Thomson effect – scheme explanation of JT effect.

the first heat exchanger, after the first stage, the He gas reaches 25 – 45 K, depending on the heat load. The second stage displacer assembly contains a special rare earth metal material within the regenerator thus ultimately reaching 3.5 – 4.2 K in the heat exchanger. No physical work is required to move the displacers within the cylinders. The pressure in the cold head is increased or decreased only through the rotary valve opening the supply and return line, alternatively. Cooled He gas flows to the motor housing through the crankcase and exits the cold head through the return coupling to the return line, and enters back to the compressor. The Gifford-McMahon head is decoupled from the system galvanically using the hydraulic stand, therefore avoiding mechanical contact. The heat is transferred to the internal cryostat elements *via* exchange gas and further to the STM head. This closed-cycle cooling can run continuously for an indefinite period, allowing for STM measurements at a temperature of 4 K. The setup can reach temperatures below 4 K by using an additional JT circuit or a 1 K pot system. There is a bellow with exchange gas inside between the 4 K stage and mounting plate. After the initial cooling down to 4 K, it is pumped out of the internal heat exchanger to avoid coupling to the 4 K stage. The JT circuit is filled with He gas and pumped by the vacuum pump through the JT cooling system. The He gas is pre-cooled by a Gifford-McMahon cryocooler by contact point and additionally by its own backflow line. The He gas passes through the very thin capillary, which can also be a porous material, serving as a resistance for the gas. Cooling down to the final temperature occurs close to the heat exchanger on the mounting post. The mounting post is connected with the STM head and thermal shields assembly by three rigid Cu rods. The final temperature depends on the power of the vacuum pump forcing the He gas flow. In this setup, the lowest achieved temperature was 1.4 K. The He gas flowing out of the circuit pre-cools the gas flowing into the JT circuit. The He gas from the backflow line exits the JT circuit and is exhausted through the vacuum pump into the air. Here, the JT circuit works as an open cycle, so the operation time depends on the He resources in the supplying gas line.

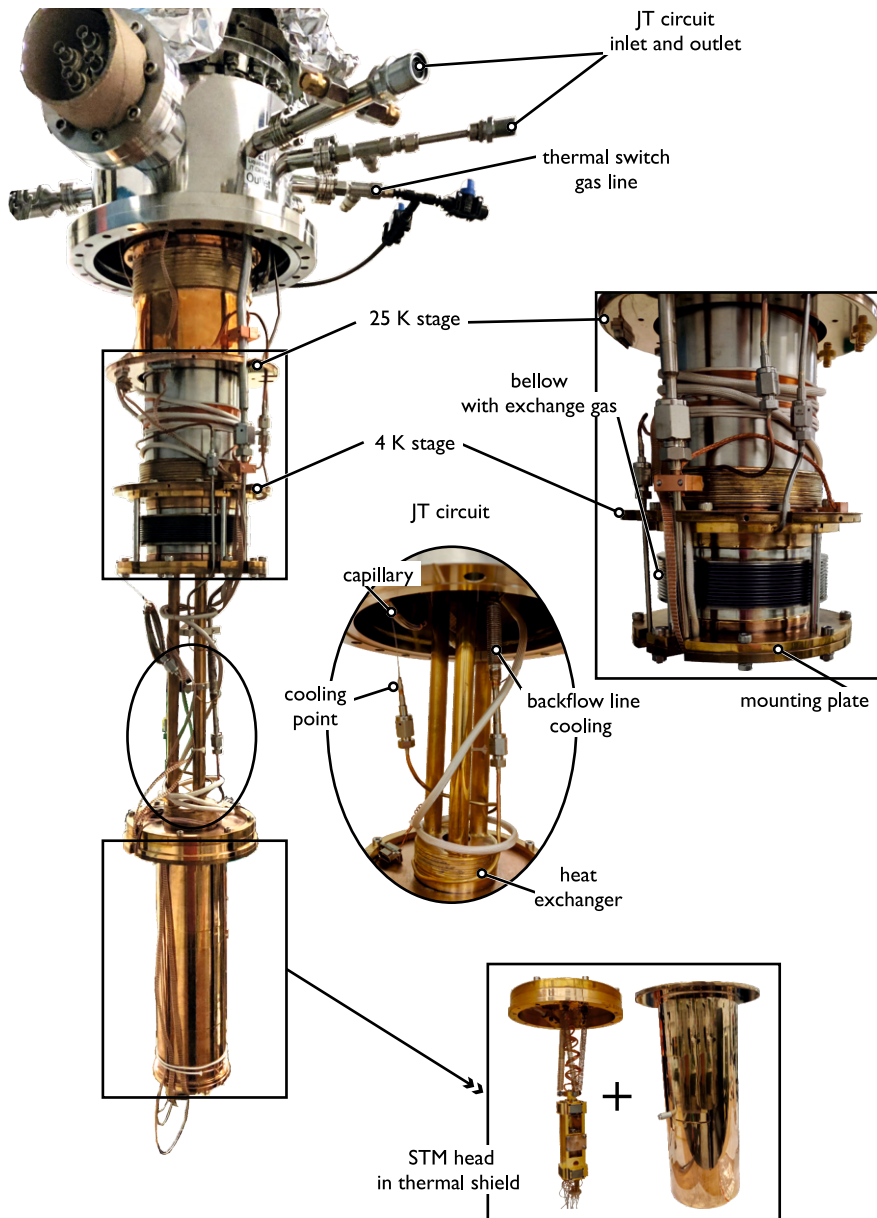


Figure 5.12: Gifford-McMahon and JT combined cryostat – photos of the cooling setup. The most important facilities crucial for the explanation of operation principles are marked.

5.3 X07MA X-Treme beamline

Swiss Light Source (SLS) located at Paul Scherrer Institute (Switzerland) is the third-generation synchrotron light facility. It has 16 beamlines and 22 endstations, with a 288 m perimeter storage ring that provides the electron beam with energy 2.4 GeV producing photon beams with high brightness and stability. The X07MA X-Treme is a soft x-ray beamline dedicated to XAS/XMCD measurements at a high magnetic field and low temperature. The x-ray source is a pure permanent magnet APPLE II helical undulator that provides variable polarization, including linear polarization with any angle between $0 - 90^\circ$, and left or right circular polarization. Table 5.1 summarizes the most important technical parameters of the X-Treme endstation [135].

Table 5.1: X-Treme beamline setup – summary of the most important technical parameters of the endstation [135].

Parameter	Value/description
X-ray energy range	400 – 2000 eV
Focused spot size	exit slit \times 230 μm^2 ($V \times H$)
Polarization	Linear: any angle in range 0 (horizontal) – 90° (vertical) Circular: right / left
Max. field along beam direction	7 T
Max. field in 3D mode	2 T
Sample temperature range	2 – 350 K
Detection modes	TEY (total fluorescence yield or transmission can be acquired in parallel with TEY)

The optical layout of the X-Treme beamline is shown in Figure 5.13. First, the x-ray beam leaving the undulator passes through the collimating mirror. Further, it goes through the most important optical element in the setup which is a plane grating monochromator. The first mirror is used for horizontal focus, while the focusing mirror in the exit slit is used for vertical focus. The beam is then refocused at the sample by the refocusing mirror. The beam size can also be reduced by removing the last mirror and using motorized apertures before the refocusing and focusing mirrors [135].

The X-Treme endstation is composed of three chambers and a cryostat, as shown in Figure 5.14. Samples are loaded to the UHV system through the load lock chamber and then transferred to the cryostat (in the case of *ex situ* prepared samples), or to the fully equipped preparation chamber, through the transfer chamber. Both, the load lock and transfer chamber have a parking stage for storing 2 – 3 samples. The preparation chamber allows for *in situ* preparation and rough identification of prepared samples. It is equipped with an ion gun, a heating stage (20 – 1500 K), e-beam and molecular evaporators, quartz crystal microbalance, and Ar and O gas lines. There are also spare DN40 CF ports in the preparation chamber to connect any additional necessary equipment. This setup is suitable for surface alloy

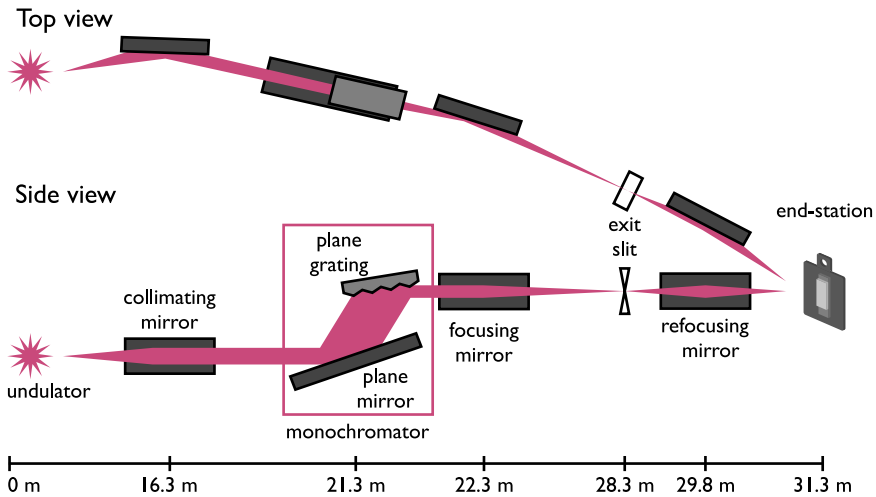


Figure 5.13: X-Treme beamline setup – optical layout scheme of the beamline. Figure reproduced from [135].

preparation using a reactive growth process. Additionally, the preparation chamber is equipped with analytical tools for quick verification of prepared samples, including a VT STM and a LEED/AES setup. The prepared sample is transferred through the transfer chamber to the cryostat. It is equipped with a 2 K sample insert and superconducting 2D vector magnet operating at 7 T in a single direction and up to 2 T for the vector field. The main detection mode is TEY, however, it is possible to use transmission or total fluorescence yield detection mode at a time [135].

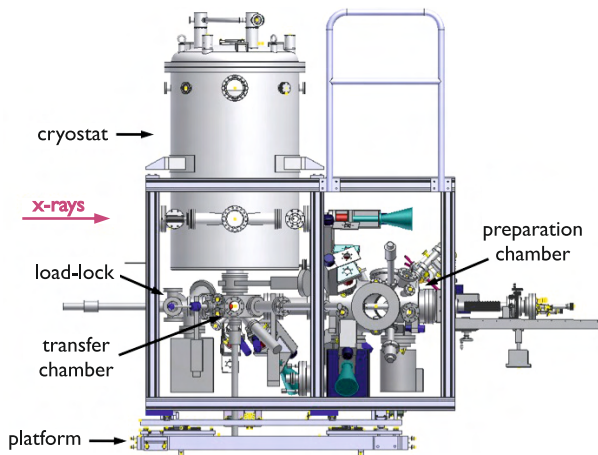


Figure 5.14: X-Treme beamline setup – a scheme of the endstation showing overview of all chambers used for sample transfer and preparation and conduction of the experiment. Figure taken from [135].

5.4 BL-29 BOREAS beamline

ALBA synchrotron is a third-generation facility located in Cerdanyola del Vallés, Spain. It is operated by the Consortium for the Exploitation of the Synchrotron Light Laboratory (Consortio para la Construcción, Equipamiento y Explotación del Laboratorio de Luz de Sincrotrón). The storage ring has a circumference 270 m and produces an electron beam with energy 3 GeV. Currently, ALBA has 10 operational beamlines and 4 under construction. The BOREAS beamline has two endstations that use soft x-rays: HECTOR for absorption experiments (used within the dissertation) and MARES for scattering and reflection experiments [136] (Figure 5.15). The x-ray source for the BOREAS beamline is the same as that of the

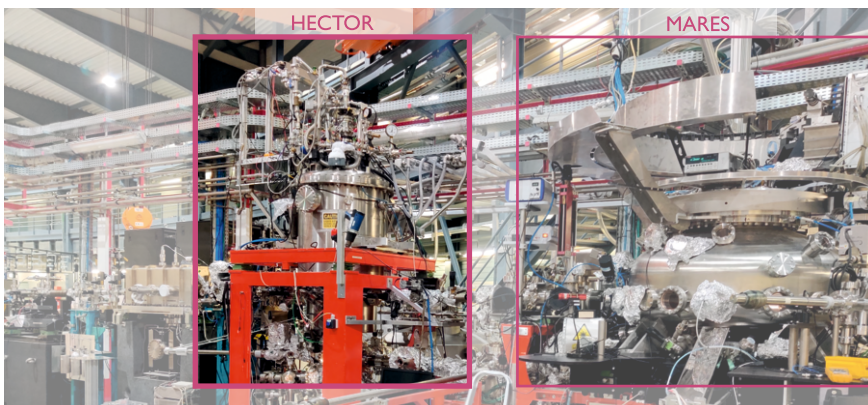
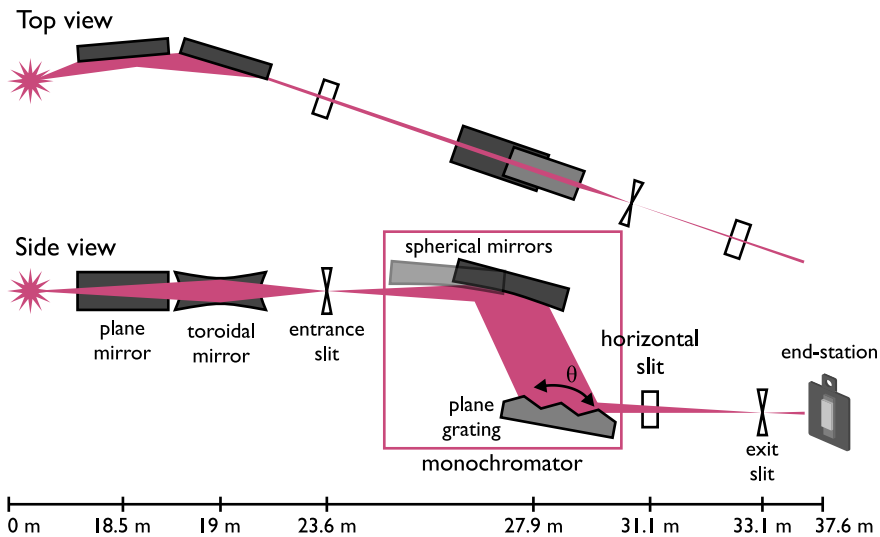


Figure 5.15: BOREAS beamline setup – a photo of the endstations: HECTOR (for soft X-ray absorption techniques such as NEXAFS, XMCD or x-ray magnetic linear dichroism) and MARES (for scattering and reflection experiments: resonant soft x-ray reflectivity or resonant magnetic scattering).

SLS X-Treme beamline described in Subsection 5.3, an elliptical undulator APPLE II with variable polarization. The most important technical parameters of the BOREAS beamline and HECTOR endstation are summarized in Table 5.2 [136]. Despite similarities, the BOREAS beamline differs from X-Treme in terms of its optical layout, as shown in Figure 5.16. The x-rays beam outgoing from the undulator passes through the pre-optics section first. It consists of a plane mirror that removes a major part of unwanted radiation and heat loads and a toroidal mirror that focuses the beam vertically on the entrance slit and horizontally on the virtual plane. Then, it goes through the entrance slit to the variable line spacing plane grating monochromator. There are two spherical mirrors and three interchangeable plane gratings. Such a monochromator allows for fast scans (the change of energy is done simply by the rotation of the gratings) and ensures high photon flux and good spectral resolution over an extended energy range. After the exit slit, the photon beam is refocused and collimated in refocusing section with a set of bendable plane elliptical mirrors [137]. The main part of the HECTOR endstation is the cryostat and experimental setup, which is the twin set to

Table 5.2: BOREAS beamline setup – summary of the most important technical parameters of the beamline and HECTOR endstation [137].

Parameter	Value/description
X-ray energy range	80 – 4000 eV
Focused spot size	variable between $< 100 \times 80 \mu\text{m}^2$ and $> 1 \times 1 \text{ mm}^2$ ($H \times V$)
Polarization	Linear: any angle in range 0 (horizontal) – 90° (vertical) Circular: right / left
Max. field along beam direction	6 T
Max. field in 3D mode	2 T
Sample temperature range	2 – 350 K
Detection modes	TEY, total fluorescence yield, transmission

**Figure 5.16: BOREAS beamline setup** – optical layout scheme of the beamline. Figure reproduced from [136].

the X-Treme endstation described in Subsection 5.3. The cryomagnet operates at 6 T along the beamline direction and up to 2 T perpendicular to the beam and for 3D operating mode. Samples are mounted on a sample shuttle attached to the cold finger of the VT insert (2–350 K). The VT insert is electrically insulated to allow for drain current registration. The main detection mode is TEY, but total fluorescence yield and transmission modes are also possible. A 5-chamber UHV system is fully equipped for the preparation of surface alloys and rough verification of prepared samples prior to the actual measurement. The load lock chamber enables to load up to 4 samples at a time. Further, the sample can go to the first preparation chamber, below the magnet, which is equipped with a cleaver, a scraper, molecular beam epitaxy evaporators for metals and organic molecules, and an ion sputtering gun. Alternatively, there is a second preparation chamber which is fully

equipped with an e-beam heating station up to 2000 K, a pyrometer, an ion sputtering gun, e-beam metal evaporators, molecular evaporators, a quartz crystal microbalance, Ar and O gas lines, and LEED/AES spectrometer. Additionally, there are few spare ports for users to connect external devices. The last chamber is equipped with VT STM and another LEED/AES spectrometer. Between preparation chambers and the STM chamber, the sample is transferred automatically through the UFO-type chamber using Python commands [137]. Overall, the ALBA synchrotron is a highly advanced facility that offers researchers the ability to perform cutting-edge experiments using soft x-rays.

Chapter 6

Results and discussion

The following Chapter describes the experiments and the analysis of their results. First, the substrate's structural, electronic, and chemical properties are analyzed to have a comparative basis for further results analysis. Then the general description of surface alloys formation is presented. Two preparation methods of surface alloys are compared, indicating their advantages and disadvantages. An analysis of the thermal evolution of surface alloys is presented, which allowed me to determine the temperature ranges in which surface alloys are formed. The next two Subsections concern Gd-Pt surface alloys (Subsection 6.3), and Dy-Pt surface alloys (Subsection 6.4). Both have the same agenda. The Subsection begins with describing the properties of the selected REM element and determining the conditions for the growth of ordered REM-Pt structures. Next, the identified surface alloys are shown. Their analysis begins with the structural properties based on large-scale and atomic-resolution STM topography images and models. Further, the structure in reciprocal space observed with LEED is compared with the simulated diffraction pattern and then with the structure observed in real space. Afterward, the electronic properties are investigated using LTS/PTS and DFT calculations. In the case of the Dy-Pt system, the local surface work function is determined using field emission spectroscopy. Finally, the REM-Pt surface alloys area occupancy graphs as a function of REM coverage (and substrate temperature for the Gd-Pt system) are presented to summarize the first part of the experiments. The second part of these Subsections concerns the magnetic properties of the surface alloys based on XMCD experiments. First, the easy magnetization axis is determined based on the hysteresis loops' signals. Next, the coercive field and T_C are determined based on field-dependent and temperature-dependent measurements. Further, the orbital and spin magnetic moments are determined using sum rules, and finally, the magnetic anisotropy is estimated.

Within this Chapter, the color convent presented below is preserved to facilitate the analysis. Depending on the structure, surface alloys are marked as follows: 1 L REM-Pt₂-type, 3 L REM-Pt₂-type, 1 L REM-Pt₅-type, and

2 L REM-Pt₅-type. Colors used for models and simulated LEED patterns are also consistent within the Subsections and analyzed structures and they are described in the relevant Sections. In XAS graphs **red** indicated the spectrum taken for **negative (left) circular light polarisation** and **navy color** indicated the spectrum taken with **positive (right) circular light polarisation**. **Yellow color** denotes signal registered for **grazing incidence angle**, while **navy color** denotes signal registered for **normal incidence angle**.

6.1 Platinum (111) single crystal

Surface alloys were grown on the (111) face of Pt single crystals. Pt was chosen as a substrate for three reasons, as outlined in Chapter 3. First, it behaves like a paramagnet and is easily polarizable, thus may play a crucial role in the mediation of interactions between magnetic REM atoms. Second, high spin-orbit coupling of Pt may lead to exotic, non-collinear magnetic structures. Finally, Pt is widely used in proton exchange membrane fuel cells due to its high activity toward oxygen reduction reactions. In this context, alloying Pt with REM may lead to the production of substitute materials with enhanced efficiency of the oxygen reduction reaction.

Once the Pt single crystal covered with REM is annealed, the substrate gets poisoned with REM atoms which diffuse into the bulk. For this reason, separate crystals were used for each REM-Pt system experiment to prevent REM intermixing. All substrates with a purity of 99.999 % and custom dimensions, were supplied by MaTeck, GmbH, Germany. Despite the residual impurities in the crystal volume, a clean (111) surface can be prepared following the standard procedure for Pt(111) crystals described in the literature [138]. Typical substrate preparation starts with 30 minutes of Ar-ion bombardment at a base pressure of 5×10^{-6} mbar and 1 keV acceleration energy of the ion beam. Further, to heal the surface, the substrate is annealed for 20 minutes at a temperature of 1000 K. An oxygen atmosphere at a level of $1 - 5 \times 10^{-8}$ mbar is used to remove carbon impurities diffusing from bulk at elevated temperatures. Oxygen remains are removed by a final 5-minute flash up to 1300 K. This procedure was repeated until the number of impurities on the surface was less than 2 %. Before REM deposition, the Pt(111) substrate was characterized using STM imaging, PTS, AES, and LEED techniques to verify surface cleanliness. In general, repeating the above procedure three times gives a clean Pt(111) surface, between successive surface alloys preparations. Directly after the preparation, the samples were transferred *in vacuo* into the analysis chamber. For local investigations using STM, the samples were inserted into the STM head and cooled to the measurement temperature of 30 K. Electrochemically etched tungsten probes, cleaned by standard *in situ* procedures, were utilized for the STM studies. Topographic data were obtained in CCM and processed using GWYDDION software [139]. The STM images were only treated with plane flattening and, if necessary, a change of the z-scale range to improve the visibility of key features. The tunneling spectra were recorded in CHM after probe sta-

bilization at specific parameters, namely U_{stab} and I_{stab} . The differential tunneling conductance (dI_t/dU) was measured *via* lock-in technique by applying modulation voltage to the sample bias voltage with a peak-to-peak value amplitude $U_{\text{pk-pk}}$ and a frequency ω_{mod} that were specified for each data set. All spectroscopic data were processed using self-written Python scripts. The LEED and AES measurements were performed directly after STM characterization in the same analysis chamber. Results obtained for pure substrate as well as the Gd-Pt system were additionally supported by DFT calculations performed by Ph.D. Eng. Michał Hermanowicz and further processed using self-written Python scripts. A single surface unit cell of each surface alloy on top of 25 layers of Pt(111) was used for calculations. Geometry was optimized within LDA using the Broyden-Fletcher-Goldfarb-Shanno method as implemented in the QUANTUM ESPRESSO code [140, 141]. The PDOS was calculated within the Perdew-Burke-Ernzerhof generalized gradient approximation for the exchange-correlation functional as implemented in the SIESTA software package [142–144]. Magnetic moments were calculated using the Mulliken charge analysis. More details on the theoretical calculations can be found in the experimental section of [145].

The results of the structural characterization of Pt(111) are presented in Figure 6.1. Figure 6.1 a) shows an illustrative large-scale STM image of Pt(111) surface, while Figure 6.1 d) presents a profile plot reproduced along the line marked in Figure 6.1 a) demonstrating mono-atomic steps. The

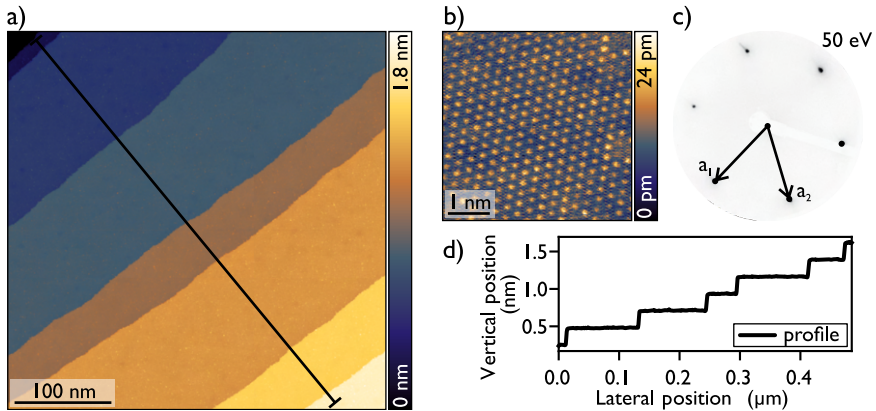


Figure 6.1: Pt(111) substrate – a) large-scale STM image overview of the substrate after preparation procedure; b) atomic-resolution STM image of Pt(111) atomic structure; c) image of LEED pattern of the cleaned substrate showing (1×1) reconstruction of pristine Pt(111) ($E_{\text{beam}} = 50$ eV); d) plot of profile line marked in a) showing Pt(111) the height of the terraces. Tunneling parameters: a) $I_t = 100$ pA, $U = 1$ V, b) $I_t = 20$ nA, $U = 3$ mV.

clean Pt(111) surface reveals terraces with a step height of 226 ± 1 pm, which is in agreement with the $d(111)$ interplanar spacing of fcc Pt [33]. An atomic-resolution STM image showing the hexagonal atomic structure of Pt(111) with an interatomic distance of $a_{\text{Pt}(111)} = 277 \pm 1$ pm typical for Pt NND [146] is presented in Figure 6.1 b). The LEED pattern (Figure 6.1 c))

exhibits (1×1) reconstruction of pristine Pt(111). The LEED image is shown for $E_{\text{beam}} = 50$ eV, but the complete data set using a wide range of electron beam energy was recorded as a reference for surface alloys LEED analysis.

The electronic structure of the pure substrate was examined using PTS. The results are shown in Figure 6.2 a). The presented curves differ with the tip position on the bare Pt(111) substrate for PTS. Despite small variations, all of them exhibit a step state at 0.45 ± 0.05 eV, which is known as a surface state of Pt(111) [138]. Finally, the purity of the substrate was verified by AES. Figure 6.2 b) presents the AES derivative signal exhibiting typical Pt signals [106], as indicated in the graph.

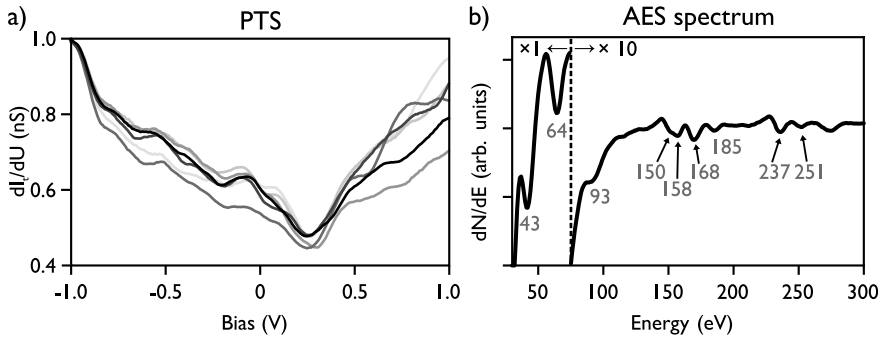


Figure 6.2: Pt(111) substrate – a) PTS plots showing Pt(111) surface state ($I_{\text{stab}} = 5$ nA, $U_{\text{stab}} = 1$ V, $U_{\text{mod}} = 50$ mV, $\omega_{\text{mod}} = 6667$ Hz); b) AES spectrum of pristine Pt(111) surface, with marked typical for Pt signals.

6.2 Surface alloys formation

There are two ways to grow surface alloys: by depositing REM on a substrate at RT and subsequent post-annealing, or by depositing it onto a substrate at an elevated temperature (known as reactive growth process). The latter is preferred because it avoids REM clustering and results in a more ordered structure of the surface alloys [6]. For that reason, the surface alloys presented within the dissertation were grown using a reactive growth process. Gd and Dy were evaporated from tungsten crucibles, using an e-beam evaporator and the background pressure during deposition did not exceed 1.0×10^{-10} mbar. Coverage (θ) of 1 L is assigned to the amount of deposited REM necessary to cover the sample surface completely with a 1 L of REM-Pt₂ alloy yielding 3.75 REM atoms per nm². This also corresponds to u.c. used in Subsection 3. The samples were kept at an elevated temperature for 5 – 15 minutes after deposition. The final structure of the surface alloys was observed to be independent of the post-annealing time. To ensure reproducible deposition conditions, the substrate temperature was controlled using two methods: an externally mounted pyrometer focused on the sample plate and the heating stage calibration based on a thermocouple readout. Although the accuracy of the thermocouple (0.05 K) and the pyrometer (0.1 K)

is high, the measurement uncertainty is about 5 K. This is due to the indirect temperature measurement. In the case of a thermocouple, the real measurement uncertainty will result from the quality of the thermal contact between the sample and the thermocouple. In the case of a pyrometer, the measurement relies on the recording of the sample plate's temperature based on the set emissivity, and additionally, the signal is transmitted through a vacuum window, which partially absorbs the signal and affects the value of the temperature readout.

Both growth methods require energy high enough to activate surface alloy formation. The range of temperatures for surface alloys growth was determined by analyzing temperature-dependent sample preparations. The same behavior was observed for both Gd- and Dy-Pt systems, they differed only in the temperature for which structural changes occurred. Figure 6.3 shows the evolution of the surface structures, based on the Dy-Pt system, depending on the temperature of the substrate in the process of reactive growth. When REM is deposited onto a clean Pt(111) substrate

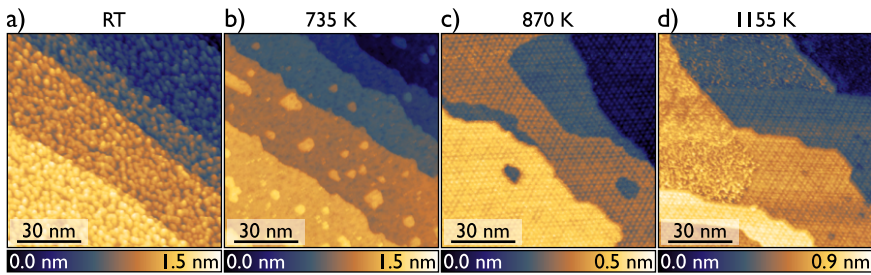


Figure 6.3: Thermal evolution of Dy-Pt surface structures – a) 0.7 L deposition on substrate with a RT; b) 0.7 L deposition on substrate with a temperature of 735 K; c) 1 L deposition on substrate with a temperature of 870 K; d) 1 L deposition on substrate with a temperature of 1155 K. Tunneling parameters: a) $I_t = 1.2$ nA, $U = 1.5$ V, b) $I_t = 0.6$ nA, $U = 1.5$ V, c) $I_t = 1.2$ nA, $U = 1.5$ V, d) $I_t = 1.7$ nA, $U = 1.3$ V.

at RT, it does not create ordered structures, as previously observed in the Ce-Pt system [59, 61]. Instead, REM demonstrates Volmer-Weber growth mode, forming irregular-shaped and randomly distributed clusters and islands with $(150 - 230) \pm 5$ pm apparent height (Figure 6.3 a)). When reactive growth occurs below the alloy-formation temperature, REM and Pt atoms intermix and form irregularly shaped islands with unknown stoichiometry (Figure 6.3 b)). Only when the alloy-formation activation temperature is reached, regardless of annealing time, the ordered structures of the surface alloys are formed (Figure 6.3 c)). The Gd-Pt system's alloy-formation activation temperature is approximately 750 ± 5 K, while the Dy-Pt system's temperature is about 780 ± 5 K. The Gd-Pt system's alloy-formation activation temperature is consistent with an earlier report by Ulrikkeholm *et al.* [48], who estimated the alloy formation temperature to be between 723 – 773 K for a 2-nm-thick Gd layer deposited on Pt(111). Detailed analysis of surface structures observed within the alloy formation temperature range and various REM coverages are presented in Subsection 6.3 for Gd-Pt and

Subsection 6.4 for Dy-Pt. It is known that Pt tends to form overlayers not only due to the electrochemical reactions [40] but also due to the annealing at the high temperature [38, 48]. When the temperature of the Dy-Pt system exceeds 1165 ± 5 K, samples get overheated, and Pt overlayers form (see Figure 6.3 d)). The temperature window for surface alloy growth is limited by the activation energy on the lower range and the formation of Pt overlayers on the upper range.

6.3 Gd-Pt system

Among the family of REMs, two elements with the highest magnetic moments and various magnetic properties were selected for the studies. The first element is *gadolinium*, which has the highest possible number of unpaired 4f electrons resulting in a very high magnetic moment of approximately $7.94 \mu_B$ [2, 147]. Gd is one of the four pure elements that exhibit ferromagnetic order above RT with its $T_C = 293$ K [147]. It is also the only heavy REM (the group from Europium to Luthenium) that goes directly from the paramagnetic to the ferromagnetic state without any rotational transition phase. Moreover, all REMs have magnetic anisotropy with an energy of the order of meV per atom, while Gd is an exception. Its anisotropy energy is two orders of magnitude smaller than other REMs, and it is comparable to the level of 3d transition metals' anisotropy [148]. Therefore, it may be assumed that the magnetic structure of Gd surface alloys will be affected only by the crystal field anisotropy and shape anisotropy. The indirect RKKY interactions are necessary to allow for the interactions between magnetic atoms of REM through the itinerant electrons of Pt. This type of interaction is even more complex than superexchange since the magnetization of orbitals occurs already within the atom. The magnetic f electrons of REM interact with REM d electrons causing their polarization. The d electrons of REM interact with d electrons of a different REM atom, or the interaction can be further mediated through d electrons of Pt.

6.3.1 Structural properties of Gd-Pt surface alloys

Within the temperature range from 590 K to 920 K and coverage range from submonolayer up to 2 L three ordered structures, presented in Figure 6.4 are observed. These structures are identified as single layer GdPt₂ (1 L GdPt₂), single layer GdPt₅ (1 L GdPt₅), double layer GdPt₅ (2 L GdPt₅). Part of the data presented within the Subsection, concerning structural and electronic properties supported by DFT calculations, were already published in [145].

The structural models of identified surface alloys are presented in Figure 6.4 a). Blue and gray spheres correspond to the Gd and Pt atoms, respectively. The distances between surface alloys' layers are magnified to present the structure, especially the termination layer more explicitly. 1 L GdPt₂ is formed by a Gd-Pt intermixed alloy layer laying on top of the substrate. The structure of the alloy layer is analogous to REM surface alloys with Au and Ag [6, 22, 28]. GdPt₂ lattice model is overlaid on

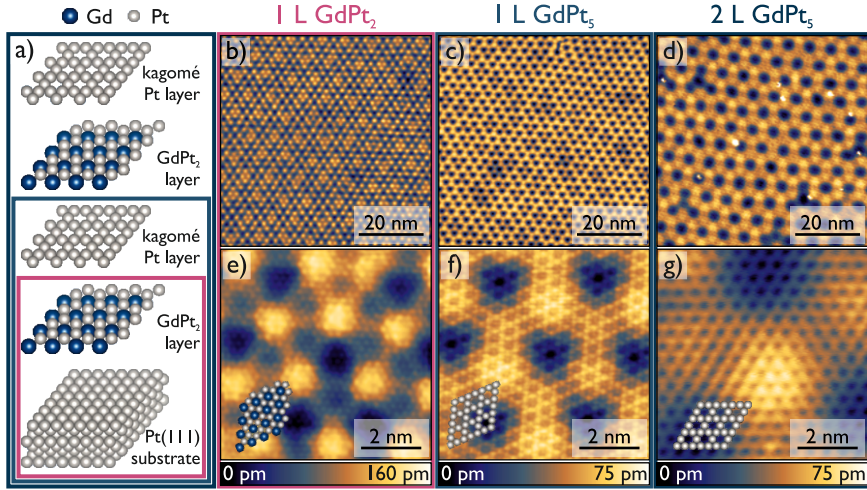


Figure 6.4: Gd-Pt surface alloys – a) structural models with alloy layers separated for clarity. The colors of the boxes' frames relate the atomic structure to the corresponding STM topography images. b) - d) Large-scale STM topography images of moiré patterns of 1 L GdPt₂, 1 L GdPt₅, and 2 L GdPt₅, respectively. e) - g) Zoom-in STM topography images with atomic resolution of the termination layer of each surface alloy. The models of the termination layers are overlaid on the STM images. Tunneling parameters: b) $I_t = 10$ nA, $U = 3$ V, c) $I_t = 1$ nA, $U = 1$ V, d) $I_t = 100$ pA, $U = 1.5$ V, e) $I_t = 50$ nA, $U = -1$ mV, f) $I_t = 100$ nA, $U = -1$ mV, g) $I_t = 100$ pA, $U = 35$ mV.

the atomic-resolution STM topography image (Figure 6.4 e)). The kagomé lattice, known from bulk GdPt₅ alloys [42], appears as a termination layer of 1 L GdPt₅ and 2 L GdPt₅. Kagomé lattice (Pt₃) consists of a net of triangles with atoms in their apex combined in such a way that each atom has four neighbors. Symmetry of the termination layers of 1 L GdPt₅ and 2 L GdPt₅ is confirmed by the atomic-resolution STM topography images (Figures 6.4 f) – g), respectively). Bulk GdPt₅ alloy consists of alternating intermixed GdPt₂ and pure Pt₃ layers. Similarly, in case of surface alloys, 1 L GdPt₅ is formed by GdPt₂ and Pt₃ layers, while 2 L GdPt₅ is double 1 L GdPt₅. DFT calculations have demonstrated that the GdPt₂ alloy layer laying directly on the Pt(111) substrate is energetically more favorable by 1.27 ± 0.01 eV compared to the system with a Pt kagomé lattice as an interface. All three surface alloys reveal long-range order (Figures 6.4 b) – d)) and short-range order (Figures 6.4 e) – g)). Numerous defects are observed in moiré patterns of all surface alloys (Figures 6.4 b) – d)), pointing to significant stress in the structure. Due to this, a clear determination of moiré patterns' unit cells is impossible. Atomically-resolved STM topography image of 1 L GdPt₂ (Figure 6.4 e)) reveals a hexagonal lattice with periodicity $a_{\text{NND-1LGdPt}_2} = 320 \pm 8$ pm corresponding to the NND of 1 L GdPt₂, that is the distance between nearest Gd-Pt or Pt-Pt atoms. Compared to the interatomic distance of pure Pt(111), which is $a_{\text{Pt}(111)} = 277$ pm, the expansion of the layer is observed. This is due to the difference in atomic radii of Pt and Gd, which is significantly larger for Gd (196 pm) than Pt (136 pm) [12, 149].

Larger Gd atoms expand the interatomic distance to fit within the lattice of Pt atoms. Gd atoms are also pushed out from the lattice plane as observed in the relaxed structural model. The lattice constant of 1 L GdPt₂, so the distance between nearest Gd atoms is equal to $a_{1\text{LGdPt}_2} = 555 \pm 14$ pm. The lattice constant of bulk GdPt₅ alloy is equal to 529 pm [43], while for few-nm-thick alloy layers it increases to 533 pm [48]. This points out that the thickness reduction results in an increased lattice constant, which is consistent with the value obtained for the surface alloy. The stress of the alloy structure, caused by the reduction of the lattice constant, leads to the formation of many dislocation lines and irregularities in the moiré pattern. Apparent corrugation, which is defined as the difference in height between the highest and lowest points in the moiré pattern, is reduced for 1 L GdPt₅ compared to the 1 L GdPt₂. To reduce the influence of electronic structure on the apparent corrugation, STM topography images taken with the same tunneling parameters were compared. Moiré pattern of 1 L GdPt₅ seems much more organized than in the case of 1 L GdPt₂, however, with a closer look, differences in the atomic structure on various top sites of moiré pattern are observed (see Figure 6.4 f)), thus pointing the incommensurability between alloy and substrate. Atomic-resolution STM topography image reveals kagomé lattice with periodicity $a_{\text{NND}-1\text{LGdPt}_5} = 269 \pm 4$ pm and unit cell size $a_{1\text{LGdPt}_5} = 537 \pm 4$ pm. Kagomé net periodicity is much smaller than typical Pt(111) interatomic distance [43] due to the vacancies in the structure. These vacancies also allow the Gd atoms from the layer beneath to fit in as they lay directly below the kagomé lattice vacancies. 2 L GdPt₅ demonstrates the most ordered moiré pattern among all three observed structures and apparent corrugation comparable to 1 L GdPt₅. Nevertheless, moiré pattern unit cell, cannot be determined straightforwardly from the obtained STM topography images. Atomic-resolution STM topography image shows that the 2 L GdPt₅ preserves the termination layer, which is the kagomé lattice with periodicity $a_{\text{NND}-2\text{LGdPt}_5} = 272 \pm 2$ pm. Atomic lattice unit cell size is $a_{2\text{LGdPt}_5} = 544 \pm 2$ pm points to a structure relaxation with an increasing number of atomic layers.

Figure 6.5 presents the structures of Gd-Pt surface alloys in reciprocal space. Well-defined diffraction patterns appear after surface alloying, pointing to the well-defined surface reconstruction that has been formed. LEED was used for experimental data while simulated spots' positions were extracted using the software LEEDLab [150]. Simulated patterns are reproduced using a Pt(111) as a reference. The calibration data were extracted from the fitting of the Pt(111) LEED pattern and further used for surface alloys structure reproduction. Simulated LEED patterns are overlaid on half of the experimental data. Dimensions from simulated patterns match well with real space surface dimensions determined from STM images. Experimental LEED patterns points that the signal from the Pt(111) substrate is visible for 1 L GdPt₂ (Figure 6.5 a)) marked with vectors $\mathbf{a}_1, \mathbf{a}_2$. Vectors $\mathbf{b}_1, \mathbf{b}_2$, forms (1.2996×1.2996) superstructure with respect to Pt(111). It corresponds to the NND distance in the alloy layer that has a larger lattice constant ($a_{\text{NND}-1\text{LGdPt}_2} = 320 \pm 8$ pm) than pure Pt(111) ($a_{\text{Pt}(111)} = 277$ pm). There

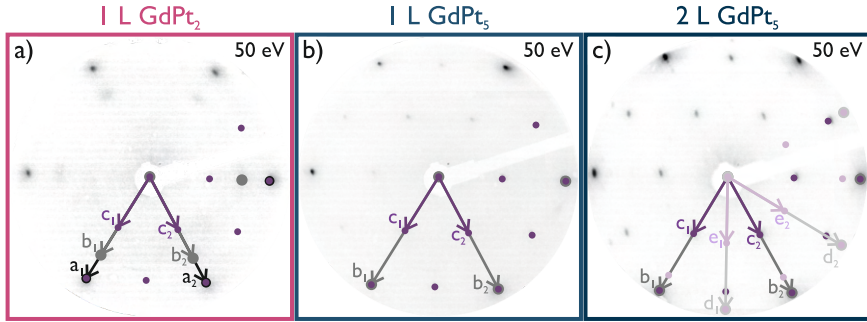


Figure 6.5: Gd-Pt surface alloys – experimental LEED diffraction images taken for electrons energy of 50 eV with simulated LEED patterns overlaid on the half of image of a) 1 L GdPt₂, b) 1 L GdPt₅, and c) 2 L GdPt₅. Black vectors ($\mathbf{a}_1, \mathbf{a}_2$) point Pt(111) structure. Gray vectors ($\mathbf{b}_1, \mathbf{b}_2$ and $\mathbf{d}_1, \mathbf{d}_2$) point the lattice of Pt atoms forming surface alloys, not rotated and rotated relative to the substrate, respectively. Purple vectors ($\mathbf{c}_1, \mathbf{c}_2$ and $\mathbf{e}_1, \mathbf{e}_2$) indicate the lattice formed by Gd atoms from alloy layers that are not rotated and rotated relative to the substrate, respectively.

is also a considerably weaker signal, marked with $\mathbf{c}_1, \mathbf{c}_2$ vectors, forming the (2.0036×2.0036) superstructure parallel to the first one. The vectors' length and the lack of rotation suggest that the latter superstructure corresponds to the distance between the nearest Gd atoms in the alloy layer. It is possible to distinguish the two lattices due to slight atoms' buckling occurring in 1 L GdPt₂ (see side view models in Figure 6.7). No rotation between the alloy layer and substrate Pt(111) is observed. Shadows around the spots may point out that the structure is not fully ordered or that the moiré pattern is very disordered. Compared with the STM data, the latter seems more likely, however, the resolution of LEED data does not allow for a clear explanation. Signal from the substrate Pt(111) vanishes already for 1 L GdPt₅ (Figure 6.5 b)). Only two superstructures, that are not rotated to each other, are observed in the LEED pattern of 1 L GdPt₅. The first one, described by $\mathbf{b}_1, \mathbf{b}_2$ vectors, has the higher intensity signal and forms (0.9711×0.9711) superstructure, demonstrating the lattice constant contraction with respect to the pure Pt(111). This lattice corresponds to the NND distance in the kagomé lattice. This is consistent with the STM observation of the termination layer. Second superstructure, described by $\mathbf{c}_1, \mathbf{c}_2$ vectors, appear as (1.9386×1.9386) superstructure regarding to Pt(111) substrate. Due to the vacancies in the kagomé lattice, and the structure buckling, that pushes up the Gd atoms from the alloy layer, LEED patterns also reveal the Gd-Gd lattice from the layer beneath. Contrary to the other surface alloys, 2 L GdPt₅ LEED pattern reveals the coexistence of two rotated domains of superstructures similar to the one observed for 1 L GdPt₅. Rotated domains coexistence was already observed before for Ce-Pt thin film alloys [59, 61–63] as well as Gd-Pt surface structures [48]. The exact determination of rotational domains requires more statistics from LEED experiments on numerous samples. However, following Ulrikkeholm *et al.*, who in half of the cases observed the structure rotated and in the other half not rotated [48],

this suggests that both configurations are energetically equivalent or at least very close. Both domains consist of two superstructures with the same lattice constants that differ only with the rotation angle. Not rotated domain consists of (0.9819×0.9819) and (1.9639×1.9639) (marked with dark gray vectors $\mathbf{b}_1, \mathbf{b}_2$ and dark purple $\mathbf{c}_1, \mathbf{c}_2$ vectors) while rotated domain has $(0.9819 \times 0.9819)R30^\circ$ and $(1.9639 \times 1.9639)R30^\circ$ superstructures (marked with light gray $\mathbf{d}_1, \mathbf{d}_2$ and light purple $\mathbf{e}_1, \mathbf{e}_2$ vectors). The rotation angle is around $30 \pm 3^\circ$. A more accurate angle is not possible to determine due to the resolution of LEED images. Moiré pattern fingerprints are observed for both 1 L GdPt₅ and 2 L GdPt₅, with more pronounced signals in the latter. In general, the spots from the moiré pattern are observed around zero-spot. However, they are also reproduced around the spots of the superstructure described by $\mathbf{b}_1, \mathbf{b}_2$ vectors. In 1 L GdPt₅ they appear as a shadow around without any pronounced spots. This confirms the structural analysis based on STM topography images, where the moiré pattern could not be clearly defined due to the complicated and disordered structure of the moiré pattern and its large unit cell. Satellites are more pronounced in 2 L GdPt₅, although their pattern is still very weak confirming the STM data analysis, where the determination of moiré patterns was not possible.

Summarizing, the Gd-Pt system's surface alloys adopt two types of structures: GdPt₂ (1 L GdPt₂), and GdPt₅ (1 L GdPt₅ and 2 L GdPt₅). The first one is terminated with hexagonal symmetry Gd-Pt mixed layer, while the other two are the combination of alternating Gd-Pt mixed layers and kagomé symmetry pure Pt layers with the latter as a termination layer. All of them exhibit long-range (moiré pattern) and short-range (atomic) ordered structures. Due to the significant stress in the structure, they differ with apparent corrugations and unit cell and moiré pattern periodicity dimensions.

6.3.2 Electronic properties of Gd-Pt surface alloys

To study the electronic properties of surface alloys experimental data of LTS were compared with DFT calculations. The influence of the moiré pattern on electronic properties was confirmed by LTS, as shown in Figure 6.6. The LTS measurements were taken along arrows marked on STM topography images, with 20 points at a constant separation distance chosen for each line. Although the observed features slightly vary in intensity, the main features remain consistent. These variations are due to the varying hybridization of the surface alloy with the substrate, resulting in weakened or strengthened electronic states.

Structural models' relaxation confirmed that 1 L GdPt₂ is the most strained among all three surface alloys, proving the interpretation of STM topography images. Side views of relaxed models are shown in Figure 6.7. Gd atoms are pushed up from the plane of Pt atoms in the alloy layer, by Pt atoms laying in the layer beneath. The same is the case for 1 L GdPt₅ and 2 L GdPt₅. The calculated DOS of termination layers for all three surface

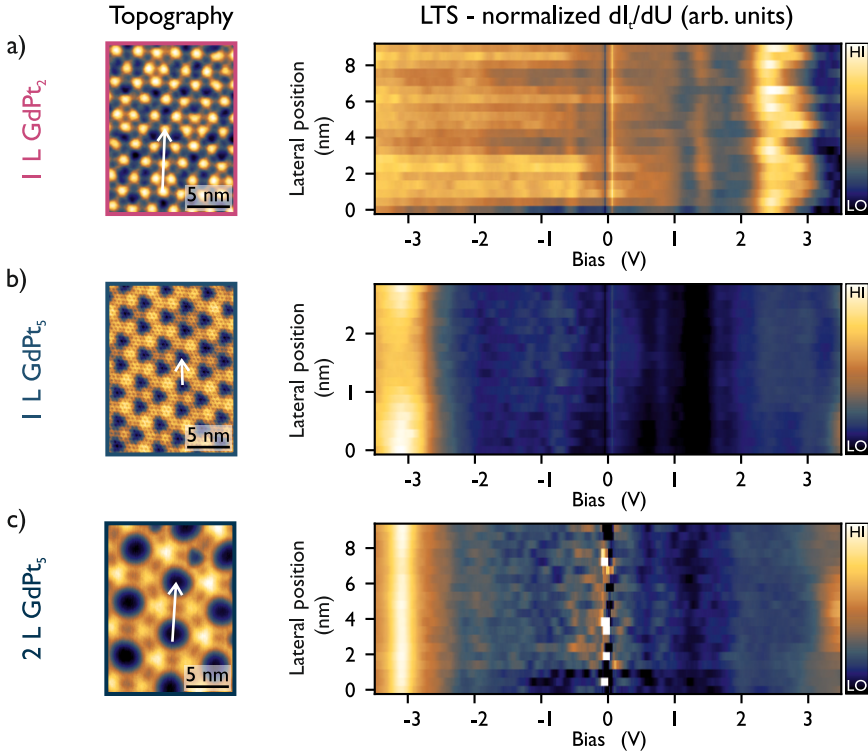


Figure 6.6: Gd-Pt surface alloys – LTS and STM topography images with marked LTS position of a) 1 L GdPt₂, b) 1 L GdPt₅, and c) 2 L GdPt₅. Tunneling parameters: a) $I_{\text{stab}} = 10$ nA, $U_{\text{stab}} = 3.5$ V, $U_{\text{mod}} = 50$ mV, $\omega_{\text{mod}} = 6667$ Hz, b) $I_{\text{stab}} = 5$ nA, $U_{\text{stab}} = 3.5$ V, $U_{\text{mod}} = 50$ mV, $\omega_{\text{mod}} = 6667$ Hz, c) $I_{\text{stab}} = 10$ nA, $U_{\text{stab}} = 2$ V, $U_{\text{mod}} = 50$ mV, $\omega_{\text{mod}} = 6667$ Hz.

alloys are compared with the experimental data in Figure 6.7. The calculations reproduced well the spectroscopic features but underestimated their energy. The unoccupied states are shifted towards E_F for 1 L GdPt₂, while the occupied states are closer to E_F for 1 L GdPt₅ and 2 L GdPt₅ compared to the experiment. These results confirm the previous interpretation based on STM topography images of the termination layer. The presented DOS results from the summation of the states of all atoms' residing in the termination layer and, in the case of 1 L GdPt₅ and 2 L GdPt₅, in the first intermixed alloy layer. The PDOS separately showing the states of Pt and Gd atoms for each of the alloys are shown in Figure 6.8.

The experimental and theoretical data of 1 L GdPt₂ show distinct features only in unoccupied states. The most pronounced peaks observed in the experiment, located at 2.50 ± 0.05 V and 1.45 ± 0.05 V originate from Gd, which is exposed in this layer. In the experiment, the 4f states have a sharp drop off into the vacuum, thus the most likely observed signals are the combination of 5d and 6s states. The intensity of these two peaks differs in the experiment, and it is unclear why. No significant feature is observed in

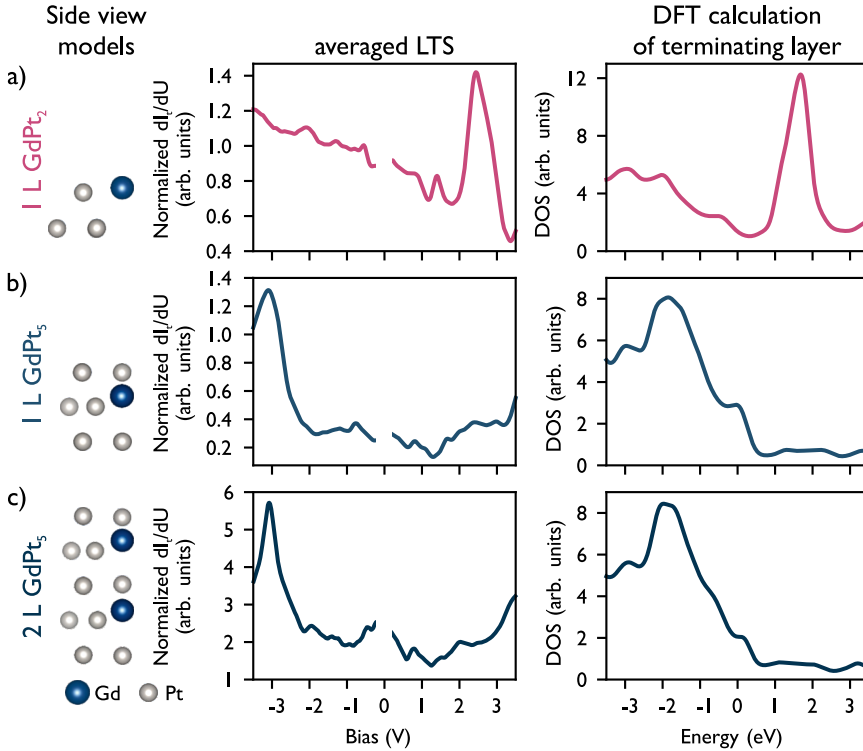


Figure 6.7: Gd-Pt surface alloys – relaxed models, averaged LTS spectra from Figure 6.6, and DFT calculation of a) 1 L GdPt₂, b) 1 L GdPt₅, and c) 2 L GdPt₅.

the unoccupied states. Instead, a slow increase in signal is observed, which may be attributed to the combination of Pt and Gd states. For 1 L GdPt₅ and 2 L GdPt₅, where the termination layer is formed solely by Pt atoms, the intensity of Gd signals is attenuated only to small features in unoccupied states, thus the dominance of Pt signals is expected. In experimental data, the highest intensity feature is observed in occupied states at around -3.10 ± 0.05 V for both, 1 L GdPt₅ and 2 L GdPt₅, and this state is merged with the one observed at -2.65 ± 0.05 V. At the same time, in the calculated DOS these bands are shifted toward the E_F by 1.30 ± 0.05 V. The observed states are most probably the combination of 5d and 6s bands of Pt. The STM topography images of samples, where all three surface alloys coexist, revealed that the impurities prefer absorption on 1 L GdPt₂ over 1 L GdPt₅ or 2 L GdPt₅, indicating the higher reactivity of the surface alloy terminated with intermixed GdPt₂ layer compared to the one terminated with kagomé Pt layer. The same was reported for the Ce-Pt system, indicating a higher chemical reactivity of the uncovered CePt₂ layer [65].

The electronic properties of the investigated surface alloys show significant differences depending on the termination layer. In addition, the moiré pattern also affects the electronic structure, namely, it causes a change in the

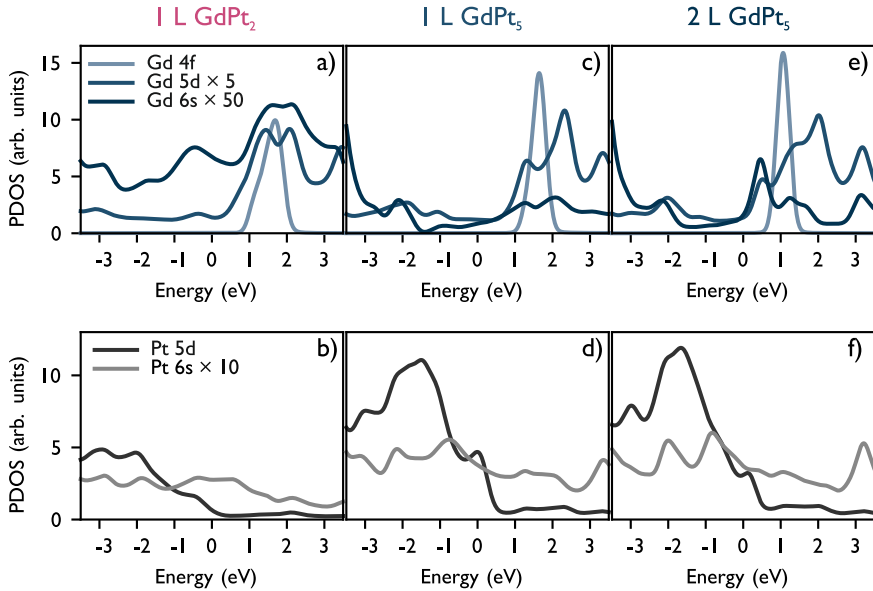


Figure 6.8: Gd-Pt surface alloys – PDOS of a) 1 L GdPt₂, b) 1 L GdPt₅, and c) 2 L GdPt₅. The top row presents Gd 4f, 5d, and 6s states, while the bottom row 5d and 6s states of Pt.

hybridization of the substrate with the surface alloy, which, together with the modulation of the moiré structure, modulates the intensity of electronic states. Depending on the termination layer, the surface alloys also exhibit varying reactivity.

6.3.3 Gd-Pt surface alloys phase diagram

A variety of samples were analyzed to understand how the surface structures are affected by temperature and coverage. The results showed that two factors determine the contribution to surface area occupancy: the initial surface coverage with Gd and substrate temperature during the reactive growth process. To preserve the most constant level of Gd diffusion into the bulk for coverage-dependent analysis, only the deposition rate was increased while the deposition time was kept. STM is a local technique thus to collect reliable statistics, the macroscopic position of the sample was changed at least three times. Numerous large-scale STM topography images were collected with a total area of at least $1.5 \mu\text{m}^2$. When the initial Gd coverage is below 0.5 L, 1 L GdPt₂ and 1 L GdPt₅ coexist with disordered Gd-Pt clusters. In the lowest of investigated initial Gd coverage, *i.e.* 0.2 L, when the substrate temperature exceeds 900 K alloy growth is hampered. Above that temperature, Gd atoms diffuse to the bulk, and Pt atoms form Pt overlayers on top of the surface. This results in low Gd concentration in the surface regime and only Gd-Pt clusters and islands with unknown stoichiometry are formed on the surface. At an initial Gd coverage of 0.5 L the area occupancy

of 1 L GdPt₂ and 1 L GdPt₅ increases. The sample morphology is strongly dependent on the location of the probe on the sample, and there is no clear temperature dependency observed in the range from 865 K to 926 K. Only for Gd coverage above 0.75 L, there is significant temperature dependence observed. Statistics data for Gd coverage 0.75 L, 1.5 L, and 2 L and temperature in the range from 865 K to 926 K are presented in Figure 6.9. Submonolayer Gd coverage reveals the largest number of various structures observed, including Gd-Pt clusters, and all three surface alloys. Unordered Gd-Pt clusters are observed only up to 880 K. The highest reached area occupancy of 1 L GdPt₂ (65 %) is observed for 880 ± 5 K. With increasing temperature, the contribution from Gd-Pt clusters and 1 L GdPt₂ decreases, while the input from 1 L GdPt₅ increases. Additional thermal energy provided at increased temperature enhances Pt atoms' mobility, which allows for the formation of Pt overlayers [38, 42, 48]. Pt atoms form a kagomé overlayer on top of 1 L GdPt₂, transforming it into 1 L GdPt₅. With the temperature increase the area occupied by 2 L GdPt₅ is reduced at the expense of 1 L GdPt₅, tending to the unification of the surface. Samples with Gd coverage above 1.5 L are solely covered with surface alloys within the investigated temperature range. For 1.5 L Gd coverage, 2 L GdPt₅ covers about 65 % of the surface area, while 1 L GdPt₂ and 1 L GdPt₅ occupy the remaining part of the surface. There is no clear temperature dependence in the area share of these two surface alloys, but in general, the surface is dominated by 1 L GdPt₂. Coverage above 1.5 L leads to the 2 L GdPt₅ dominance on the level of 90 % surface area occupancy.

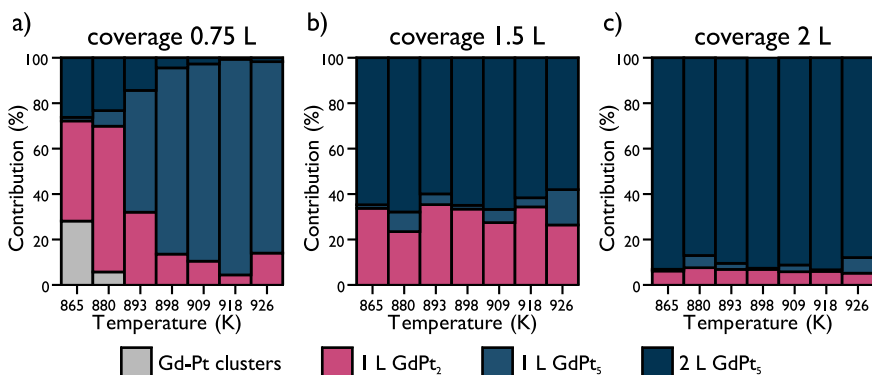


Figure 6.9: Gd-Pt surface alloys – area occupancy graphs as a function of substrate temperature in range 865 – 926 K, and Gd coverage a) 0.75 L, b) 1.5 L, and c) 2 L.

The fraction of surface coverage for each of these structures can be controlled by the sample preparation parameters (coverage and temperature). Using the presented simplified phase diagrams, it is possible to determine the conditions for preparing a sample with specific coverage. It is possible to prepare homogeneous samples almost exclusively covered with 1 L GdPt₅, 2 L GdPt₅. Sample dominated by 1 L GdPt₂ may also be prepared, but the highest possible coverage is then 65 %.

6.3.4 Magnetic properties of Gd-Pt surface alloys

XMCD measurements of the Gd-Pt system were conducted at the ALBA Synchrotron's BL-29 Boreas beamline in collaboration with ALBA staff. The measurements were carried out using a 90 % circularly polarized light from a helical undulator and registered using TEY mode [136]. The sample was kept at the lowest possible temperature of 4 K throughout all measurements, except for temperature-dependent measurements where the temperature was increased in small steps determined by the beamline temperature calibration. For Gd investigation, the $M_{4,5}$ absorption edges were taken. In the XMCD measurements, the samples were magnetized with a magnetic field $\mu_0 H = -6$ T. The XMCD spectra were obtained by calculating the difference between XAS signals registered for right (μ_-) and left (μ_+) circularly polarized light. Prior to the calculation, the XAS signals were normalized over the ring current, registered during the measurement. The background signal from Pt was subtracted. Although the step signal registered in the spectra is small compared to the XAS intensity, the Shirley function was calculated and subtracted from each XAS spectrum to reduce the error input to the sum rules calculations. Finally, to compare results for various samples, the XMCD signal was normalized over the maximum averaged XAS signal for a given sample. XMCD hysteresis loops were measured for two photon energies – one that matches with the maximum of the XMCD signal of the M_5 absorption edge and the other, which corresponds to the energy prior to the absorption edge (called pre-edge) where there is no XMCD signal. The electrons are affected by the magnetic field thus the normalization of the resonant energy signal over the non-resonant energy signal reduces the uncertainty [116]. The signals for both energies were recorded alternately while the magnetic field was successively sweeping from -6 T to 6 T and back. Such loops were measured for both light polarizations. For normalization purposes, the edge signal is divided over the pre-edge signal, and then the signals for both polarizations are subtracted and divided over their sum ($\frac{C^- - C^+}{C^- + C^+}$). Measurements were conducted in two configurations, as shown in Figure 4.14. At normal incidence ($\alpha = 0^\circ$), the magnetic field is also normal to the sample's surface, giving an out-of-plane contrast. While for grazing incidence (in this experiment $\alpha = 70^\circ$), the magnetic field is nearly parallel to the sample's surface, giving the in-plane contrast. The in-plane signal will be affected by the additional out-of-plane component due to the setup geometry. It is not possible to align the incident beam parallel to the sample surface, and thus the pure in-plane contrast is not reachable. Samples were prepared *on-site* according to the procedure described in Subsection 6.2. For this purpose, the preparation chamber at the endstation was involved. Prior to the experiment, the structure of the sample was verified using LEED to check if the sample was correctly reproduced. Further, the sample was transferred *in situ* to the cryostat where after reaching measurements conditions the XMCD experiment took place.

The absorption spectra at the Gd $M_{4,5}$ absorption edges of 1 L GdPt₅ and 2 L GdPt₅ are presented in Figures 6.10 a) and b), respectively. The

incident light polarization is indicated by color, where red represents negative polarization, blue represents positive polarization, and gray indicates an average absorption signal. The presented spectra are normalized according to the procedure described above. The intensity difference for absorption edges is clearly visible for both surface alloys, reaching the maximum at M_5 edge. The normalized XMCD signals for normal (navy) and grazing (yellow) configurations are presented in Figures 6.10 c) and d) for 1 L GdPt₅ and 2 L GdPt₅, respectively. The dichroism is explicitly observed for normal and grazing configurations of both surface alloys. The photon energies corresponding to the absorption edges are the same within the energy accuracy for both surface alloys, regardless of the beam – sample configuration. Obtained M_5 absorption edge energy stands at 1185.1 ± 0.1 eV, while the M_4 absorption edge is split into two maxima as observed before [151] with energies 1214.3 ± 0.1 eV and 1215.9 ± 0.1 eV. The tabulated electron binding energies of M_5 and M_4 edges are 1189.6 eV and 1221.9 eV, respectively [113, 152]. The observed energy difference of the order 5 eV between experimental and tabulated data results from chemical shifts. Atoms with a higher level of oxidation have higher binding energy because the reduction of electrons number in an atom makes its overall charge more positive, and thus, the removal of another electron requires higher energy. Conversely, in NEXAFS the higher oxidation state, the energy of absorption edge decreases [153].

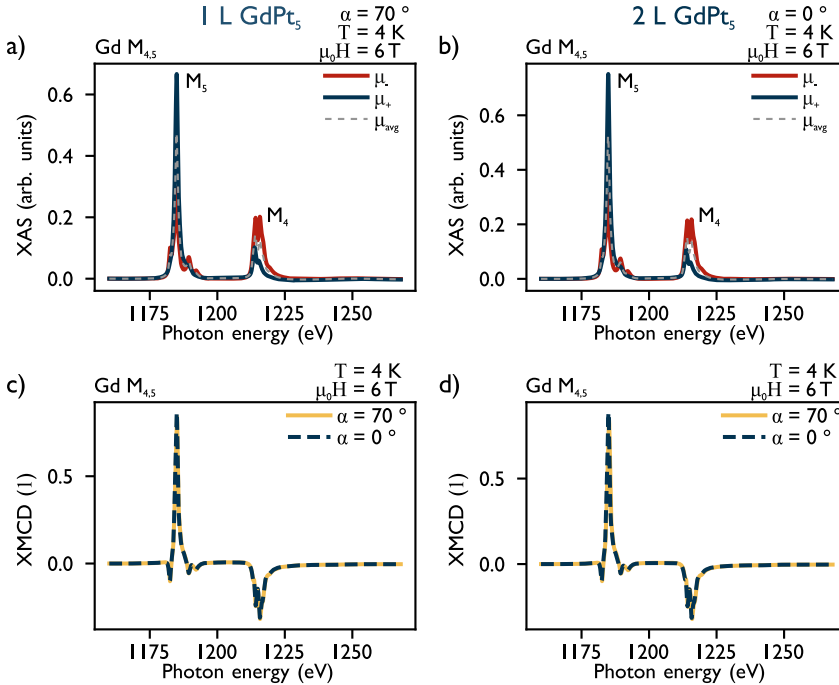


Figure 6.10: Gd-Pt surface alloys – a) 1 L GdPt₅ XAS spectra taken with grazing incidence of the x-ray beam, b) 2 L GdPt₅ XAS spectra taken with normal incidence of the x-ray beam, c) and d) XMCD spectra for grazing and normal incidence of the x-ray beam for 1 L GdPt₅ and 2 L GdPt₅, respectively.

Using sum rules, described in Subsection 4.4.2, the expected values of spin $\langle S_Z \rangle$ and orbital $\langle L_Z \rangle$ moments projections along the photon beam direction were calculated. Magnetic dipole operator value for Gd was assumed as 0, following Teramura *et al.* [154] and the number of holes as 7. Using the dependencies [155]:

$$\begin{aligned} m_l &= -\langle L_Z \rangle \mu_B, \\ m_s &= -2 \langle S_Z \rangle \mu_B. \end{aligned} \quad (6.1)$$

orbital magnetic moment (m_l) and spin magnetic moment (m_s) in units of μ_B (Bohr magneton) were calculated. Orbital magnetic moments reach $m_{l-1\text{LGdPt}_5} = -0.03 \pm 0.01 \mu_B$ and $m_{l-2\text{LGdPt}_5} = 0.15 \pm 0.01 \mu_B$. The orbital angular moment is required to observe magnetic anisotropy [156], thus for Gd, which has no inherent magnetic anisotropy a nearly zero value of the orbital moment is expected. This also explains the lack of a distinct difference in the intensity of XMCD between signals registered for grazing and normal configurations. Calculated spin magnetic moments amount to $m_{s-1\text{LGdPt}_5} = 5.82 \pm 0.01 \mu_B$ and $m_{s-2\text{LGdPt}_5} = 5.97 \pm 0.01 \mu_B$. The values are lower than the pure Gd ($7.94 \mu_B$ [147]) or simulated for Gd^{3+} ion ($-6.94 \mu_B$ [157]). The reduction of m_s value arises from the charge transfer between the Gd atoms and the Pt atoms which are involved in surface alloy formation.

Table 6.1 lists the spin magnetic moments of all three Gd-Pt surface alloys resulting from DFT calculations. The first column points out the layers of surface alloys and the top two substrate layers (analogously to layers in Figure 6.4 a)). These values are closer to the one for pure Gd.

Table 6.1: Gd-Pt surface alloys – Calculated magnetic moments. Layers in the first column are ordered analogously to layers in Figure 6.4 a).

Layer	Atom	1L GdPt ₂ (μ_B)	1L GdPt ₅ (μ_B)	2L GdPt ₅ (μ_B)
Pt kagomé	Pt	-	-	0.01
	GdPt ₂	-	-	0.09
GdPt ₂	Gd	-	-	7.62
	Pt kagomé	Pt	-	0.10
	Pt	0.03	0.12	0.06
GdPt ₂	Gd	7.64	7.58	7.61
	substrate 1 st layer	Pt	0.10	0.09
substrate 2 nd layer	Pt	0.05	0.02	0.02

Since the Gd atoms in surface alloys are bounded with Pt atoms, it can be assumed that DFT underestimates the charge transfer. Nevertheless, the calculations confirm the polarization of Pt atoms due to the charge transfer from Gd atoms. Pt atoms in the alloy layer of 1 L GdPt₂ have the smallest of induced magnetic moments over the three considered alloys. In 1 L GdPt₅ and 2 L GdPt₅, all Pt atoms surrounding the Gd atoms are also polarized and their magnetic moments reach 0.06 – 0.12 μ_B . The Pt atoms of the

substrate layers are also polarized, but the interaction range is very short. A sharp drop of the magnetic moments is observed towards the bulk of the substrate. The reduction is more significant for GdPt₅ surface alloys than 1 L GdPt₂.

Figures 6.11 a) and b) shows magnetization curves of normal (navy) and grazing (yellow) incidence for 1 L GdPt₅ and 2 L GdPt₅ surface alloys. These curves show normalized magnetization at a fixed energy as a function of the applied magnetic field $\mu_0 H$. The photon energies of edge and pre-edge were extracted from XMCD spectra taken for the highest possible magnetic field of 6 T. The magnetization curves were normalized over the highest magnetization value of a given range. For 1 L GdPt₅, the out-of-plane mag-

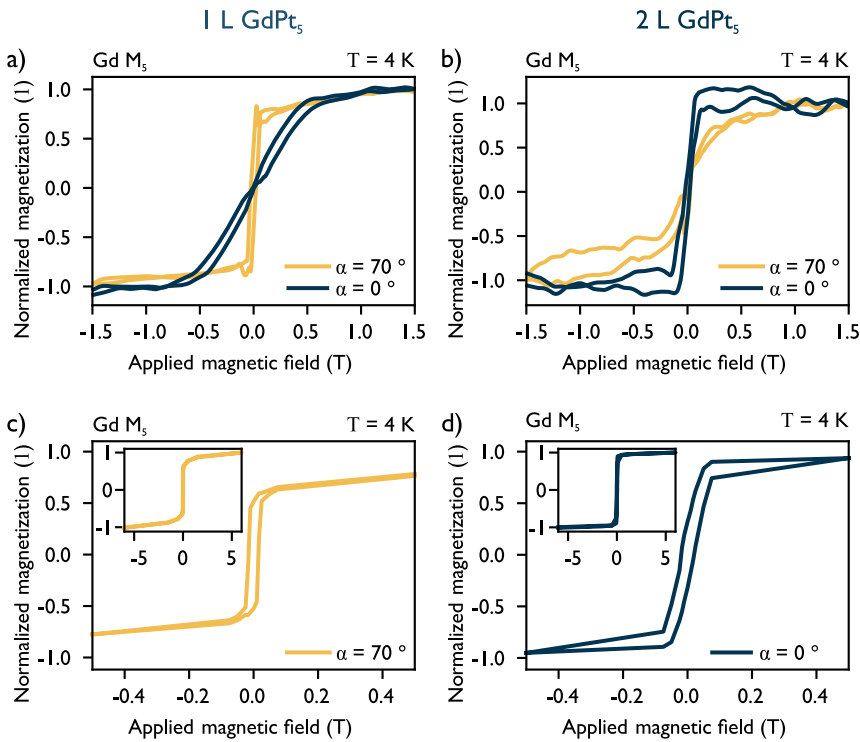


Figure 6.11: Gd-Pt surface alloys – a) and b) hysteresis loops registered for normal and grazing incidence angles for 1 L GdPt₅ and 2 L GdPt₅, c) and d) limited range hysteresis loops extracted from magnetic field-dependent XMCD measurements for 1 L GdPt₅ and 2 L GdPt₅, respectively.

netization curve with the field applied perpendicular to the surface saturates at approximately 1 T, while the in-plane magnetization curve reaches saturation at a lower magnetic field of 0.15 T. The hysteresis loop of the grazing incidence shows a step-like shape, indicating that the 1 L GdPt₅ surface alloy exposes ferromagnetic order with an in-plane easy magnetization axis. The magnetization curves of 2 L GdPt₅ in Figure 6.11 b) reveal the opposite behavior. The step-like shape is observed for the normal incidence magne-

tization curve, pointing to the out-of-plane as an easy magnetization axis. In-plane magnetization loop saturates around 1 T, while the out-of-plane saturates at 0.3 T, in contrast to the 1 L GdPt₅. A higher saturation field the hysteresis taken for an easy magnetization axis points out the 2 L GdPt₅ to be a harder magnetic material than 1 L GdPt₅. The different easy magnetization axes of 1 L GdPt₅ and 2 L GdPt₅ are most likely caused by varying crystal field interactions. In 1 L GdPt₅ the kagomé layer is only present above the intermixed alloys layer, whereas below is a hexagonal Pt layer from the substrate. In contrast, in 2 L GdPt₅, there is a kagomé layer both above and below the intermixed layer, causing the Gd atoms in the two alloys to be in different environments and thus affected by different crystal fields. The in-plane arrangement indicates a strong interaction between the Gd atoms located in the same plane. In the second case, the presence of the kagomé layer under the intermixed alloy layer causes the interaction between the Gd atoms of different layers, which are separated by kagomé lattice vacancies, to be stronger than between the Gd atoms of the same layer. The coercivity of both surface alloys is lower than the accuracy of the magnetic field affected by the artifact around 0 T. Using the fact that the XMCD signal is proportional to the projection of the magnetization M in the direction of the applied magnetic field, the XMCD spectra for various magnetic fields were recorded to reproduce the hysteresis loop without the artifact [116]. Figures 6.11 c) and d) show the normalized magnetizations extracted from XMCD data as a function of the applied magnetic field. Insets in Figures 6.11 c) and d) show hysteresis loops with full range magnetic field taken up to 6 T. The curves' shapes reveal that they are not entirely saturated even with the highest possible magnetic field, most likely due to the fact that the measurement was made at a temperature close to T_C . The signal of the curve is slowly increasing up to the maximum magnetic field. This effect is particularly visible for 1 L GdPt₅. This also explains the fact that the signal does not reach unity in a limited range of hysteresis loops shown in Figures 6.11 c) and d). The coercivity of 1 L GdPt₅ is $H_{C-1L\text{GdPt}_5} = 15 \pm 2$ mT, while for 2 L GdPt₅ is slightly higher and amounts $H_{C-2L\text{GdPt}_5} = 20 \pm 2$ mT. The values are comparable to the order of the local coercive field obtained for GdAu₂ by the spin-polarized STM method (17.5 mT [8]). However, they are an order of magnitude higher than the coercivity obtained from the magneto-optical Kerr effect for GdAu₂ (0.2 mT) and GdAg₂ (0.1 mT) [28].

The Curie temperatures of both surface alloys were obtained by using temperature-dependent XMCD to extract the remanences. The results are presented in Figures 6.12 a) and b) for a temperature range of up to 16 K. Measurements at temperatures below 4 K were not possible due to experimental setup limitations. The dependence of magnetization on the temperature below T_C follow the dependence [158]:

$$|m| = \sqrt{\frac{a}{2bT_C}}(T_C - T)^{1/2}, \quad (6.2)$$

where a and b are constants, and m is a parameter proportional to the mag-

netization. The gray dashed lines indicate the cut-off lines and any points below this line were omitted from the fitting process due to low values in the noise range. The gray lines represent the fitting of the data to Equation 6.2, which agrees well with the experimental data. For 1 L GdPt₅ and 2 L GdPt₅,

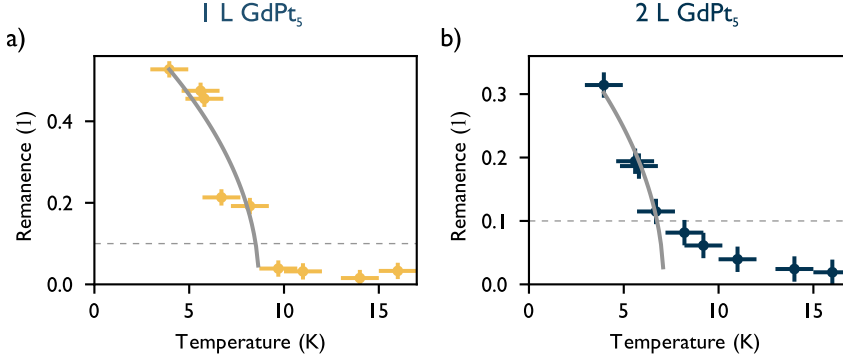


Figure 6.12: Gd-Pt surface alloys – graphs of the temperature dependence of normalized remanence for a) 1 L GdPt₅ and b) 2 L GdPt₅.

the T_C values were obtained as one of the parameters of the fitted equation and they are 9 ± 1 K and 7 ± 1 K, respectively. Bulk GdPt₅ alloy, is also ferromagnetic but its T_C is 13.9 K [57]. The values for surface alloys are significantly lower than the T_C of pure Gd (293 K [147]) and twice lower than the T_C of GdAu₂ surface alloy [32]. Although the shape of the hysteresis curves in a wide magnetic field range (insets of Figures 6.11 c) and d)) suggests that the temperature is lower for 1 L GdPt₅ (the signal increase is more pronounced than in 2 L GdPt₅ hysteresis curve), the closer look at the remanence in the base measurement temperature is higher for 1 L GdPt₅ than for 2 L GdPt₅, confirming the above findings.

Both surface alloys are ferromagnetic materials with very low T_C of a few Kelvins, which turned out to be lower than bulk alloy. The orbital magnetic moments calculated from experimental results are close to 0, confirming the lack of inherent magnetic anisotropy of Gd. The spin magnetic moments are lower than for pure Gd or Gd³⁺ ions due to the charge transfer effect and polarization of Pt atoms. DFT calculated magnetic moments suggest that the Pt atoms of the alloys' layers and the top two substrate layers are affected by the magnetism of Gd atoms. The difference is observed in the easy magnetization axes, which are in-plane for 1 L GdPt₅ and out-of-plane for 2 L GdPt₅.

6.4 Dy-Pt system

Dysprosium is the second REM chosen for surface alloys investigation. Similar to Gd, it has a high magnetic moment of $10.65 \mu_B$ [2, 147], which is the highest of any naturally occurring element. At the same time, its magnetic structure order is more complex than Gd. Dy has a Néel temperature

$T_N = 178.5 - 179$ K and $T_C = 85 - 89$ K [2, 147]. Ferromagnetic order shows an axial anisotropy with magnetic moments confined to the basal plane [2]. Between T_C and T_N Dy exhibits a transitional order, frequently observed for REMs, with a helical anti-ferromagnetic arrangement. The magnetization vector is rotating from layer to layer along the hexagonal c -axis, forming a spin spiral, also called a screw-type structure. The rotation angle strongly depends on the temperature [2]. By comparing Gd- and Dy-based systems, the contribution of shape anisotropy and magnetocrystalline anisotropy on the magnetic order structure of surface alloys can be determined. The competition between indirect RKKY interactions and direct Heisenberg-type interactions is observed when magnetic anisotropy occurs, giving rise to complex and unusual non-collinear magnetic structures.

6.4.1 Chemical composition and structural properties of Dy-Pt surface alloys

The chemical composition of 1 L DyPt₂ was confirmed using AES. The spectrum in the energy range of 90 eV to 175 eV showed all the characteristic peaks for both species [106] (see Figure 6.13). The peaks were marked with arrows on the spectrum, with pink color representing the signal from Dy and gray representing the signal from Pt.

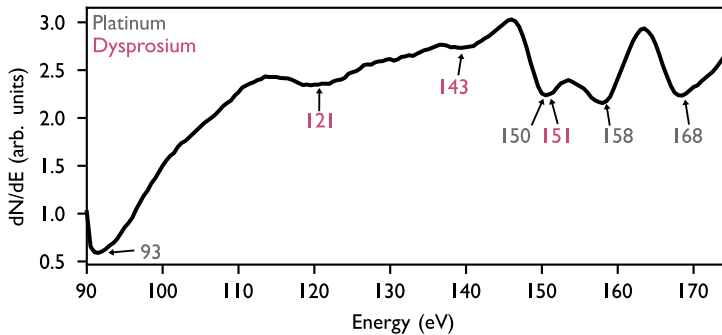


Figure 6.13: Dy-Pt surface alloys – AES spectrum in energy range from 90 eV to 175 eV of 1 L DyPt₂.

Dy-Pt surface alloys were investigated using reactive growth with temperatures ranging from 715 K to 1125 K and coverage ranging from submonolayer to about 7 layers. Within the investigated preparation conditions, the Dy-Pt clusters and only DyPt₂-type surface alloy and its multilayers were observed. Based on STM topography images, electronic properties, and dependence between growth conditions and surface area occupancy, two main cases were distinguished: single layer DyPt₂ (1 L DyPt₂) and triple layer DyPt₂ (3 L DyPt₂).

Along with other REM-NM surface alloys [7, 8, 22–24, 27] 1 L DyPt₂ and 3 L DyPt₂ reveal long-range moiré pattern presented in Fig-

ures 6.14 a) and b), respectively. Due to the very similar structure of the termination layers, distinguishing between 1 L DyPt₂ and 3 L DyPt₂ on an atomic scale is very challenging. The difference is most clearly seen in large-scale STM topography images exposing their moiré patterns. The one observed for 1 L DyPt₂ closely resembles a moiré pattern of 1 L GdPt₂ (compare with Figure 6.4 b)). The structure of the moiré pattern is non-

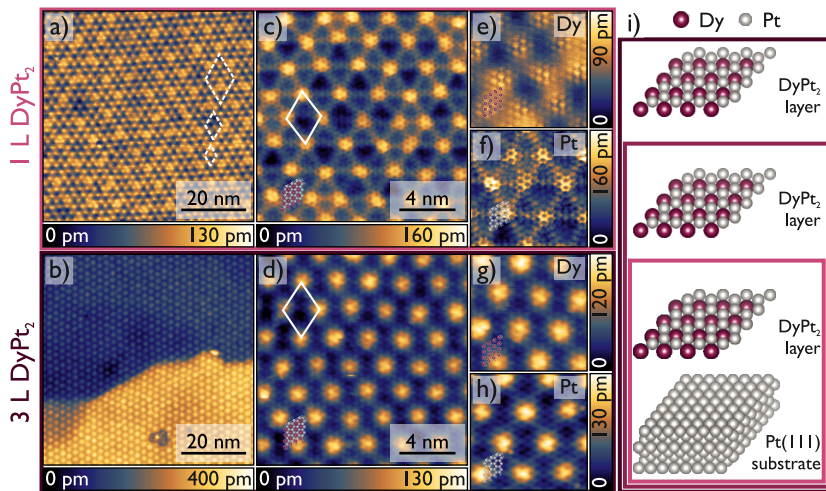


Figure 6.14: Dy-Pt surface alloys – a) – b) Large-scale STM topography images of moiré patterns of 1 L DyPt₂ and 3 L DyPt₂, respectively. c) – d) Zoom-in STM topography images with an atomic resolution of the termination layer of each surface alloy. The model of the termination layer is overlaid on the STM images. e) – f) and g) – h) Magnified atomic-resolution STM topography images of 1 L DyPt₂ and 3 L DyPt₂, respectively, exposing two contrasts: Dy and Pt atoms nets, respectively. The nets are overlaid on the STM images. i) Structural models with alloy layers separated for clarity. The colors of the boxes relate the atomic structure to the corresponding STM topography images. Tunneling parameters: a) $I_t = 1$ nA, $U = 2$ V, b) $I_t = 0.5$ nA, $U = -2$ V, c) $I_t = 5$ nA, $U = 10$ mV, d) $I_t = 10$ nA, $U = 3$ V, e) $I_t = 1.5$ nA, $U = 2$ V, f) $I_t = 5$ nA, $U = 2$ mV, g) $I_t = 10$ nA, $U = 3$ V, h) $I_t = 5$ nA, $U = 3$ V.

uniform and contains numerous defects and inhomogeneities, indicating the structure is stressed. For this reason, the determination of the exact unit cell based on the STM topography image is not possible. The most noticeable difference between 1 L DyPt₂ and 3 L DyPt₂ moiré patterns is the vanishing of the dislocation lines in the case of 3 L DyPt₂, which suggests that it is more ordered than 1 L DyPt₂. However, a closer look at its structure reveals differences in the atomic arrangement between on top sited in the moiré pattern (Figure 6.14 d)). This points out that the observed moiré patterns for both 1 L DyPt₂ and 3 L DyPt₂ are incommensurate. Nevertheless, the apparent unit cells of the moiré patterns can be indicated in zoomed-in STM topography images (marked with a white rhombus in Figures 6.14 c) and d)). They are very similar in size, which for 1L DyPt₂ is 2.2 ± 0.2 nm while for 3L DyPt₂ is 2.1 ± 0.2 nm. The apparent corrugation is reduced for 3 L DyPt₂ with respect to the 1 L DyPt₂, indicating structural relaxation with an increasing number of layers. STM topography

images with the same bias and size were compared to minimize the influence of the electronic structure and resolution on the apparent corrugation. The models of termination layers are overlaid on the STM images in Figures 6.14 c) and d). Depending on the tunneling conditions, two contrast can be identified in STM atomically resolved topography images [6, 8], as shown in Figures 6.14 e) – f) and g) – h). The hexagonal lattice formed by the Dy atoms of 1 L DyPt₂ and 3 L DyPt₂ is shown in Figures 6.14 e) and g), respectively. Interatomic distance measured between the species, which is the surface alloy lattice constant, is $a_{1\text{LDyPt}_2} = 510 \pm 2$ pm for 1 L DyPt₂ and $a_{3\text{LDyPt}_2} = 515 \pm 2$ pm for 3 L DyPt₂. The lattice constant of bulk polycrystalline DyPt₂ alloys is estimated as 760.3 pm [58, 159], which significantly exceeds the value obtained in our experiment. However, the lattice constant of bulk polycrystalline DyPt₅ alloys, which should be similar to the lattice constant of DyPt₂ alloys is estimated as 523.8 pm [43]. Also the lattice constant of polycrystalline DyAu₂ and DyAg₂ alloys (522.4 pm and 522.7 pm, respectively [160]) and surface alloys DyAu₂ and DyAg₂ (550 pm and 520 pm, respectively) are closer to obtained experimental values. The kagomé-like lattice formed by Pt atoms surrounding the Dy atoms in the alloy layer of 1 L DyPt₂ and 3 L DyPt₂ is shown in Figures 6.14 f) and h), respectively. The NND of 1 L DyPt₂ is $a_{\text{NND-1LDyPt}_2} = 246 \pm 1$ pm. In the case of 3 L DyPt₂ it was not possible to determine the distance since the single atoms within the Pt rings are not resolved (Figure 6.14 h)). Models of the observed atomic species are overlaid on the STM images. The structural models are depicted in Figure 6.14 i). Gray spheres correspond to Pt atoms, as in Subsection 6.3, while pink spheres represent Dy atoms. Distances between the adjacent layers are enlarged to present the structure more transparently. The structure of single alloy layer is analogous to the 1 L GdPt₂ [145] and other REM-Au [6, 22] and REM-Ag surface alloys [28]. Unlike the Gd-Pt system, Dy-Pt surface alloys take only the form of intermixed Dy-Pt layers directly superimposed on each other, without a kagomé interlayer, thus forming multilayers of DyPt₂.

The Dy-Pt surface alloys were further analyzed through experimental LEED patterns and their simulations, as shown in Figure 6.15. In the 1 L DyPt₂ LEED pattern, the Pt(111) substrate signal marked with $\mathbf{a}_1, \mathbf{a}_2$ vectors, is visible. However, the diffraction spots are poorly visible due to overlaying satellites around the main spots from the NND of surface alloy. Vectors $\mathbf{b}_1, \mathbf{b}_2$ and $\mathbf{d}_1, \mathbf{d}_2$ forms (0.8881×0.8881) and $(0.8881 \times 0.8881)R30^\circ$ superstructures with regard to the Pt(111) substrate. In contrast to 1 L GdPt₂, there are two rotational domains, one parallel to the substrate and the other rotated by $30 \pm 3^\circ$. Both reveal lattice constant contraction of about 11 % with respect to the pure Pt(111) lattice constant, which is possible due to the structure buckling observed also for Gd-Pt surface alloys [145]. The Dy atoms are pushed out from the alloy layer, and the Pt atoms surrounding Dy may form a kagomé-like lattice around them with a contracted lattice constant. Due to the structure buckling another superstructure formed by Dy atoms, marked with vectors $\mathbf{c}_1, \mathbf{c}_2$ and $\mathbf{e}_1, \mathbf{e}_2$ is observed. Following the Pt lattices, Dy lattices occur in two rotational

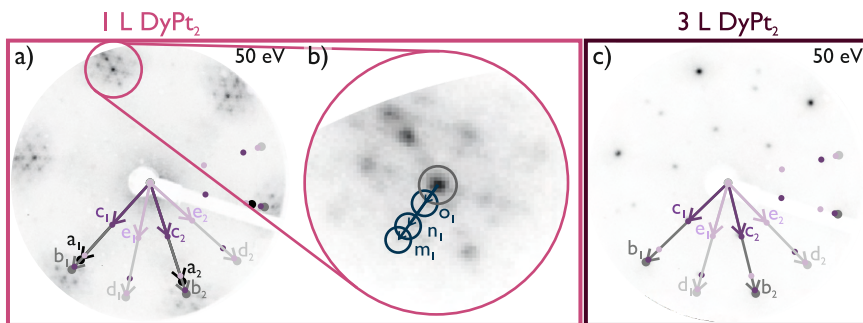


Figure 6.15: Dy-Pt surface alloys – experimental LEED diffraction images taken for electrons energy of 50 eV with simulated LEED patterns overlaid on the half of image of a) 1 L DyPt₂, b) zoom-in on the satellites spots, and c) 3 L DyPt₂. Black vectors ($\mathbf{a}_1, \mathbf{a}_2$) points Pt(111) structure. Gray vectors ($\mathbf{b}_1, \mathbf{b}_2$ and $\mathbf{d}_1, \mathbf{d}_2$) point the lattice of Pt atoms forming surface alloys, not rotated and rotated relative to the substrate, respectively. Purple vectors ($\mathbf{c}_1, \mathbf{c}_2$ and $\mathbf{e}_1, \mathbf{e}_2$) indicate the lattice formed by Dy atoms from alloy layers that are not rotated and rotated relative to the substrate, respectively. Blue vectors $\mathbf{m}_1, \mathbf{n}_1, \mathbf{o}_1$ indicates moiré pattern lattice constants. Single vectors are indicated to keep the image transparent.

domains (1.8375×1.8375) and $(1.8375 \times 1.8375)R30^\circ$ with respect to the Pt(111) substrate. Satellites, described by $\mathbf{m}_1, \mathbf{n}_1, \mathbf{o}_1$ vectors in zoom-in of Figure 6.15 a), arise from slight differences in interatomic distances resulting from the moiré pattern [27]. Numerous satellite spots confirm the complex and highly disturbed structure of the moiré pattern. Three main vectors whose lengths point to the moiré pattern constants of 3.6 nm, 5.0 nm, and 8.8 nm are observed when enlarged. Reproduced moiré pattern's unit cells are shown with white dashed lines in Figure 6.14 a). They correspond respectively to contracted (2×2) , relaxed (2×2) , and (4×4) of apparent moiré pattern's unit cells. The 3 L DyPt₂ LEED pattern is very similar to the pattern of 2 L GdPt₅ (Figure 6.5 c)). There is no signal from Pt(111) substrate observed anymore. Vectors $\mathbf{b}_1, \mathbf{b}_2$ and $\mathbf{d}_1, \mathbf{d}_2$ forms (0.9025×0.9025) and $(0.9025 \times 0.9025)R30^\circ$ superstructures with regard to the Pt(111) substrate. The Pt lattice is less contracted than in the case of 1 L DyPt₂ most probably due to the structure relaxation with increased layers number. Superstructures formed by vectors $\mathbf{c}_1, \mathbf{c}_2$ and $\mathbf{e}_1, \mathbf{e}_2$ are (1.8592×1.8592) and $(1.8592 \times 1.8592)R30^\circ$ with respect to the Pt(111) substrate. The resolution of the LEED image does not allow for analyzing the moiré pattern. There are only shadows around the main NND spots without any pronounced satellites. LEED diffraction patterns confirmed that two rotational domains of 3 L DyPt₂ coexist on the sample. The presented LEED images were selected as representatives of a wide energy range of data, and all of them were taken for electron energy 50 eV. Any differences between the reciprocal and real space dimensions, especially the species on the LEED images' edges, may be caused by distortions due to the LEED screen curvature.

Dy-Pt surface alloys form DyPt₂-type alloys. Their atomic structure is almost identical and the lattice constants have very similar values. They

differ in the apparent corrugation and moiré pattern. With the increased number of layers the corrugation reduces, and moiré pattern dislocation lines disappear pointing out to the structural relaxation. Both, 1 L DyPt₂ and 3 L DyPt₂, come in two configurations: parallel to the substrate lattice and rotated by 30°.

6.4.2 Electronic properties of Dy-Pt surface alloys

Similarly, as in the Gd-Pt system, the moiré pattern influence on electronic properties was investigated by LTS along the moiré pattern's unit cell (shown in Figure 6.16). The arrows on STM topography images indicate the line and direction of the LTS recordings, with 32 points recorded at a constant spacing. In the case of 1 L DyPt₂, the differences observed in unoccupied states are much smaller than those in occupied states, while in 3 L DyPt₂ the variation level is comparable for both sides. The differences are mainly due to the various intensity of the peaks, caused by the varying coupling strength of the surface alloy with the substrate. No energy shift is observed for the most pronounced peaks within the different regions of the moiré pattern's unit cell, excluding the occurrence of dispersion states.

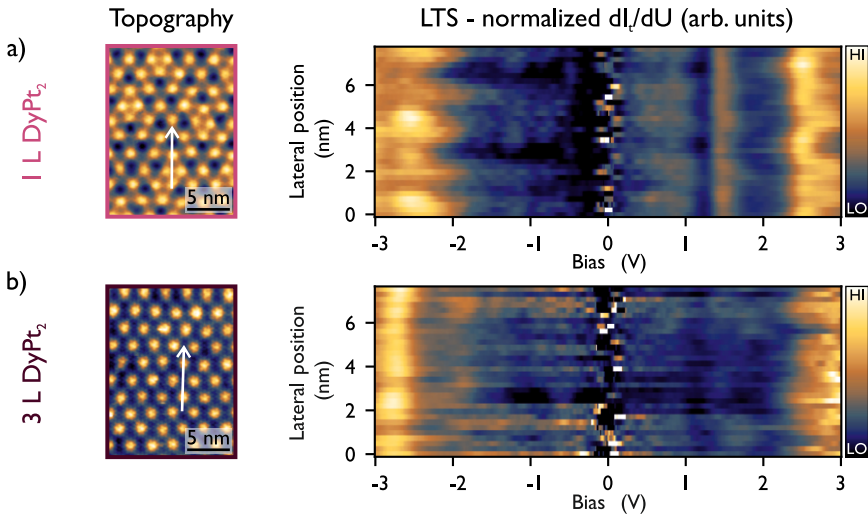


Figure 6.16: Dy-Pt surface alloys – LTS and STM topography images with marked LTS position of a) 1 L DyPt₂, b) 3 L DyPt₂. Tunneling parameters: a) $I_{\text{stab}} = 5$ nA, $U_{\text{stab}} = 3$ V, $U_{\text{mod}} = 50$ mV, $\omega_{\text{mod}} = 49.95$ kHz, b) $I_{\text{stab}} = 5$ nA, $U_{\text{stab}} = 3$ V, $U_{\text{mod}} = 50$ mV, $\omega_{\text{mod}} = 49.95$ kHz.

Figure 6.17 shows the averaged LTS for both surface alloys. Both surface alloys have two main maxima, one on the unoccupied states' side and another on the occupied states' side. The one around -2.55 ± 0.05 V for 1 L DyPt₂ and -2.70 ± 0.05 V for 3 L DyPt₂ may be attributed to Pt states [161]. The most pronounced maximum observed in the unoccupied states consists of two components. 1 L DyPt₂ exposes merged 2.55 ± 0.05 V

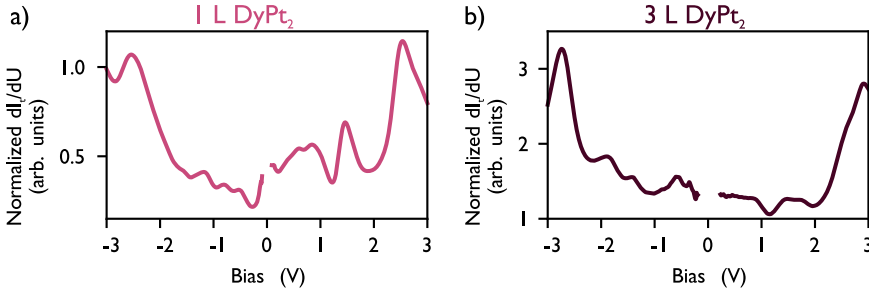


Figure 6.17: Dy-Pt surface alloys – averaged LTS spectra from Figure 6.16 of a) 1 L DyPt₂, b) 3 L DyPt₂.

and 2.85 ± 0.05 V with the dominance of the former, while 3 L DyPt₂ combines 2.55 ± 0.05 V with 2.90 ± 0.05 V with the dominance of the latter. Similarly, as for Gd, the 4f states of Dy rapidly vanish into the vacuum therefore observed peaks are most probably the combination of 5d and 6s states of Dy. In the case of 1 L DyPt₂, the maximum on the unoccupied states' side is more intense, while in 3 L DyPt₂ the maximum on the occupied states' side has a higher intensity. However, the difference is so small that it is comparable to the variations in electronic states' intensity resulting from the different strengths of the interaction of the surface alloy with the substrate. Between the mentioned peaks several electronic states of lower intensity are observed. 1 L DyPt₂ have a single peak with relatively high intensity at 1.45 ± 0.05 V and two smaller distinct peaks at 0.60 ± 0.05 V and 0.85 ± 0.05 V. 3 L DyPt₂ have a plateau from E_F up to 0.85 ± 0.05 V and two separated small peaks at 1.45 ± 0.05 V and 1.75 ± 0.05 V. On the occupied states' side, the discrepancy is greater the farther from the E_F . Both surface alloys have small peaks around $(0.50 - 0.55) \pm 0.05$ V, $(0.80 - 0.90) \pm 0.05$ V, and $(1.20 - 1.40) \pm 0.05$ V. Further, 1 L DyPt₂ signal sharply increases where three peaks may be distinguished 1.55 ± 0.05 V, 1.90 ± 0.05 V with the maximum on 2.55 ± 0.05 V. In 3 L DyPt₂ two peaks at 1.40 ± 0.05 V and 1.90 ± 0.05 V precede the sharp signal increase with the maximum at 2.70 ± 0.05 V. The lower intensity peaks observed between main states are the combination of 5d and 6s states of Dy and Pt. The presence of Dy and Pt signals and no clear dominance of any of them proves that the terminating layer consists of both species.

High-bias regime LTS (up to 10 V) showed that the field states position varies slightly within the moiré pattern. The most opposite spectra are observed for the *top* and *bottom* regions of its unit cell (marked with arrows in STM topography image in Figure 6.18 c)). Representative spectra collected for the *top* (yellow), and *bottom* (navy) sites of the moiré pattern are presented in Figure 6.18 a). The energies of the FER states were extracted from each spectrum taken along the line marked in Figure 6.18 c). Using the Gaussian function fitting the exact position of each peak was calculated. The assignment of FER's order follows the description in [89]. Figure 6.18 b) shows only two borderline plots for *top* and *bottom* positions on the moiré

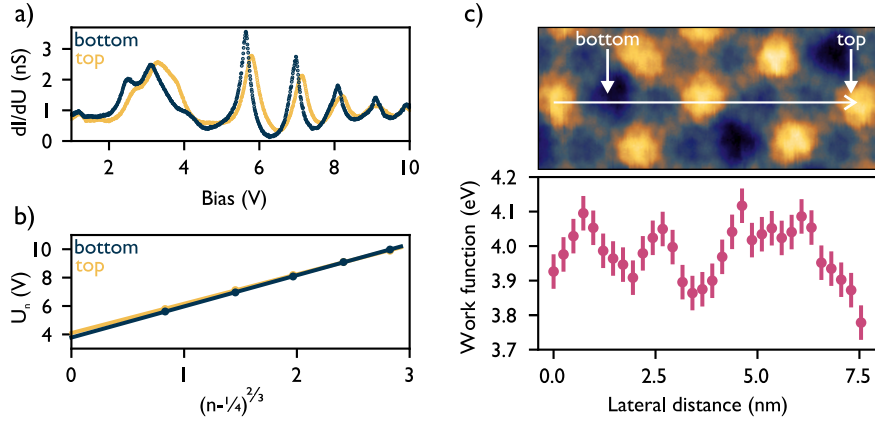


Figure 6.18: Field emission spectroscopy of 1 L DyPt₂ – a) dI_t/dU signal for high bias range taken from top (yellow) and bottom (navy) regions on moiré pattern’s unit cell. Tunneling parameters: $I_{stab} = 1$ nA, $U_{stab} = 4$ V, $U_{mod} = 50$ mV, $\omega_{mod} = 6777$ Hz. b) Plot of the FER peaks position U_n as a function of FER quantum number n . Points – the energy of the FER states taken from a); lines – linear fitting. c) Surface work function values variation along the white arrow in the STM topography image.

pattern of the FER peaks positions as a function of their quantum number $(n - \frac{1}{4})^{\frac{2}{3}}$. The y-intercept indicates the value of the local work function of the 1 L DyPt₂ surface alloy (ϕ_{1LDyPt_2}). Plot in Figure 6.18 c) summarizes all work function values obtained within the moiré pattern at 32 evenly spaced points. The work function of 1 L DyPt₂ surface alloy fluctuates from 3.78 ± 0.05 eV for the *top* site to 4.12 ± 0.05 eV for the *bottom* site. Within the more uniform areas of the moiré pattern, the fluctuations are smaller. The work function of Pt(111), which is $\phi_{Pt(111)} = 5.77$ eV [35], is reduced by surface alloying in consistency with previous reports of other surface alloys [7, 25].

The electronic properties of both surface alloys are comparable. Since the termination layer is formed by an intermixed Dy-Pt layer in both cases, the mixture of Dy and Pt electronic states is observed. The reactivity of both surface alloys is thus comparable. The states modulate with the moiré pattern variations. Alloying of Pt with Dy reduces the Pt work function leading to the ϕ_{1LDyPt_2} of $(3.78 - 4.12) \pm 0.05$ eV.

6.4.3 Dy-Pt surface alloys phase diagram

The alloying of Pt(111) substrate with Dy resulted in the formation of a greater variety of ordered surface structures compared to alloying with Gd, as described in Subsection 6.3. It has been previously demonstrated that Dy-Pt surface alloys do not form a Pt kagomé overlayer upon increasing the temperature up to the overheating of the sample. For further details about temperature dependence, refer to Subsection 6.2. In this context, the statistics presented in Figure 6.19 were collected only for various surface coverage

in a range from 0.7 L to 7.2 L. When the Dy coverage is less than 1 L, the surface is primarily occupied in 41 % with Dy-Pt clusters and in 58 % with 1 L DyPt₂. The remaining surface is occupied by multilayers. At 1.2 L Dy coverage, almost the entire sample area is covered with 1 L DyPt₂ (95 %). As Dy coverage increases, the areas occupied by multilayers also increase and cover less than 30 % of the sample. The composition of the surface observed for the Dy coverage of 4.8 L is unclear. The domination of multilayers in surface occupancy may result from local structure inhomogeneity and insufficient statistical samples. STM is a local technique, where the scanning area is limited to hundreds of nm, and even the registration of several images in globally different locations may not provide a good overview of the surface composition. Most likely, the areas with locally increased density of multilayers were imaged here. When Dy coverage reaches 7.2 L, the surface is dominated by 3 L DyPt₂, and the remaining part (about 37 %) is occupied by multilayers. Above 1 L coverage, a structure similar to 1 L DyPt₂ is also observed. Its atomic structure is very much like 1 L DyPt₂ and the only difference is a slightly more ordered moiré pattern. This may be due to different stacking concerning the Pt(111) substrate. Apart from the coverage of 4.8 L, the trend of the dependence of the observed structures on their area occupancy is preserved in the whole investigated coverage range.

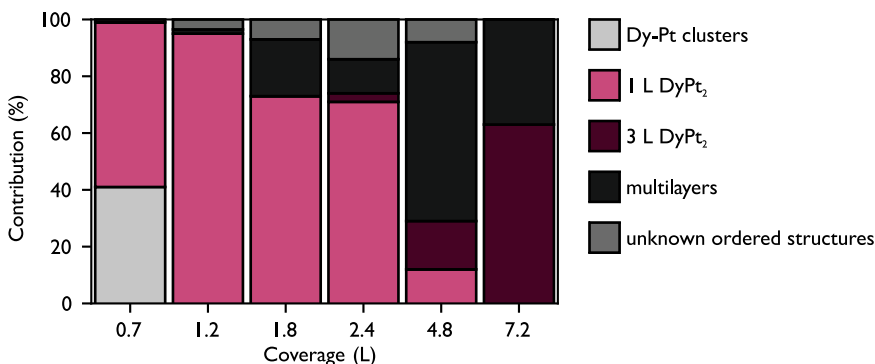


Figure 6.19: Dy-Pt surface alloys area occupancy – occupancy graphs as a function of Dy coverage in a range from 0.7 L to 7.2 L. Samples were prepared using a reactive growth process with a substrate temperature of 1050 K.

Despite the large variety of ordered structures formed by the Dy-Pt system it is possible to prepare samples almost fully covered with the chosen surface alloy. Based on these statistics, it is possible to determine the growth conditions of the sample in the vast majority covered with 1 L DyPt₂ or 3 L DyPt₂.

6.4.4 Magnetic properties of Dy-Pt surface alloys

XMCD measurements of the Dy-Pt system were conducted at the SLS (Paul Scherrer Institute) using X07MA X-Treme beamline described in Subsection 5.3. The experiments were mainly performed when the sample was

cooled down to the base temperature of 3 K, following the beamline temperature calibration. Only the temperature-dependent magnetization loops used for the calculation of T_C were recorded for varying temperatures, which were estimated according to calibration data. The beamline energy range allowed the investigation of Dy $M_{4,5}$ absorption edges. The XMCD measurements were recorded when the sample was magnetized by the external magnetic field of $\mu_0 H = 6.8$ T, which is the highest possible magnetic field at this endstation. The XMCD spectra were obtained by calculating the difference between μ_+ and μ_- XAS spectra. XMCD hysteresis loops were recorded for two photon energies: one at the M_5 edge, and the other at pre-edge energy for normalization purposes. All data processing followed the same procedures as described for the Gd-Pt system in Subsection 6.3.4. Similarly, the measurements were carried out for two beam-sample configurations (normal $\alpha = 0^\circ$ and grazing $\alpha = 70^\circ$) to determine the easy magnetization axis. The samples were reproduced *on-site* using the beamline's preparation chamber and verified the structural properties of the samples before the experiment by means of LEED and STM. Further, the sample was transferred *in vacuo* to the cryostat, where it was cooled down to the base temperature. After thermal stabilization, the XMCD measurements were performed.

Figures 6.20 a) and b) show the XAS spectra taken with grazing incidence of the x-ray beam for $M_{4,5}$ absorption edges of 1 L DyPt₂ and 3 L DyPt₂. The color concept from Subsection 6.3.4 is preserved. Two distinct absorption edges are observed, confirming d states splitting. A clear difference in the absorption of left and right circularly polarized light is visible in these graphs. Calculated XMCD spectra for grazing and normal incidences of the x-ray beam for both surface alloys are shown in Figures 6.20 c) and d). In both graphs, dichroism is observed for both beam-sample configurations. The energies of absorption edges have the same values within the energy accuracy in all cases. The M_5 edge is split into two extrema with a maximum at 1288.9 ± 0.1 eV and minimum at 1284.9 ± 0.1 eV, while M_4 edge has a maximum at 1322.1 ± 0.1 eV. The tabulated electron binding energy of M_5 edge is 1292.6 eV while M_4 edge 1333 eV. The experimental values are shifted towards lower energies due to the ionization of Dy atoms when involved in the formation of Dy-Pt surface alloys. Dy has a non-zero orbital magnetic moment and intrinsic anisotropy, and for that reason, a pronounced difference is observed in the intensity of XMCD signals, which is significantly higher for grazing incidence in both surface alloys.

Using magneto-optical sum rules for $M_{4,5}$ edges spin and orbital magnetic moments were calculated. The magnetic dipole operator for Dy was assumed as 0.15 following [157] and the number of the holes as 5. The orbital magnetic moments are $m_{l-1LDyPt_2} = 3.80 \pm 0.01 \mu_B$ and $m_{l-3LDyPt_2} = 3.81 \pm 0.01 \mu_B$. The value is non-zero, as expected for Dy, but it is significantly lower than simulated for Dy³⁺ ion ($5.11 \mu_B$ [157]). The spin magnetic moments were also calculated and found to be $m_{s-1LDyPt_2} = 3.32 \pm 0.01 \mu_B$ and $m_{s-3LDyPt_2} = 3.28 \pm 0.01 \mu_B$. The values are also lower than simulated for Dy³⁺ ion ($-4.48 \mu_B$ [157]). The total magnetic moment

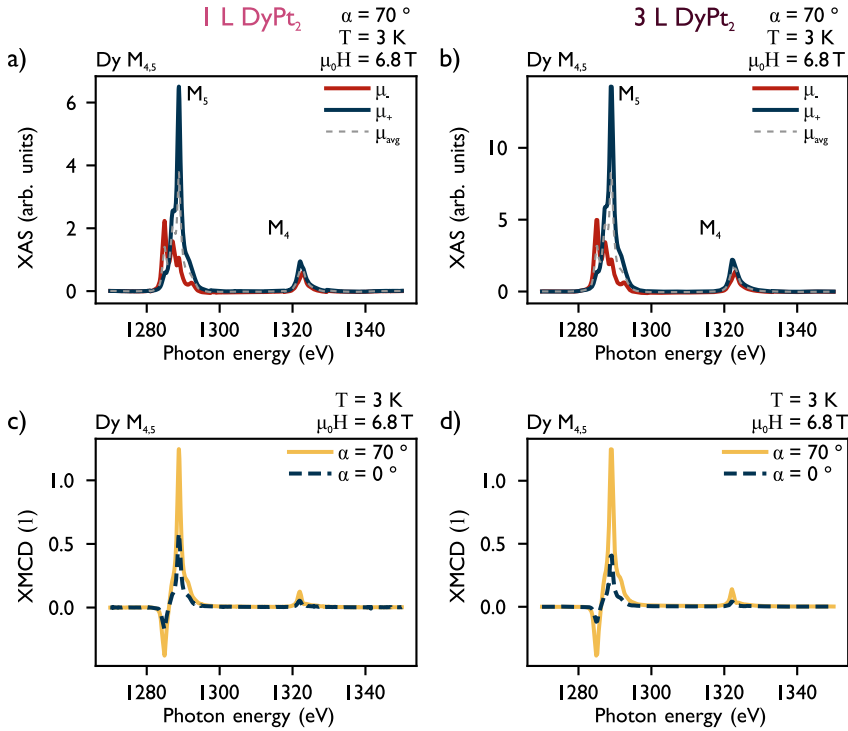


Figure 6.20: Dy-Pt surface alloys – a) and b) 1 L DyPt₂ and 3 L DyPt₂ XAS spectra taken with grazing incidence of the x-ray beam, c) and d) XMCD spectra for grazing and normal incidences of the x-ray beam for 1 L DyPt₂ and 3 L DyPt₂, respectively.

of Dy of $10.65 \mu_B$ [2, 147] is also higher than the spin and orbital moments obtained from the experiment. Following the observations for the Gd-Pt system this may be caused by charge transfer to the Pt atoms of alloy and substrate layers.

Magnetization curves taken at M₅ edge of 1 L DyPt₂ and 3 L DyPt₂ for normal and grazing incidence angles are shown in Figures 6.21 a) and b). The photon energies of edge and pre-edge were extracted from XMCD shown in Figures 6.20 c) and d). For both surface alloys, only a single magnetic phase is present in the sample, namely, a ferromagnetic phase with an in-plane easy magnetization axis. The crystal field exposes a strong in-plane arrangement, additionally affected by the internal anisotropy of Dy. After reaching the saturation, magnetization increases linearly up to the maximum magnetic field, indicating that the measurement temperature is close to the material's T_C . The loops' openings are smaller than the resolution of full range hysteresis loops, thus the limited range graphs of magnetization loops in grazing incidence are shown in Figure 6.21 c) and d). The coercive field is $H_{C-1LDyPt_2} = 20 \pm 2$ mT and $H_{C-3LDyPt_2} = 30 \pm 2$ mT for 1 L DyPt₂ and 3 L DyPt₂, respectively. The values are significantly lower than the coercive field of bulk DyPt₂ alloy of 66 mT [58]. At the same time, they

are slightly higher than H_C for the Gd-Pt system and local coercive field of GdAu₂[8]. This suggests that 3 L DyPt₂ is a harder ferromagnet than 1 L DyPt₂. 1 L DyPt₂ grazing hysteresis loop signal saturates at 0.45 T, while the value for 3 L DyPt₂ is lower and stands at 0.3 T.

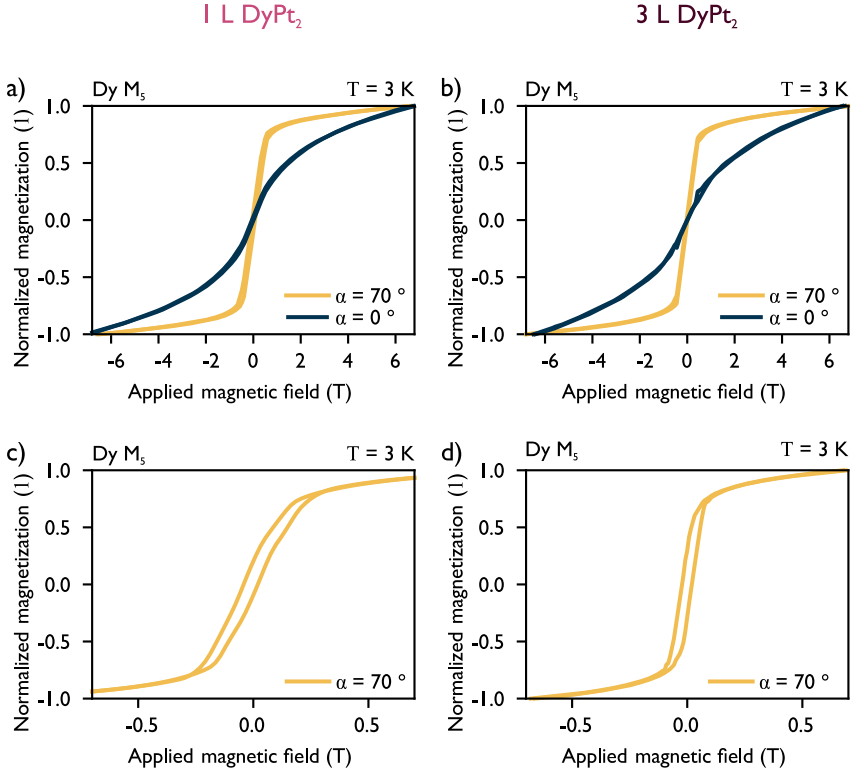


Figure 6.21: Dy-Pt surface alloys – a) and b) hysteresis loops registered for normal and grazing incidence angles for 1 L DyPt₂ and 3 L DyPt₂, c) and d) limited range hysteresis loops for 1 L DyPt₂ and 3 L DyPt₂, respectively.

Magnetization loops recorded at various temperatures, allow an Arrott plot estimation of the Curie temperature of the surface alloys [28, 162]. Figures 6.22 a) and b) presents the Arrott plots derived from the in-plane magnetization loops at different temperatures. The linear fitting of high magnetic field data intersects the y-axis at different M_0^2 points. Figures c) and d) show the dependence of the intercept as a function of temperature. The point at which the intercept changes the sign corresponds to T_C . Two types of functions were fitted to the data: the second-order polynomial function according to [24, 28, 32] and linear following [11]. From linear fitting the T_C are 5 ± 1 K and 3 ± 1 K for 1 L DyPt₂ and 3 L DyPt₂, respectively. The quadratic function fitting, although better reflecting the trend of the data, gives values significantly different from those suggested on the basis of observations of experimental results (3 ± 1 K and 7 ± 1 K, respectively). Uncertainty factors of M_0^2 result from the goodness of fit-

ting of a linear function to the $M^2(\mu_0 H/M)$. This indicates that the base temperature of measurements is already very close to the Curie point for both surface alloys, thus the linear fitting seems more likely. T_C observed for surface alloys are significantly lower compared to the bulk DyPt₂ alloy (25 – 29 K) [56, 58].

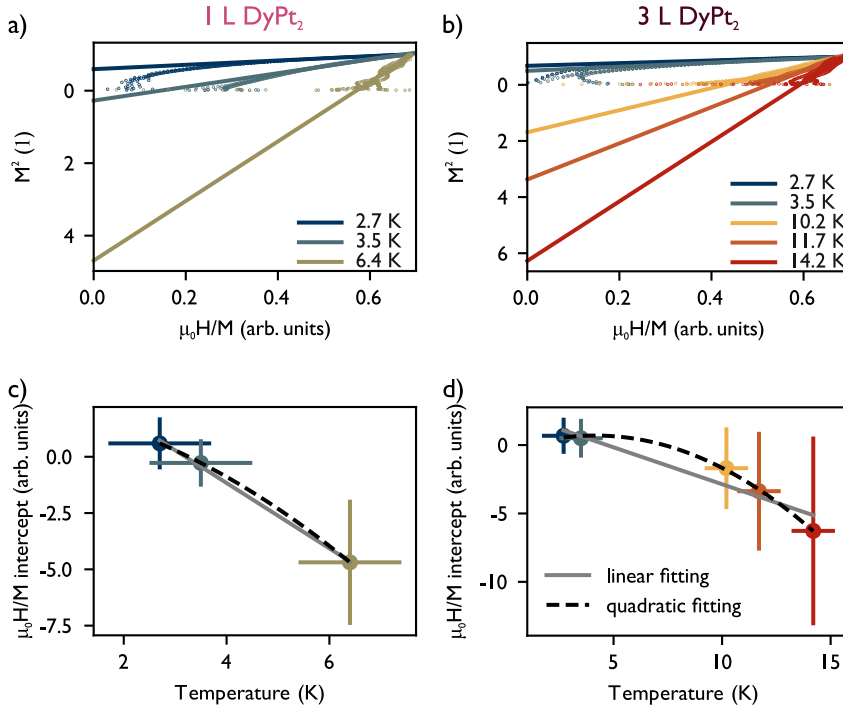


Figure 6.22: Dy-Pt surface alloys – Arrott plots of a) 1 L DyPt₂ and b) 3 L DyPt₂.

Both investigated Dy-Pt surface alloys, 1 L DyPt₂ and 3 L DyPt₂, are ferromagnetic with an in-plane easy magnetization axis. Their coercivity is of the order of tenths mT. Experimentally estimated orbital and spin magnetic moments are lower than for Dy ion, indicating the charge transfer and polarization of Pt atoms. Arrott plots pointed out that both surface alloys have a low T_C with a value at the level of the base temperature of the measurements and significantly lower than their bulk counterpart.

Chapter 7

Summary and conclusions

In the dissertation, I have demonstrated for the first time that it is possible to prepare 2D Gd-Pt and Dy-Pt surface alloys on a Pt(111) substrate using a reactive growth process. Although Gd and Dy belong to the same group of elements called rare earth metals, significant differences in the properties of the prepared surface alloys were observed. Low-dimensional REM-Pt alloys usually adopt REM-Pt₂ and REM-Pt₅ stoichiometry. In the Gd-Pt system, both types are observed, while the Dy-Pt system only forms DyPt₂ and its multilayers. All of the investigated surface alloys exhibit long-range (moiré pattern) and short-range structural orders that differ in their lattice constants. The locally investigated electronic structure is relatively uniform within the moiré unit cell, with small deviations whose strength depends on the surface alloy type. For 1 L GdPt₅ and 2 L GdPt₅, which are terminated with a kagomé layer containing only Pt atoms, the deviations are less significant than for 1 L GdPt₂, terminated with intermixed Gd-Pt layer, where the maximum shift is of the order of 0.5 eV. Variations of the same order are observed for 1 L DyPt₂ and 3 L DyPt₂, suggesting that they mostly depend on the termination layer. The work function value determined for 1 L DyPt₂ is also fluctuating with the moiré pattern, but in general, alloying reduces the value of pure Pt work function and it stands between the work function of Pt and Dy. The electronic structure of 1 L GdPt₅ and 2 L GdPt₅ is dominated by the Pt states, while for 1 L GdPt₂, 1 L DyPt₂, and 3 L DyPt₂ it consists of a mixture of REM and Pt states. The termination layer has a great impact on the reactivity, which was observed to be higher for REM-Pt₂ surface alloys. The correlation between the growth parameters and the fraction of surface occupied by each structure combined with their structural and electronic properties confirmed their identification. Simplified phase diagrams showing the dependence of surface alloys' contribution in sample surface area as a function of coverage and temperature allow the reproduction of samples covered almost exclusively with chosen-type surface alloy. It is possible to prepare the sample covered with more than 90 % of 1 L GdPt₅, 2 L GdPt₅, 1 L DyPt₂, and 3 L DyPt₂. 1 L GdPt₂ is more difficult to obtain

due to its high sensitivity to temperature and formation of Pt overlayers and the highest obtained coverage reached 65 %.

Table 7.1 summarizes the magnetic properties of the investigated Gd-Pt and Dy-Pt surface alloys. All of them are ferromagnetic with low Curie temperature of the order of a few Kelvins which makes their practical applications limited. Such a low T_C , makes the exact determination challenging since it is very close to the measurement base temperature, thus obtained T_C should be considered with caution. For surface alloys T_C decreases with the increase of layers number. At the same time, it is significantly lower than the value obtained for bulk polycrystalline alloy. This indicates that the interaction of surface alloy with the first substrate layer stabilizes the T_C . The coercive fields of surface alloys are in the order of tens of mT, and increase with a surface alloy layer number, pointing out that 2D surface alloys are softer magnets than their bulk counterparts. Considering the case of the Dy-Pt system, with the growth of subsequent layers, an increase of H_C is expected until the value reaches the bulk H_C value. Easy magnetization axis of 1 L GdPt₅, 1 L DyPt₂, and 3 L DyPt₂ is in-plane, while only 2 L GdPt₅ presents the out-of-plane order. This shows that the crystal field formed by Pt kagomé interlayers greatly impacts the magnetic ordering. The Pt kagomé layers that separate the intermixed Gd-Pt layers cause the crystal field that forces the out-of-plane ordering of Gd magnetic moments in 2 L GdPt₅. On the other hand, in the case of Dy-Pt surface alloys, due to the lack of pure platinum interlayers between alloy layers, the interaction within the atomic layer is stronger than between the adjacent layers, and the in-plane easy magnetization axis is observed. Previous research focuses mainly on polycrystalline materials and lacks information on these bulk alloys' anisotropy. However, the presented results for 1 L DyPt₂ and 3 L DyPt₂ show that the in-plane easy axis occurs for both surface alloys. It can therefore be assumed that this state of affairs is going to be preserved for thicker alloys. Similarly, thicker alloys than 2 L GdPt₅ are expected to maintain the out-of-plane easy magnetization axis due to the crystal field formed by Pt kagomé interlayers surrounding the intermixed alloy layers. Magnetic moments of Gd and Dy extracted from experimental data using sum rules are lower than expected for REM³⁺ ions proving the charge transfer and polarization of Pt atoms. DFT calculations confirmed that not only Pt atoms forming surface alloys are polarized, but also Pt atoms from the first two substrate layers.

The presented research offers significant insight into 2D surface alloys, specifically regarding REM-NM. The conclusions summarized above hint at possible new directions of studies. Despite the high spin-orbital coupling of Pt and high magnetic moments of REM, no non-collinear structure was observed. To confirm this, it is recommended to conduct spin-polarized STM measurements at a base temperature below 2 K. The moiré patterns observed in all surface alloys have large lattice constants, making them ideal substrates for the templated growth of independent magnetic structures separated by significant distances varying with the chosen surface alloy as a substrate. 2 L GdPt₅ that has the highest moiré pattern lattice constant among the

Table 7.1: Summary table – magnetic properties of investigated Gd-Pt and Dy-Pt surface alloys.

alloy	T_C (K)	H_C (mT)	m_l (μ_B)	m_s (μ_B)	easy magnetization axis
1 L GdPt ₅	9 ± 1	15 ± 2	-0.03 ± 0.01	5.82 ± 0.01	in-plane
2 L GdPt ₅	7 ± 1	20 ± 2	0.15 ± 0.01	5.97 ± 0.01	out-of-plane
bulk GdPt ₅	13.9 [57]			7.1 ± 0.1 [57]	
1 L DyPt ₂	5 ± 1	20 ± 2	3.80 ± 0.01	3.32 ± 0.01	in-plane
3 L DyPt ₂	3 ± 1	30 ± 2	3.81 ± 0.01	3.28 ± 0.01	in-plane
bulk DyPt ₂	25 – 29 [56, 58]	66 [58]			

investigated surface alloys offers to use it in two ways. On the one hand, for the deposition of large molecules, and on the other hand, for the deposition of small molecules but with larger separation distances. Different termination layers in surface alloys can be studied to determine the influence of the substrate on deposited molecules. A termination layer of intermixed REM-Pt enhances the interaction of molecules with REM atoms, whereas Pt kagomé layers weaken these interactions. Small T_C obtained for the surface alloys may also be preferred in magnetic experiments on molecules. The transition between ferromagnetic and paramagnetic states of the substrate already at low temperatures allows for control of the magnetism of the substrate avoiding excitation or diffusion of molecules deposited on top. Based on the study of thicker films of several dozen layers the compression of Pt kagomé layer may be useful in oxygen-reduction reactions in membrane fuel cells. Finally, The research also presents the opportunity to explore other REM metals with Pt to discover a harder magnetic material with a higher T_C . Most likely, however, the key to success here would be trying different substrates.

Bibliography

- [1] J. E. Bickel, F. Meier, J. Brede, A. Kubetzka, K. Von Bergmann, and R. Wiesendanger, “Magnetic properties of monolayer Co islands on Ir(111) probed by spin-resolved scanning tunneling microscopy,” *Physical Review B - Condensed Matter and Materials Physics*, vol. 84, no. 5, p. 054454, 2011. DOI: 10.1103/PhysRevB.84.054454.
- [2] W. C. Koehler, “Magnetic properties of rare-earth metals and alloys,” *Journal of Applied Physics*, vol. 36, no. 3, pp. 1078–1087, 1965. DOI: 10.1063/1.1714108.
- [3] S. Cotton, *Lanthanide and Actinide Chemistry*, D. Woollins, B. Crabtree, D. Atwood, and G. Meyer, Eds. Chichester: John Wiley and Sons, 2006, p. 280, ISBN: 9780470010082. DOI: 10.1002/0470010088.
- [4] S. B. Castor and J. B. Hedrick, “Rare Earth Elements,” in *Industrial Minerals and Rocks*, J. Kogel, N. Trivedi, and J. Barker, Eds., 7th, Littleton, CO, USA: Society for Mining, Metallurgy and Exploration, 2006, pp. 769–792, ISBN: 0873352491.
- [5] The Geological Society of London, “Rare Earth Elements. A Briefing note by the Geological Society of London,” The Geological Society of London, Tech. Rep., 2011, pp. 1–13. [Online]. Available: <https://www.geolsoc.org.uk/~media/shared/documents/policy/Rare%20Earth%20Elements%20briefing%20note%20final%20%20new%20format.pdf>.
- [6] M. Corso, L. Fernández, F. Schiller, and J. E. Ortega, “Au(111)-based nanotemplates by Gd alloying,” *ACS Nano*, vol. 4, no. 3, pp. 1603–1611, 2010. DOI: 10.1021/nn901345s.
- [7] M. Corso *et al.*, “Rare-earth surface alloying: A new phase for GdAu₂,” *Physical Review Letters*, vol. 105, no. 1, p. 016101, 2010. DOI: 10.1103/PhysRevLett.105.016101.
- [8] M. Bazarnik *et al.*, “Atomically resolved magnetic structure of a Gd-Au surface alloy,” *Physical Review B*, vol. 99, no. 17, p. 174419, 2019. DOI: 10.1103/PhysRevB.99.174419.
- [9] L. Fernández *et al.*, “Co nanodot arrays grown on a GdAu₂ template: Substrate/nanodot antiferromagnetic coupling,” *Nano Letters*, vol. 14, pp. 2977–2981, 2014. DOI: 10.1021/nl403471z.

- [10] L. Fernández, M. Corso, F. Schiller, M. Ilyn, M. Holder, and J. E. Ortega, "Self-organized growth of high density magnetic Co nanodot arrays on a Moiré template," *Applied Physics Letters*, vol. 96, p. 013 107, 2010. DOI: 10.1063/1.3280900.
- [11] M. Abadía *et al.*, "Polymerization of Well-Aligned Organic Nanowires on a Ferromagnetic Rare-Earth Surface Alloy," *ACS Nano*, vol. 11, pp. 12 392–12 401, 2017. DOI: 10.1021/acsnano.7b06374.
- [12] J. C. Slater, "Atomic radii in crystals," *The Journal of Chemical Physics*, vol. 41, no. 10, pp. 3199–3204, 1964. DOI: 10.1063/1.1725697.
- [13] J. Wiebe, *Lecture notes in nanostrukturphysik ii – magnetismus und oberflächenphysik*, Department of Physics, Universität Hamburg, 2019.
- [14] S. Blundell, *Magnetism in Condensed Matter*, First edition. New York: Oxford University Press, 2001, pp. 80–81, ISBN: 0198505914.
- [15] J. Stöhr and H. C. Siegmann, *Magnetism: From fundamentals to nanoscale dynamics*, First edition. Berlin Heidelberg: Springer-Verlag, 2006, p. 822, ISBN: 3540302824. DOI: 10.1007/978-3-540-30283-4.
- [16] J. Kanamori, "Superexchange interaction and symmetry properties of electron orbitals," *Journal of Physics and Chemistry of Solids*, vol. 10, pp. 87–98, 1959. DOI: 10.1016/0022-3697(59)90061-7.
- [17] P. W. Anderson, "New approach to the theory of superexchange interactions," *Physical Review Journals Archive*, vol. 115, no. 1, 1959. DOI: 10.1103/PhysRev.115.2.
- [18] M. Ohring, *The materials science of thin films*, First edition. London: Academic Press, 1992, p. 742, ISBN: 012524990X.
- [19] M. A. Herman, W. Richter, and H. Sitter, *Epitaxy: Physical Principles and Technical Implementation*. Berlin: Springer Berlin Heidelberg, 2010, p. 540, ISBN: 364208737X.
- [20] J. W. Evans, P. A. Thiel, and M. C. Bartelt, "Morphological evolution during epitaxial thin film growth: Formation of 2D islands and 3D mounds," *Surface Science Reports*, vol. 61, pp. 1–128, 2006. DOI: 10.1016/j.surfrep.2005.08.004.
- [21] I. V. Markov, *Crystal growth for beginners Fundamentals of nucleation, crystal growth and epitaxy*, Third edition. Singapore: World Scientific Publishing Co. Pte. Ltd., 1995, p. 436, ISBN: 9810215312.
- [22] M. S. Ormaza *et al.*, "LaAu₂ and CeAu₂ surface intermetallic compounds grown by high-temperature deposition on Au(111)," *Physical Review B - Condensed Matter and Materials Physics*, vol. 88, no. 12, p. 125 405, 2013. DOI: 10.1103/PhysRevB.88.125405.
- [23] A. Correa *et al.*, "Self-texturizing electronic properties of a 2-dimensional GdAu₂ layer on Au(111): The role of out-of-plane atomic displacement," *Nanoscale*, vol. 9, no. 44, pp. 17 342–17 348, 2017. DOI: 10.1039/c7nr04699e.

- [24] L. Fernández *et al.*, “Influence of 4f filling on electronic and magnetic properties of rare earth-Au surface compounds,” *Nanoscale*, vol. 12, no. 43, pp. 22 258–22 267, 2020. DOI: 10.1039/d0nr04964f.
- [25] Y. Que *et al.*, “Two-Dimensional Rare Earth-Gold Intermetallic Compounds on Au(111) by Surface Alloying,” *Journal of Physical Chemistry Letters*, vol. 11, pp. 4107–4112, 2020. DOI: 10.1021/acs.jpclett.0c00981.
- [26] M. Blanco-Rey *et al.*, “Effect of the valence state on the band magnetocrystalline anisotropy in two-dimensional rare-earth/noble-metal compounds,” *Physical Review Research*, vol. 4, p. 013 237, 2022. DOI: 10.1103/physrevresearch.4.013237.
- [27] S. Mousavion *et al.*, “Atomic and mesoscopic structure of Dy-based surface alloys on noble metals,” *New Journal of Physics*, vol. 24, p. 033 048, 2022. DOI: 10.1088/1367-2630/ac5c17.
- [28] M. S. Ormaza *et al.*, “High temperature ferromagnetism in a GdAg₂ monolayer,” *Nano Letters*, vol. 16, pp. 4230–4235, 2016. DOI: 10.1021/acs.nanolett.6b01197.
- [29] A. Correa, B. Xu, M. J. Verstraete, and L. Vitali, “Strain-induced effects in the electronic and spin properties of a monolayer of ferromagnetic GdAg₂,” *Nanoscale*, vol. 8, pp. 19 148–19 153, 2016. DOI: 10.1039/c6nr06398e.
- [30] J. Knippertz *et al.*, “Exchange Splitting of a Hybrid Surface State and Ferromagnetic Order in a 2D Surface Alloy,” *Mesoscale and Nanoscale Physics*, p. 6, 2020. arXiv: 1906.03780.
- [31] C. Xu *et al.*, “A two-dimensional ErCu₂ intermetallic compound on Cu(111) with moiré-pattern-modulated electronic structures,” *Physical Chemistry Chemical Physics*, vol. 22, no. 3, pp. 1693–1700, 2020. DOI: 10.1039/c9cp05585a.
- [32] A. Cavallin *et al.*, “Magnetism and morphology of Co nanocluster superlattices on GdAu₂/Au(111)-(13×13),” *Physical Review B - Condensed Matter and Materials Physics*, vol. 90, no. 23, p. 235 419, 2014. DOI: 10.1103/PhysRevB.90.235419.
- [33] C. Kittel, *Introduction to Solid State Physics*, Eighth edition. New Jersey: John Wiley and Sons, 2005, p. 720.
- [34] F. H. Spedding, A. H. Daane, and K. W. Herrmann, “The crystal structures and lattice parameters of high-purity scandium, yttrium and the rare earth metals,” *Acta Crystallographica*, vol. 9, pp. 559–563, 1956. DOI: 10.1107/s0365110x5600156x.
- [35] H. B. Michaelson, “The work function of the elements and its periodicity,” *Journal of Applied Physics*, vol. 48, no. 11, pp. 4729–4733, 1977. DOI: 10.1063/1.323539.
- [36] S. Miura, T. Kaneko, M. Ohashi, and K. Kamigaki, “Magnetic properties of DyAu₂ and DyAg₂,” *Journal de Physique Colloques*, vol. 32, no. C1, pp. 1124–1125, 1971. DOI: 10.1051/jphyscol:19711401.

- [37] H. J. Albert and L. R. Ruin, "Magnetic Properties of the Platinum Metals and Their Alloys," in *Platinum Group Metals and Compounds*, U. V. Rao, Ed., First edition, American Chemical Society, 1971, ch. 1, p. 16, ISBN: 9780841201354. DOI: 10.1021/ba-1971-0098.ch001.
- [38] I. E. Stephens, A. S. Bondarenko, U. Grønbjerg, J. Rossmeis, and I. Chorkendorff, "Understanding the electrocatalysis of oxygen reduction on platinum and its alloys," *Energy and Environmental Science*, vol. 5, pp. 6744–6762, 2012. DOI: 10.1039/c2ee03590a.
- [39] E. Zamburlini, K. D. Jensen, I. E. Stephens, I. Chorkendorff, and M. Escudero-Escribano, "Benchmarking Pt and Pt-lanthanide sputtered thin films for oxygen electroreduction: fabrication and rotating disk electrode measurements," *Electrochimica Acta*, vol. 247, pp. 708–721, 2017. DOI: 10.1016/j.electacta.2017.06.146.
- [40] A. F. Pedersen *et al.*, "Probing the nanoscale structure of the catalytically active overlayer on Pt alloys with rare earths," *Nano Energy*, vol. 29, pp. 249–260, 2016. DOI: 10.1016/j.nanoen.2016.05.026.
- [41] J. Greeley *et al.*, "Alloys of platinum and early transition metals as oxygen reduction electrocatalysts," *Nature Chemistry*, vol. 1, pp. 552–556, 2009. DOI: 10.1038/nchem.367.
- [42] M. Escudero-Escribano *et al.*, "Pt5Gd as a highly active and stable catalyst for oxygen electroreduction," *Journal of the American Chemical Society*, vol. 134, pp. 16476–16479, 2012. DOI: 10.1021/ja306348d.
- [43] M. Escudero-Escribano *et al.*, "Tuning the activity of Pt alloy electrocatalysts by means of the lanthanide contraction," *Science*, vol. 352, no. 6281, pp. 73–76, 2016. DOI: 10.1126/science.aad8892.
- [44] A. Velázquez-Palenzuela *et al.*, "The enhanced activity of mass-selected Pt x Gd nanoparticles for oxygen electroreduction," *Journal of Catalysis*, vol. 328, pp. 297–307, 2015. DOI: 10.1016/j.jcat.2014.12.012.
- [45] B. Eriksson *et al.*, "Enhanced oxygen reduction activity with rare earth metal alloy catalysts in proton exchange membrane fuel cells," *Electrochimica Acta*, vol. 387, p. 138454, 2021. DOI: 10.1016/j.electacta.2021.138454.
- [46] K. D. Jensen, A. F. Pedersen, E. Zamburlini, I. E. L. Stephens, I. Chorkendorff, and M. Escudero-Escribano, "X-ray Absorption Spectroscopy Investigation of Platinum – Gadolinium Thin Films with Different Stoichiometry for the Oxygen Reduction Reaction," *Catalysts*, vol. 10, no. 978, p. 12, 2020. DOI: 10.3390/catal10090978.
- [47] M. Escudero-Escribano *et al.*, "Active-Phase Formation and Stability of Gd/Pt(111) Electrocatalysts for Oxygen Reduction: An In Situ Grazing Incidence X-Ray Diffraction Study," *Chemistry - A European Journal*, vol. 24, pp. 12280–12290, 2018. DOI: 10.1002/chem.201801587.

- [48] E. T. Ulrikkeholm *et al.*, “Pt_xGd alloy formation on Pt(111): Preparation and structural characterization,” *Surface Science*, vol. 652, pp. 114–122, 2016. DOI: 10.1016/j.susc.2016.02.009.
- [49] E. T. Ulrikkeholm, M. H. Hansen, J. Rossmesl, and I. Chorkendorff, “Investigating the coverage dependent behaviour of CO on Gd/Pt(111),” *Physical Chemistry Chemical Physics*, vol. 18, pp. 29 732–29 739, 2016. DOI: 10.1039/c6cp04575h.
- [50] K. T. Jacob and Y. Waseda, “Thermodynamic properties of platinum-rich intermetallics in the Pt-Gd system,” *Materials Transactions JIM*, vol. 31, no. 2, pp. 135–140, 1990. DOI: 10.2320/matertrans1989.31.135.
- [51] N. C. Baenziger and J. L. Moriarty, “Gadolinium and dysprosium intermetallic phases. I. The crystal structures of DyGa and GdPt and their related compounds,” *Acta Crystallographica*, vol. 14, pp. 946–947, 1961. DOI: 10.1107/s0365110x61002758.
- [52] A. Castets, D. Gignoux, and J. C. Gomez-Sal, “Magnetic properties and structures of equiatomic rare earth-platinum compounds RPt (R = Gd, Tb, Dy, Ho, Er, Tm),” *Journal of Solid State Chemistry*, vol. 31, pp. 197–207, 1980. DOI: 10.1016/0022-4596(80)90021-3.
- [53] J. C. Gómez-Sal, J. Rodríguez Fernández, R. J. López Sánchez, and D. Gignoux, “Electrical resistivity on intermetallic equiatomic RPt compounds with R = La, Pr, Nd, Gd, Tb, Dy, Ho and Er,” *Solid State Communications*, vol. 59, no. 11, pp. 771–776, 1986. DOI: 10.1016/0038-1098(86)90715-5.
- [54] R. H. Taylor, I. R. Harris, and W. E. Gardner, “The electrical and magnetic properties of off-stoichiometry Gd-Pt Laves phase compounds,” *Journal of Physics F: Metal Physics*, vol. 6, no. 6, pp. 1125–1134, 1976. DOI: 10.1088/0305-4608/6/6/025.
- [55] A. E. Baranovskiy, G. E. Grechnev, I. V. Svechkarov, and O. Eriksson, “Electronic structure and magnetic properties of GdM₂ compounds,” *Journal of Magnetism and Magnetic Materials*, vol. 258-259, pp. 520–522, 2003. DOI: 10.1016/S0304-8853(02)01131-9.
- [56] W. E. Wallace and Y. G. Vlasov, “Magnetic properties of intermetallic compounds between the lanthanides and platinum,” *Inorganic Chemistry*, vol. 6, no. 12, pp. 2216–2219, 1967. DOI: 10.1021/ic50058a019.
- [57] J. L. Smith, Z. Fisk, and R. B. Roof, “Ferromagnetism in the RhGd and PtGd systems,” *Journal of Applied Physics*, vol. 52, no. 3, pp. 1684–1685, 1981. DOI: 10.1063/1.329679.
- [58] P. Arora, M. K. Chattopadhyay, and S. B. Roy, “Magnetic properties and large magnetocaloric effect of DyPt₂,” *Journal of Applied Physics*, vol. 106, p. 093 912, 2009. DOI: 10.1063/1.3253729.

- [59] C. J. Baddeley, A. W. Stephenson, C. Hardacre, M. Tikhov, and R. M. Lambert, "Structural and electronic properties of Ce overlayers and low-dimensional Pt-Ce alloys on Pt(111)," *Physical Review B - Condensed Matter and Materials Physics*, vol. 56, no. 19, pp. 12 589–12 598, 1997. DOI: 10.1103/physrevb.56.12589.
- [60] K. Ienaga, S. Kim, T. Miyamachi, and F. Komori, "Structural and electrical characterization of the monolayer Kondo-lattice compound CePt6/Pt(111)," *Physical Review B - Condensed Matter and Materials Physics*, vol. 104, no. 16, p. 165 419, 2021. DOI: 10.1103/PhysRevB.104.165419.
- [61] J. Tang, J. M. Lawrence, and J. C. Hemminger, "Structure and valence of the Ce/Pt(111) system," *Physical Review B - Condensed Matter and Materials Physics*, vol. 48, no. 20, pp. 15 342–15 352, 1993. DOI: 10.1103/PhysRevB.48.15342.
- [62] J. M. Essen, C. Becker, and K. Wandelt, "Pt_xCe_{1-x} Surface Alloys on Pt(111): Structure and Adsorption," *e-Journal of Surface Science and Nanotechnology*, vol. 7, pp. 421–428, 2009. DOI: 10.1380/ejssnt.2009.421.
- [63] J. Kemmer, C. Praetorius, A. Krönlein, P. J. Hsu, K. Fauth, and M. Bode, "Structural analysis of the intermetallic surface compound CePt5/Pt(111)," *Physical Review B - Condensed Matter and Materials Physics*, vol. 90, no. 19, p. 195 401, 2014. DOI: 10.1103/PhysRevB.90.195401.
- [64] C. Praetorius *et al.*, "Electronic tuneability of a structurally rigid surface intermetallic and Kondo lattice: CePt5/Pt(111)," *Physical Review B - Condensed Matter and Materials Physics*, vol. 92, no. 4, p. 045 116, 2015. DOI: 10.1103/PhysRevB.92.045116.
- [65] C. Praetorius, M. Zinner, G. Held, and K. Fauth, "Surface termination of CePt5/Pt(111): The key to chemical inertness," *Physical Review B - Condensed Matter and Materials Physics*, vol. 92, no. 19, p. 195 427, 2015. DOI: 10.1103/PhysRevB.92.195427.
- [66] U. Berner and K. D. Schierbaum, "Cerium oxides and cerium-platinum surface alloys on Pt(111) single-crystal surfaces studied by scanning tunneling microscopy," *Physical Review B - Condensed Matter and Materials Physics*, vol. 65, no. 23, p. 235 404, 2002. DOI: 10.1103/PhysRevB.65.235404.
- [67] U. Berner and K. Schierbaum, "Cerium oxide layers on Pt(111): A scanning tunneling microscopy study," *Thin Solid Films*, vol. 400, pp. 46–49, 2001. DOI: 10.1016/S0040-6090(01)01446-8.
- [68] A. Ramstad and S. Raaen, "Formation of and co adsorption on an inert la-pt(111) surface alloy," *Physical Review B - Condensed Matter and Materials Physics*, vol. 59, no. 24, pp. 15 935–15 941, 1999. DOI: 10.1103/PhysRevB.59.15935.

- [69] A. Ramstad, S. Raaen, and N. Barrett, "Electronic structure of the La-Pt(111) surface alloy," *Surface Science*, vol. 448, pp. 179–186, 2000. DOI: 10.1016/S0039-6028(99)01237-6.
- [70] M. Garnier, D. Purdie, K. Breuer, M. Hengsberger, and Y. Baer, "Momentum-resolved photoemission of the Kondo peak in an ordered Ce-containing alloy," *Physical Review B - Condensed Matter and Materials Physics*, vol. 56, no. 18, R11399–R11402, 1997. DOI: 10.1103/PhysRevB.56.R11399.
- [71] M. Garnier, D. Purdie, K. Breuer, M. Hengsberger, and Y. Baer, "Comparative photoemission study of Pt(111)(3×3)R30°Ce and Pt(111)(2×2)La," *Physical Review B - Condensed Matter and Materials Physics*, vol. 58, no. 15, pp. 9697–9699, 1998. DOI: 10.1103/physrevb.58.9697.
- [72] M. Kildemo, M. Juel, and S. Raaen, "Properties of Tm - Pt(111) surface alloys," *Surface Science*, vol. 581, pp. 133–141, 2005. DOI: 10.1016/j.susc.2005.02.036.
- [73] E. Meyer, H. J. Hug, and R. Bennewitz, *Scanning Probe Microscopy: The Lab on a Tip*, 1st. Berlin Heidelberg: Springer-Verlag Berlin Heidelberg, 2004, p. 210, ISBN: 9783642077371. DOI: 10.1007/978-3-662-09801-1.
- [74] G. Binnig, H. Rohrer, C. Gerber, and E. Weibel, "Tunneling through a controllable vacuum gap," *Applied Physics Letters*, vol. 40, no. 2, pp. 178–180, 1982. DOI: 10.1063/1.92999.
- [75] G. Binnig, H. Rohrer, C. Gerber, and E. Weibel, "Surface studies by scanning tunneling microscopy," *Physical Review Letters*, vol. 49, no. 1, pp. 57–61, 1982. DOI: 10.1103/PhysRevLett.49.57.
- [76] G. Binnig, H. Rohrer, C. Gerber, and E. Weibel, "7 x 7 Reconstruction on Si(111) Resolved in Real Space," *Physical Review Letters*, vol. 50, no. 2, pp. 120–123, 1983. DOI: 10.1103/PhysRevLett.50.120.
- [77] G. Binnig and H. Rohrer, "Nobel Lecture: Scanning Tunneling Microscopy - from Birth to Adolescence," *Reviews of Modern Physics*, vol. 59, no. 3, pp. 615–625, 1987. DOI: 10.1002/anie.198706061.
- [78] G. Binnig and D. P. Smith, "Single-tube three-dimensional scanner for scanning tunneling microscopy," *Review of Scientific Instruments*, vol. 57, no. 8, pp. 1688–1689, 1986. DOI: 10.1063/1.1139196.
- [79] R. Wiesendanger, *Scanning Probe Microscopy and Spectroscopy Methods and Applications Roland*, 1st. Cambridge: University Press, 1994, p. 667, ISBN: 9780511524356. DOI: 10.1017/CB09780511524356.
- [80] J. Bardeen, "Tunneling from a many-particle point of view," *Physical Review Letters*, vol. 6, no. 2, pp. 57–59, 1961. DOI: 10.1103/PhysRevLett.6.57.
- [81] J. Tersoff and D. R. Hamann, "Theory and Application for the Scanning Tunneling Microscope," *Physical Review Letters*, vol. 50, no. 25, pp. 1998–2001, 1983. DOI: 10.1103/PhysRevLett.50.1998.

- [82] J. Tersoff and D. R. Hamann, "Theory of the scanning tunneling microscope," *Physical Review B - Condensed Matter and Materials Physics*, vol. 31, no. 2, pp. 805–813, 1985. DOI: 10.1103/PhysRevB.31.805.
- [83] C. J. Chen, "Tunneling matrix elements in three-dimensional space: The derivative rule and the sum rule," *Physical Review B - Condensed Matter and Materials Physics*, vol. 42, no. 14, pp. 8841–8857, 1990. DOI: 10.1103/PhysRevB.42.8841.
- [84] N. D. Lang, "Spectroscopy of single atoms in the scanning tunneling microscope," *Physical Review B - Condensed Matter and Materials Physics*, vol. 34, no. 8, pp. 5947–5950, 1986. DOI: 10.1103/PhysRevB.34.5947.
- [85] J. H. Scofield, "Frequency-domain description of a lock-in amplifier," *American Journal of Physics*, vol. 62, no. 2, pp. 129–133, 1994. DOI: 10.1119/1.17629.
- [86] V. A. Ukraintsev, "Data evaluation technique for electron-tunneling spectroscopy," *Physical Review B - Condensed Matter and Materials Physics*, vol. 53, no. 16, pp. 11176–11185, 1996. DOI: 10.1103/PhysRevB.53.11176.
- [87] R. W. Wood, "A new form of cathode discharge and the production of x-rays, together with some notes on diffraction. Preliminary Communication," *Physical Review*, vol. 5, no. 1, pp. 1–10, 1897. DOI: 10.1103/PhysRevSeriesI.5.1.
- [88] R. H. Fowler and L. W. Nordheim, "Electron Emission in Intense Electric Fields," *Proceedings of the Royal Society of London. Series A, Containing Papers of a Mathematical and Physical Character*, vol. 119, no. 781, pp. 173–181, 1928. DOI: 10.1142/9789814503464_0087.
- [89] A. Schlenhoff, "Imaging and Switching Individual Nanomagnets with Spin-Polarized Scanning Field Emission Microscopy," Ph.D. dissertation, Universität Hamburg, 2013, p. 130.
- [90] W. Schottky, "Über kalte und warme Elektronenentladungen," *Zeitschrift für Physik*, vol. 14, pp. 63–106, 1923. DOI: 10.1007/BF01340034.
- [91] G. Binnig *et al.*, "Tunneling spectroscopy and inverse photoemission: Image and field states," *Physical Review Letters*, vol. 55, no. 9, pp. 991–994, 1985. DOI: 10.1103/PhysRevLett.55.991.
- [92] J. H. Coombs and J. K. Gimzewski, "Fine structure in field emission resonances at surfaces," *Journal of Microscopy*, vol. 152, no. 3, pp. 841–851, 1988. DOI: 10.1111/j.1365-2818.1988.tb01457.x.
- [93] K. H. Gundlach, "Zur berechnung des tunnelstroms durch eine trapezförmige potentialstufe," *Solid State Electronics*, vol. 9, pp. 949–957, 1966. DOI: 10.1016/0038-1101(66)90071-2.

- [94] R. M. Feenstra, J. A. Stroscio, and A. P. Fein, "Tunneling spectroscopy of the Si(111) 2×1 surface," *Surface Science*, vol. 181, pp. 295–306, 1987. DOI: 10.1016/0039-6028(87)90170-1.
- [95] R. J. Hamers, "Atomic-resolution surface spectroscopy with the scanning tunneling microscope," *Annual Review of Physical Chemistry*, vol. 40, pp. 531–559, 1989. DOI: 10.1146/annurev.pc.40.100189.002531.
- [96] C. Davisson and L. H. Germer, "The scattering of electrons by a single crystal of nickel," *Nature*, vol. 119, no. 2998, pp. 558–560, 1927. DOI: 10.1038/119558a0.
- [97] C. J. Davisson, "Nobel Lecture: The Discovery of Electron Waves," *Bell System Technical Journal*, vol. 17, no. 3, pp. 475–482, 1938. DOI: 10.1002/j.1538-7305.1938.tb00792.x.
- [98] L. de Broglie, "Recherches sur la théorie des quanta (Researches on the quantum theory)," Ph.D. dissertation, Université de Paris, 1924.
- [99] D. J. O'Connor, B. A. Sexton, and R. S. C. Smart, Eds., *Surface Analysis Methods in Material Science*, First edition. Berlin, Heidelberg: Springer, 1992, p. 453, ISBN: 978-3-662-02767-7. DOI: 10.1007/978-3-662-02767-7.
- [100] A. T. Hubbard, Ed., *The Handbook of Surface Imaging and Visualization*, First edition. Berlin, Heidelberg: CRC Press, 1995, p. 942, ISBN: 9780849389115.
- [101] A. Zangwill, *Physics at Surfaces*, Fifth edition. Cambridge University Press, 1996, p. 146, ISBN: 9780511622564.
- [102] W. H. Bragg and W. L. Bragg, "The Reflection of X-rays by Crystals," *Proceedings of the Royal Society A: Mathematical, Physical and Engineering Sciences*, vol. 88, no. 605, pp. 428–438, 1913. DOI: 10.1098/rspa.1913.0040.
- [103] L. Meitner, "Über die Entstehung der β -Strahl-Spektren radioaktiver Substanzen," *Zeitschrift für Physik*, vol. 9, pp. 131–144, 1922. DOI: 10.1007/BF01326962.
- [104] P. Auger, "Sur les rayons β secondaires produits dans un gaz par des rayons X," *Comptes Rendus des séances hebdomadaires de l'Académie des Sciences*, vol. 177, pp. 169–171, 1923.
- [105] D. Vrij, Ed., *Handbook of Applied Solid State Spectroscopy*. New York: Springer New York, NY, 2006, p. 742, ISBN: 0-387-32497-6.
- [106] L. E. Davis, N. C. MacDonald, P. W. Palmberg, G. E. Riach, and R. E. Weber, *Handbook of Auger Electron Spectroscopy*, Second edition. Minnesota: Physical Electronics Division Perkin-Elmer Corporation, 1976, p. 253, ISBN: 9780964812406.
- [107] G. McGuire, *Auger Electron Spectroscopy Reference Manual: A Book of Standard Spectra for Identification and Interpretation of Auger Electron Spectroscopy Data*. New York: Springer New York, NY, 2013, p. 135, ISBN: 9781475717020.

- [108] C. C. Chang, "Auger electron spectroscopy," *Surface Science*, vol. 25, pp. 53–79, 1971. DOI: 10.1016/0039-6028(71)90210-X.
- [109] W. C. Roentgen, "On a new kind of rays," *Nature*, vol. 53, no. 1369, pp. 274–276, 1896. DOI: 10.1038/053274b0.
- [110] F. de Groot and A. Kotani, *Core level spectroscopy of solids*, First edition. Boca Raton: CRC Press, 2008, p. 512, ISBN: 9780849390715.
- [111] H. Wende, "Recent advances in x-ray absorption spectroscopy," *Reports on Progress in Physics*, vol. 67, pp. 2105–2181, 2004. DOI: 10.1088/0034-4885/67/12/R01.
- [112] E. Beaurepaire, H. Bulou, F. Scheurer, and J. P. Kappler, Eds., *Magnetism and synchrotron radiation*, First edition. Berlin: Springer-Verlag, 2010, p. 442, ISBN: 9783642044977.
- [113] A. Thompson *et al.*, *X-Ray Data Booklet*, Third edition. Lawrence Berkeley National Laboratory, University of California, 2009, p. 176.
- [114] Center for X-Ray Optics, *X-Ray Interactions With Matter*, Accessed Jan. 18, 2023 [Online], Available: https://henke.lbl.gov/optical_constants/.
- [115] H. Kronmüller and S. Parkin, Eds., *Handbook of magnetism and advanced magnetic materials*, First edition. New Jersey: John Wiley and Sons, 2007, p. 2912, ISBN: 9780470022184. DOI: 10.1002/9780470022184.
- [116] G. van der Laan and A. I. Figueroa, "X-ray magnetic circular dichroism - A versatile tool to study magnetism," *Coordination Chemistry Reviews*, vol. 277-278, pp. 95–129, 2014. DOI: 10.1016/j.ccr.2014.03.018.
- [117] I. A. Kowalik, "Element specific magnetometry combining X-ray circular with linear dichroism: Fundamentals and applications," *Acta Physica Polonica A*, vol. 127, no. 3, pp. 831–849, 2015. DOI: 10.12693/APhysPo1A.127.831.
- [118] J. Stöhr, "X-ray magnetic circular dichroism spectroscopy of transition metal thin films," *Journal of Electron Spectroscopy and Related Phenomena*, vol. 75, no. 95, pp. 253–272, 1995. DOI: 10.1016/0368-2048(95)02537-5.
- [119] E. Goering, J. Will, J. Geissler, M. Justen, F. Weigand, and G. Schuetz, "X-ray magnetic circular dichroism - A universal tool for magnetic investigations," *Journal of Alloys and Compounds*, vol. 328, pp. 14–19, 2001. DOI: 10.1016/S0925-8388(01)01324-X.
- [120] J. L. Erskine and E. A. Stern, "Calculation of the M23 magneto-optical absorption spectrum of ferromagnetic nickel," *Physical Review B - Condensed Matter and Materials Physics*, vol. 12, no. 11, pp. 5016–5024, 1975. DOI: 10.1103/PhysRevB.12.5016.
- [121] G. Schutz *et al.*, "Absorption of circularly polarized x rays in iron," *Physical Review Letters*, vol. 58, no. 7, pp. 737–740, 1987. DOI: 10.1103/PhysRevLett.58.737.

- [122] F. Baudelet *et al.*, “Study of 5d magnetism in rare-earth-transition-metal (Fe, Co) intermetallic compounds by magnetic circular X-ray dichroism,” *Journal of Electron Spectroscopy and Related Phenomena*, vol. 62, pp. 153–156, 1993. DOI: 10.1016/0368-2048(93)80012-B.
- [123] C. M. Praetorius, “Ce M_{4,5} XAS and XMCD as local probes for Kondo and heavy fermion materials - a study of CePt₅/Pt(111) surface intermetallics,” Ph.D. dissertation, Universitat Wurzburg, 2015, p. 260.
- [124] B. T. Thole, P. Carra, F. Sette, and G. Van Der Laan, “X-ray circular dichroism as a probe of orbital magnetization,” *Physical Review Letters*, vol. 68, no. 12, pp. 1943–1946, 1992. DOI: 10.1103/PhysRevLett.68.1943.
- [125] P. Carra, B. T. Thole, M. Altarelli, and X. Wang, “X-ray circular dichroism and local magnetic fields,” *Physical Review Letters*, vol. 70, no. 5, pp. 694–697, 1993. DOI: 10.1103/PhysRevLett.70.694.
- [126] A. Tcakaev *et al.*, “Incipient antiferromagnetism in the Eu-doped topological insulator Bi₂Te₃,” *Physical Review B - Condensed Matter and Materials Physics*, vol. 102, no. 18, p. 184401, 2020. DOI: 10.1103/PhysRevB.102.184401.
- [127] P. Hohenberg and W. Kohn, “Inhomogeneous Electron Gas,” *Physical Review*, vol. 136, no. 3B, pp. 864–871, 1964. DOI: 10.1103/PhysRev.136.B864.
- [128] L. Piela, *Ideas of Quantum Chemistry*, First edition. Amsterdam: Elsevier B.V, 2007, p. 1086, ISBN: 9780444522276.
- [129] W. Kohn and L. J. Sham, “Self-Consistent Equations Including Exchange and Correlation Effects,” *Physical Review*, vol. 140, no. 4A, A1133–A1138, 1965. DOI: 10.1103/PhysRev.140.A1133.
- [130] A. D. Becke, “Exchange–Correlation Approximations in Density-Functional Theory,” in *Modern Electronic Structure Theory Part II*, D. R. Yarkony, Ed., First edition, London: World Scientific, 1995, ch. 15, pp. 1022–1046, ISBN: 9789810219604. DOI: 10.1021/ja9655754.
- [131] J. P. Perdew and K. Burke, “Generalized gradient approximation for the exchange-correlation hole of a many-electron system,” *Physical Review B - Condensed Matter and Materials Physics*, vol. 54, no. 23, pp. 16533–16539, 1996. DOI: 10.1103/PhysRevB.54.16533.
- [132] S. Kurth, M. Marques, and E. Gross, “Density-Functional Theory,” in *Encyclopedia of Condensed Matter Physics*, F. Bassani, L. G. Liedl, and P. Wyder, Eds., Oxford: Elsevier Ltd, 2005, pp. 395–402. DOI: <https://doi.org/10.1016/B0-12-369401-9/00445-9>.
- [133] M. Bazarnik, “Influence of monocrystalline surfaces on switching possibilities of 4-anilino-4’nitroazobenzene,” Ph.D. dissertation, Poznan University of Technology, 2011, p. 101.

- [134] *Operating manual - konti cryostat*, CryoVac Gesellschaft für Tieftemperaturtechnik mbH and CO KG, Heuserweg 16, D-53842 Troisdorf, Germany, 1995, pp. 1–21.
- [135] Paul Scherrer Institut, *X-Treme/X07MA: X-ray absorption spectroscopy at high magnetic field and low temperature*, Accessed Feb. 3, 2023 [Online], Available: <https://www.psi.ch/en/sls/xtreme>.
- [136] A. Barla *et al.*, “Design and performance of BOREAS, the beamline for resonant X-ray absorption and scattering experiments at the ALBA synchrotron light source,” *Journal of Synchrotron Radiation*, vol. 23, 2016. DOI: 10.1107/S1600577516013461.
- [137] ALBA synchrotron, *BL29 - BOREAS, resonant absorption and scattering*, Accessed Feb. 2, 2023 [Online], Available: <https://www.cells.es/en/beamlines/bl29-boreas>.
- [138] J. Wiebe *et al.*, “Unoccupied surface state on Pt(111) revealed by scanning tunneling spectroscopy,” *Physical Review B - Condensed Matter and Materials Physics*, vol. 72, no. 19, p. 193406, 2005. DOI: 10.1103/PhysRevB.72.193406.
- [139] D. Nečas and P. Klapetek, “Gwyddion: An open-source software for SPM data analysis,” *Central European Journal of Physics*, vol. 10, no. 1, pp. 181–188, 2012. DOI: 10.2478/s11534-011-0096-2.
- [140] P. Giannozzi *et al.*, “QUANTUM ESPRESSO: A modular and open-source software project for quantum simulations of materials,” *Journal of Physics Condensed Matter*, vol. 21, no. 39, 2009. DOI: 10.1088/0953-8984/21/39/395502.
- [141] P. Giannozzi *et al.*, “Advanced capabilities for materials modelling with Quantum ESPRESSO,” *Journal of Physics: Condensed Matter*, no. 29, p. 465901, 2017. DOI: 10.1088/1361-648X/aa8f79.
- [142] M. J. Soler *et al.*, “The SIESTA method for ab initio order-N materials simulation,” *Journal of Physics: Condensed Matter*, vol. 14, pp. 2745–2779, 2002. DOI: 10.1088/0953-8984/14/11/302.
- [143] E. Artacho *et al.*, “The SIESTA method; Developments and applicability,” *Journal of Physics Condensed Matter*, vol. 20, no. 6, 2008. DOI: 10.1088/0953-8984/20/6/064208.
- [144] A. García *et al.*, “Siesta: Recent developments and applications,” *The Journal of chemical physics*, vol. 152, no. 20, p. 204108, 2020. DOI: 10.1063/5.0005077.
- [145] M. Przychodnia *et al.*, “Controlled growth of Gd-Pt surface alloys on Pt (111),” *Physical Review B - Condensed Matter and Materials Physics*, vol. 105, no. 3, p. 035416, 2022. DOI: 10.1103/PhysRevB.105.035416.
- [146] J. W. Arblaster, “Crystallographic properties of platinum,” *Platinum Metals Review*, vol. 41, no. 1, pp. 12–21, 1997. DOI: 10.1595/147106706X129088.

- [147] J. Jensen and A. R. Mackintosh, *Rare Earth Magnetism Structures and Excitations*, First edition, J. Birman, S. F. Edwards, C. H. Llewellyn Smith, and M. Rees, Eds. Oxford: Clarendon Press, 1991, p. 403, ISBN: 0198520271. DOI: 10.1038/physci241120a0.
- [148] M. Colarieti-Tosti *et al.*, “Origin of magnetic anisotropy of Gd metal,” *Physical Review Letters*, vol. 91, no. 15, p. 157201, 2003. DOI: 10.1103/PhysRevLett.91.157201.
- [149] B. Cordero *et al.*, “Covalent radii revisited,” *Dalton Transactions*, no. 21, pp. 2832–2838, 2008. DOI: 10.1039/b801115j.
- [150] F. Sojka and T. Fritz, Fritz & Sojka GbR, Apolda Germany, 2019, *Leedlab 2018*, version 1.2, Jun. 19, 2023. [Online]. Available: <https://fritz-sojka-gbr.de/leedlab/>.
- [151] V. López-Flores *et al.*, “Role of critical spin fluctuations in ultrafast demagnetization of transition-metal rare-earth alloys,” *Physical Review B - Condensed Matter and Materials Physics*, vol. 87, no. 214412, 2013. DOI: 10.1103/PhysRevB.87.214412.
- [152] M. Cardona and L. Ley, Eds., *Photoemission in Solids I, General Principles*, First edition. Berlin: Springer Berlin Heidelberg, 1978, p. 293, ISBN: 9783662309193. DOI: 10.1007/3-540-08685-4.
- [153] J. Yano and V. K. Yachandra, “X-ray absorption spectroscopy,” *Photosynthesis Research*, vol. 102, pp. 241–254, 2009. DOI: 10.1007/s11120-009-9473-8.
- [154] Y. Teramura, A. Tanaka, B. T. Thole, and T. Jo, “Effect of Coulomb Interaction on the X-Ray Magnetic Circular Dichroism Spin Sum Rule in Rare Earths,” *Journal of the Physical Society Japan*, vol. 65, no. 9, pp. 3056–3059, 1996. DOI: 10.1143/JPSJ.65.3056.
- [155] H. B. Vasili *et al.*, “Direct observation of multivalent states and 4f→3d charge transfer in Ce-doped yttrium iron garnet thin films,” *Physical Review B - Condensed Matter and Materials Physics*, vol. 96, no. 1, p. 014433, 2017. DOI: 10.1103/PhysRevB.96.014433.
- [156] H. J. F. Jansen, “Origin of orbital momentum and magnetic anisotropy in transition metals,” *Journal of Applied Physics*, vol. 67, pp. 4555–4557, 1990. DOI: 10.1063/1.344868.
- [157] S. Tripathi, “XMCD investigation at M4,5 edges of the rare earth elements in high-performance permanent magnet,” Ph.D. dissertation, University of Stuttgart, 2018, p. 176.
- [158] K. Fabian, V. P. Shcherbakov, and S. A. McEnroe, “Measuring the Curie temperature,” *Geochemistry, Geophysics, Geosystems*, vol. 14, no. 4, pp. 947–961, 2013. DOI: 10.1029/2012GC004440.
- [159] P. Arora, M. K. Chattopadhyay, L. S. Sharath Chandra, V. K. Sharma, and S. B. Roy, “Multiple magnetic transitions in Ag- substituted DyPt₂,” *Journal of Applied Physics*, vol. 112, p. 033906, 2012. DOI: 10.1063/1.4742024.

-
- [160] M. Atoji, "Magnetic structures of DyAu₂ and DyAg₂," *The Journal of Chemical Physics*, vol. 51, pp. 3877–3882, 1969. DOI: 10.1063/1.1672605.
- [161] N. V. Smith, G. K. Wertheim, S. Hufner, and M. M. Traum, "Photoemission spectra and band structures of d-band metals," *Physical Review B - Condensed Matter and Materials Physics*, vol. 10, no. 8, pp. 3197–3206, 1974. DOI: 10.1103/PhysRevB.10.3197.
- [162] A. Arrott, "Criterion for ferromagnetism from observations of magnetic isotherms," *Physical Review*, vol. 108, no. 6, pp. 1394–1396, 1957. DOI: 10.1103/PhysRev.108.1394.

List of Tables

3.1	Overview of REM-NM surface alloys' structural and growth parameters.	16
3.2	Overview of REM-NM surface alloys' magnetic and electronic properties.	17
4.1	The total probabilities of the excitation of a spin-up or spin-down electron from the $3d_{3/2}$ and $3d_{5/2}$ core levels.	48
4.2	Sum rules prefactors.	49
5.1	X-Treme endstation technical parameters.	68
5.2	BOREAS/HECTOR beamline and endstation technical parameters.	71
6.1	Calculated magnetic moments of Gd-Pt surface alloys.	89
7.1	Summary table of magnetic properties of investigated Gd-Pt and Dy-Pt surface alloys.	107

List of Figures

2.1	Summary graph of magnetic interactions.	3
2.2	Diagrams of superexchange	6
2.3	Dzialoshinsky-Moriya interaction scheme.	8
2.4	Scheme of possible scenarios of adatoms adsorption on the surface in nucleation stage.	9
2.5	Scheme of thin films growth modes.	10
3.1	Models of REMPt ₂ and REMPt ₅ surface alloys.	14
4.1	Scanning tunneling microscope setup scheme.	24
4.2	Energetic level diagrams in STM setup.	25
4.3	Scheme of one-dimensional quantum tunneling through a potential barrier.	27
4.4	STM imaging operating modes: CHM, CCM.	30
4.5	Lock-in adaptation to the STM setup	32
4.6	Overview of STM spectroscopic modes	34
4.7	Scheme of influence of negative electric field on the image potential	35
4.8	LEED/AES setup scheme.	37
4.9	Scheme of Bragg diffraction scenarios.	38
4.10	Scheme of Auger electron emission process.	39
4.11	X-ray notation scheme.	42
4.12	X-ray absorption detection modes.	43
4.13	Classification of XAS spectrum.	45
4.14	Scheme of adopted x-ray circular polarisation direction definition.	46

4.15	Two-step model of XMCD.	47
4.16	Concept of normal and grazing configurations for XAS/XMCD investigations.	49
5.1	Back view photo of UHV system with VT STM in Hamburg.	54
5.2	Front view photo of UHV system with VT STM in Hamburg.	55
5.3	Photo of VT STM setup used in Hamburg.	56
5.4	Front view photo of UHV system with VT STM in Poznan.	57
5.5	Back view photo of UHV system with VT STM in Poznan.	58
5.6	Photography and project visualisation of STM head.	60
5.7	Photographs of outer and inner shields of multipurpose STM head.	62
5.8	Graphs of main operating parameters of VT STM setup cooled with LN ₂	63
5.9	Scheme of continuous-flow cryostat operating principle.	64
5.10	Scheme of Gifford-McMahon refrigeration cycle.	65
5.11	Scheme of Joule-Thomson effect.	66
5.12	Gifford-McMahon and Joule-Thomson combined cryostat setup.	67
5.13	X-Treme beamline optical layout scheme.	69
5.14	X-Treme beamline endstation scheme.	69
5.15	BOREAS beamline endstation scheme.	70
5.16	BOREAS beamline optical layout scheme.	71
6.1	Pt(111) substrate STM and LEED characterization.	75
6.2	Pt(111) substrate PTS and AES characterization.	76
6.3	Thermal evolution of Dy-Pt surface structures.	77
6.4	Gd-Pt surface alloys - models and STM topography images.	79
6.5	Experimental and simulated LEED patterns of Gd-Pt surface alloys.	81
6.6	LTS results for Gd-Pt surface alloys.	83
6.7	Averaged LTS and DFT results for Gd-Pt surface alloys.	84
6.8	PDOS of Gd-Pt surface alloys.	85
6.9	Gd-Pt surface alloys area occupancy as a function of the substrate temperature and Gd coverage.	86
6.10	XAS and XMCD spectra for 1 L GdPt ₅ and 2 L GdPt ₅	88

6.11	1 L GdPt ₅ and 2 L GdPt ₅ hysteresis loops taken for normal and grazing incidence angles.	90
6.12	Graph of the temperature dependence of normalized remanence for 1 L GdPt ₅ and 2 L GdPt ₅	92
6.13	AES spectrum of 1 L DyPt ₂	93
6.14	Dy-Pt surface alloys – models and STM topography images.	94
6.15	Experimental and simulated LEED patterns of Dy-Pt surface alloys.	96
6.16	LTS results for Dy-Pt surface alloys.	97
6.17	Averaged LTS results for Dy-Pt surface alloys.	98
6.18	Field emission spectroscopy of 1 L DyPt ₂	99
6.19	Dy-Pt surface alloys area occupancy as a function of Dy coverage.	100
6.20	XAS and XMCD spectra for 1 L DyPt ₂ and 3 L DyPt ₂	102
6.21	1 L DyPt ₂ and 3 L DyPt ₂ hysteresis loops taken for normal and grazing incidence angles.	103
6.22	Arrott plots of 1 L DyPt ₂ and 3 L DyPt ₂	104

Acknowledgements

*"It is the time you have wasted for your rose
that makes your rose so important."*

– Antoine de Saint-Exupéry

I would like to express my deepest gratitude to all those who supported me during the preparation of my dissertation, as they made this time worthwhile for me.

First, I am incredibly grateful to my supervisor – Wojtek (D.Sc. Eng. Wojciech Koczorowski, PUT Professor) for taking me under his wings a few years ago when I started my scientific adventure, for trusting me and believing in me. Not only was he my supervisor, but he was also my colleague whom I could rely on in many situations, not only those related to my PhD and work. I am thankful for all his advice, conversations, and constant motivation towards self-development and shaping me as a scientist.

I also thank my auxiliary supervisor - Maciej (Ph.D. Eng. Maciej Bazarnik) for numerous scientific conversations, substantive support, and for sharing his knowledge and experience. I am grateful for his guidance during all my research stays abroad. I am thankful to Prof. Roland Wiesendanger for the opportunity to join his group during my research stays.

A special thank you to Prof. Ryszard Czajka for his invaluable support and constant motivation. I appreciate the acceptance into the Division of Surface Physics and Nanotechnology a few years ago, and his trust and support from the very beginning. I am grateful for his availability for conversation, advice, and help whenever I needed it. Thank you for every question "Has the dissertation been written yet?", which I have heard very often over the last months. I also appreciate that he always remembers all the occasions to celebrate.

I would like to thank Michał Hermanowicz for his contribution by conducting theoretical calculations that complemented the experimental results presented in the dissertation and for his analysis of these results. I would also like to thank Adrian Adamski for the hours spent together writing Python scripts for data analysis.

During my PhD adventure, the Poznan University of Technology became my second home. Therefore, I would like to thank my Colleagues from the Faculty of Materials Engineering and Technical Physics, especially Alicja, Michał, Łukasz, Ariadna, Johnny, Emilia P., Marek W., and Łukasz's Girls for the enjoyable working atmosphere that made me feel very comfortable. I am also especially thankful to Mr. Ryszard Banasiak for his invaluable help in mechanical work, his ideas, patience, and precision. Additionally, I thank Ania Piechowiak for her patience and assistance with orders and administrative tasks. Thank you all for the moments we spent together: all the dinners we got, scientific and non-scientific conversations, your support and advice, and all the moments that have made me happy. Since I have spent also part of my PhD time abroad, I want to thank Emil and Micha for their support during my stays in Hamburg.

I would like to express my great thanks to Semir, for his enormous understanding and patience during my PhD journey. I appreciate all the support and motivation that he gave me. Without you by my side, it would not be what it is now.

Finally, I am grateful to my beloved parents for their unwavering support and understanding. Thank you for always being with me at every step of my life, for always being there when I needed you, and for believing in me so much.

Financial support

The research presented in this dissertation was funded by:

PRELUDIUM, National Science Centre Poland,

Two-dimensional, magnetic surface alloys based on rare earth metals and platinum. Investigation of electronic and magnetic properties with atomic resolution.,
grant number: 2019/33/N/ST5/01711



SONATA BIS, National Science Centre Poland,

On-surface in vacuo synthesis of salophene derivatives on noble metal monocrystalline surfaces. Characterization of their electronic and magnetic properties.,
grant number: 2017/26/E/ST3/00140,
principal investigator: Ph.D. Eng. Maciej Bazarnik



ALBA Synchrotron,

These experiments were performed at BL29 - BOREAS Resonant absorption and scattering beamline at ALBA Synchrotron with the collaboration of ALBA staff.,
proposals IDs: 2021095330 and 2022085937



Swiss Light Source, Paul Scherrer Institut,

We acknowledge the Paul Scherrer Institut, Villigen, Switzerland for the provision of synchrotron radiation beamtime at beamline X-Treme / X07MA: X-ray absorption spectroscopy at high magnetic field and low temperature of the SLS.,
proposal ID: 20211738



